The Crystalline Structure of Polydimethylsiloxane : Additional Results and Additional Questions

Xiang Shi

université PARIS-SACLAY

The Crystalline Structure of Polydimethylsiloxane: Additional Results and Additional Questions

Thèse de doctorat de l'université Paris-Saclay

École doctorale n° 564 : Physique en Ile-de-France (PIF)
Spécialité de doctorat: Physique
Unité de recherche : Université Paris-Saclay, CNRS, Laboratoire de Physique des Solides, 91405, Orsay, France.
Référent : Faculté des sciences d'Orsay

Thèse présentée et soutenue à Orsay, le 15 janvier 2021, par

Xiang SHI

Composition du Jury

Patrick JUDEINSTEIN Directeur de recherche, CNRS (Laboratoire Léon Brillouin, CEA Saclay)	Président
Sylvie TENCÉ-GIRAULT Ingénieure Arkema, HDR, détachée au CNRS (PIMM, ENSAM Paris)	Rapporteure & Examinatrice
Stéphane MERY Chargé de recherche, HDR, CNRS (IPCMS, Université de Strasbourg)	Rapporteur & Examinateur
Pierre-Antoine ALBOUY Directeur de recherche, CNRS (LPS, Université Paris-Saclay)	Directeur de thèse
Min-Hui LI Directrice de recherche, CNRS (IRCP, ENSCP, Université PSL)	Co-Directrice de thèse

Thèse de doctorat

NNT : 2021UPASP009

Résumé

INTRODUCTION. Le polydiméthylsiloxane (PDMS) est un polymère caractérisé à la fois par une stabilité thermique élevée et des températures de fusion et de transition vitreuse très basses. Il se présente sous forme d'huiles de viscosité variable et peut être réticulé pour former des élastomères (« caoutchoucs silicones »). Une grande gamme de température d'utilisation combinée à des propriétés intéressantes telles que la biocompatibilité expliquent les nombreuses applications dont il fait l'objet.

En 1958, Ohlberg *et coll.* ont été les premiers à enregistrer les diagrammes de diffraction X d'élastomères de PDMS soumis à une traction uniaxiale (Voir **Figure 1-A**). A température ambiante, l'échantillon est amorphe et les clichés de diffraction présentent une succession d'anneaux diffus se structurant sous traction, reflétant l'orientation progressive des chaînes polymères. L'échantillon devient semi-cristallin à basse température, et les auteurs soulignent les changements particuliers des diagrammes de diffraction. Dans la seconde partie de cette étude, Warrick *et coll.* se sont intéressés au comportement thermo-élastique lors d'un refroidissement progressif (voir **Figure 1-B**). Ils ont mis en évidence une augmentation brutale et spectaculaire de la force de rétraction, attribuée à la cristallisation partielle.

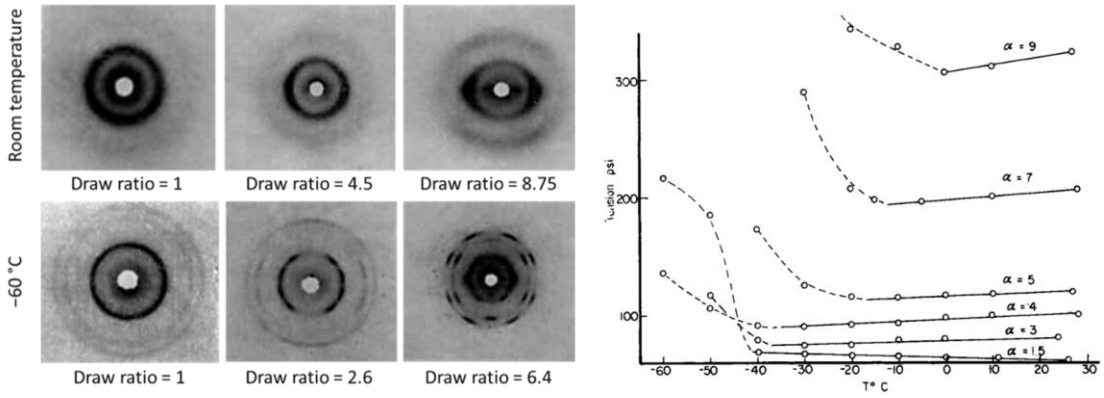

-A- **-B-**

Figure 1 A- diagrammes de diffraction X d'un élastomère de PDMS chargé en silice et soumis à différentes élongations statiques (ambiante et -60 °C). B- Comportement thermo-élastiques de ces échantillons lors d'un refroidissement progressif.

Une première structure cristalline du PDMS a été proposée par *Damaschun* en 1962 à partir du diagramme de texture d'un échantillon fortement étiré. Il suppose que la maille est monoclinique et qu'elle est traversée par une seule chaîne polymère présentant une conformation assez relaxée en hélice 2_1, avec six monomères par maille.

Ce travail est repris en 2000 par *Albouy* qui, travaillant sur des échantillons peu allongés, propose une structure quadratique centrée, dans laquelle deux chaînes polymères en conformation 4_1 très étendue traversent la maille. Celle-ci contient huit monomères, en bon accord avec la densité expérimentale ; dans les deux cas, aucune structure atomique n'est proposée. Du fait de positions similaires pour les raies de diffraction dans les deux états d'élongation, *Albouy* attribue les différences entre les diagrammes de diffraction à une *différence de texture*. En 2013, *Tosaka* et coll. reprennent ce travail et attribuent ces différences à un *polymorphisme* complexe. Des structures atomiques sont proposées, sans aucune comparaison entre intensités diffractées mesurées et calculées.

Le premier but de cette thèse est donc de déterminer s'il y a polymorphisme ou simple changement de texture, puis de déterminer une ou des structures atomiques en se basant sur les intensités mesurées. Une seconde question intéressante concerne l'augmentation brutale de la force de rétraction durant un refroidissement progressif, et de savoir à quoi elle est liée. D'autres données intéressantes ont également été collectées.

SYNTHÈSE DES ÉCHANTILLONS. Le but est d'obtenir des échantillons pouvant supporter une élongation d'un facteur au moins égal à 5, valeur à laquelle le diagramme « haute extension » est observé. En l'absence de charge ajoutée, les caoutchoucs silicones sont très fragiles. Une charge de silice est normalement utilisée et de deux processus ont été utilisés ici : croissance *in situ* de silice par un procédé sol-gel et ajout d'une charge de silice nanométrique modifiée commerciale.

PROPRIÉTÉS MÉCANIQUES À TEMPÉRATURE AMBIANTE. Les propriétés mécaniques (modules élastiques, élongation à la rupture) des échantillons synthétisés sont étudiées. Des mesures parallèles de diffraction X sont effectuées, ce qui donne accès au coefficient d'amplification des contraintes : il mesure le rapport entre la contrainte appliquée et celle ressentie par le PDMS en présence de charges de silice ajoutée. La silice nanométrique apparaît beaucoup plus efficace pour ce qui concerne l'élongation à la rupture et le coefficient d'amplification des contraintes est proche de celui calculé en supposant la silice indéformable (**Figure 2-A**). Les échantillons chargés en silice sol-gel cassent plus rapidement mais le coefficient d'amplification des contraintes est très supérieur à celui calculé (**Figure 2-B**). Cet effet très intéressant n'avait jamais été rapporté.

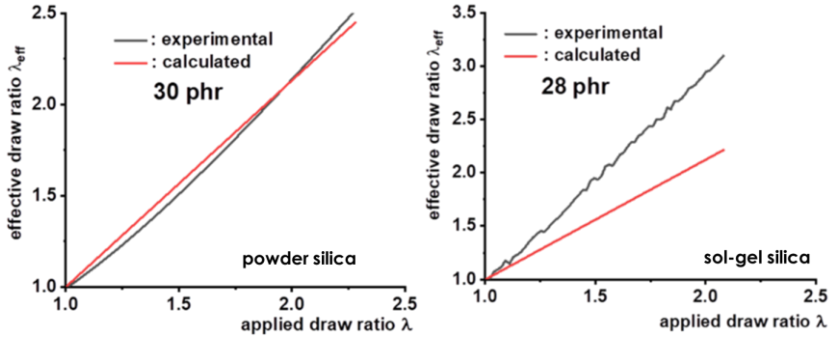

-A- **-B-**

Figure 2 Elongation effective ressentie par la gomme de PDMS en fonction de l'élongation macroscopique appliqué. -A- poudre nanométrique de silice -B- silice sol-gel.

ÉVOLUTION DES DIGRAMMES DE DIFFRACTION BASSE TEMPÉRATURE : MESURES ET SIMULATIONS. Deux explications différentes ont été proposées pour expliquer la modification des diagrammes de diffraction observée selon l'extension appliquée : (1) changement de texture et structure cristalline conservée, (2) polymorphisme caractérisé par l'existence de quatre structures cristallines. Des clichés de diffraction ont été obtenus à basse température (-100 °C) pour différentes extensions appliquées (**Figure 2-A**). Des simulations effectuées en collaboration avec Pascale LAUNOIS (LPS, Université Paris-Saclay) montrent que tous les diagrammes expérimentaux peuvent être expliqués par un changement de texture, en conservant la même phase cristalline quadratique centrée (**Figure 3-B**). L'axe d'orientation préférentiel passe d'une direction [001] à faible extension à une direction [111] à forte extension. Il reste dans un plan (1-10) aux extensions intermédiaires (**Figure 3-C**).

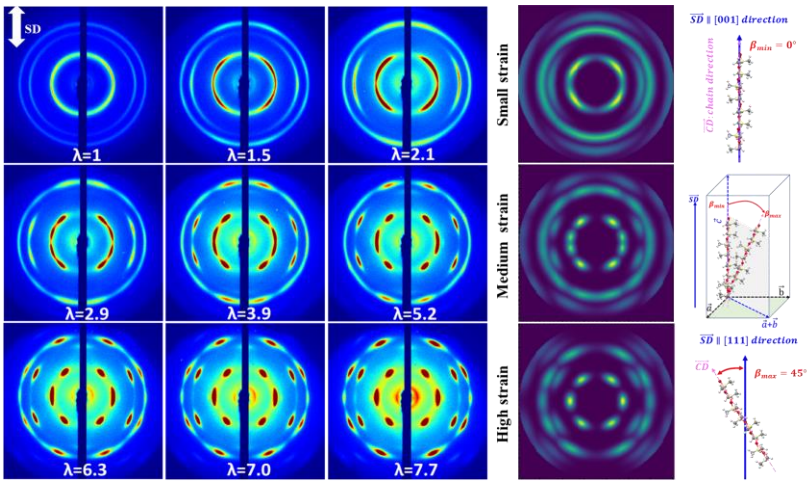

-A- **-B-** **-C-**

Figure 3 -A- diagrammes de diffraction expérimentaux mesurés à différentes élongations à -100 °C. – B- Simulation de diagrammes de textures. –C- Variation associée de l'orientation des chaînes polymères.

COMPORTEMENT THERMO-ÉLASTIQUE. On voit sur la **Figure 4-A** que l'augmentation de la force de rétraction se fait en net décalage avec le processus de cristallisation : le taux de cristallisation a déjà atteint un plateau lorsque cette augmentation se produit. On sait que le module élastique d'une phase cristalline est très supérieur à celui de la phase fondue : ceci s'explique d'une part par un module de la phase cristalline très élevé et d'autre part un module de la phase amorphe lui aussi augmenté par le confinement. L'augmentation de la force de rétraction est alors expliquée par la contraction thermique de l'échantillon. La **Figure 4-C** montre les valeurs des modules calculés à partir de la différence de force de rétraction et de la contraction thermique associée. Les valeurs sont en bon accord avec des mesures de DMA déjà publiées. L'augmentation de la température de fusion avec la contrainte appliquée est significative amis moindre que ce qui est observé par exemple dans le caoutchouc naturel (**Figure 4-B**).

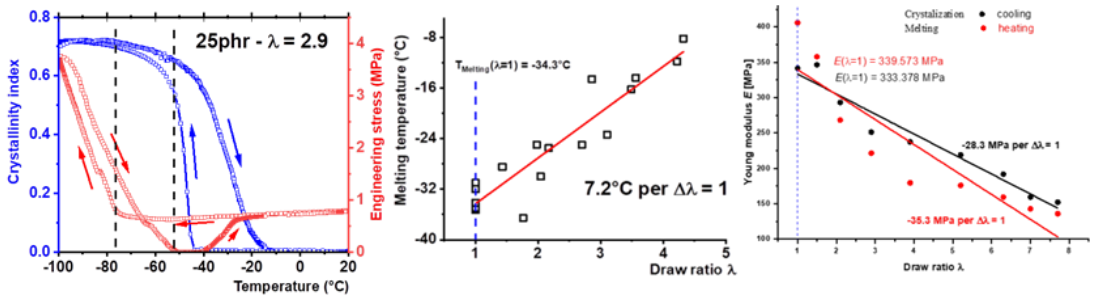

-A- **-B-** **-C-**

Figure 4 -A- Variation de l'indice de cristallinité et de la force de rétraction durant un cycle en température pour un échantillon préétiré. –B- Variation de la température de fusion en fonction de l'élongation appliquée. –C- Module élastique calculé à partir du taux de contraction thermique et de la variation de la force de rétraction.

Une phase très orientée apparaît aux plus fortes élongations (phase « mésomorphe »). La **Figure 5** montre que cette phase est différente de la phase cristalline (caractérisée par l'apparition de multiples réflexions) mais qu'elle lui est liée.

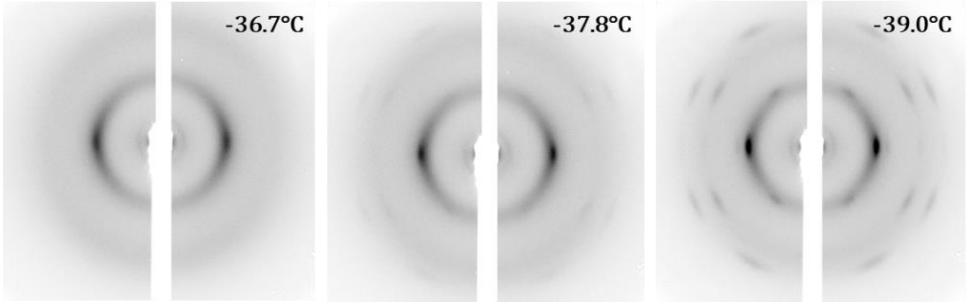

Figure 5 Passage de la phase mésomorphe à la phase cristalline.

ÉTUDE CRISTALLOGRAPHIQUE. Cette étude est essentiellement basée sur l'analyse de diagrammes de diffraction de type ϑ-2ϑ tels que représentés sur la **Figure 6** (quelques mesures de diffraction électronique basse température ont également été effectuées). La position angulaire des nombreuses raies de diffractions est précisément donnée par une maille quadratique centrée de paramètres a=0.83972nm et c=1.19773nm à 170K. On peut remarquer que le rapport des deux paramètres est très proche de $\sqrt{2}$.

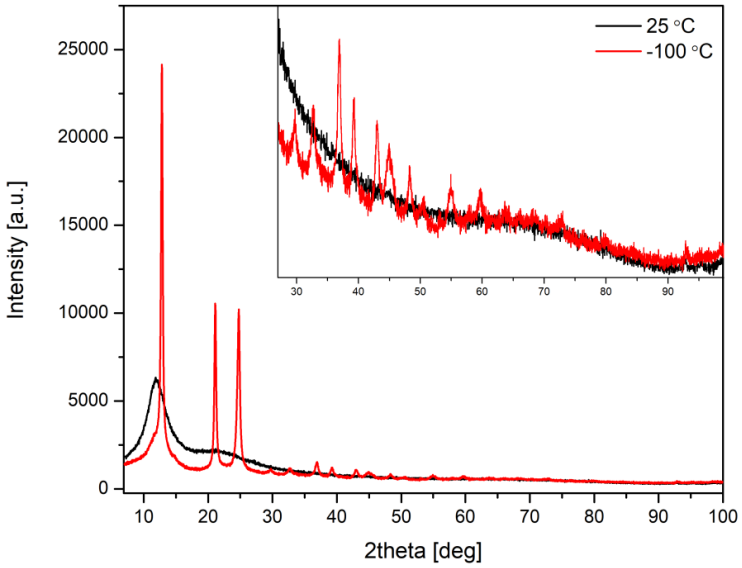

Figure 6 Diagrammes de diffraction haute et basse température.

Une optimisation de type DFT et un affinement de Rietveld ont été tout d'abord effectués dans le groupe $I4_1$ qui est le seul à donner une densité correcte. L'affinement ne converge pas de façon satisfaisante et la réflexion *110* absente du diagramme expérimentale est calculée comme intense. Cette réflexion est absente dans le groupe $I4_1/a$ qui a également été testé. Dans ce cas, il est nécessaire d'imposer un taux d'occupation de 0.5 afin de garder une densité correcte (huit monomères par maille en moyenne). L'ajustement n'est pas satisfaisant dans ce cas non plus. La **Figure 7** donne les configurations obtenues dans les deux cas : les chaînes polymères présentent dans ces deux cas une conformation étendue avec un axe 4_1 ou 4_3.

Une explication possible est l'existence de domaines cohérents de groupe d'espace $I4_1$ et contenant des chaînes soit 4_1 ou 4_3. Le passage d'un domaine à l'autre correspondrait au passage d'une conformation 4_1 à une conformation 4_3 pour la chaîne polymère.

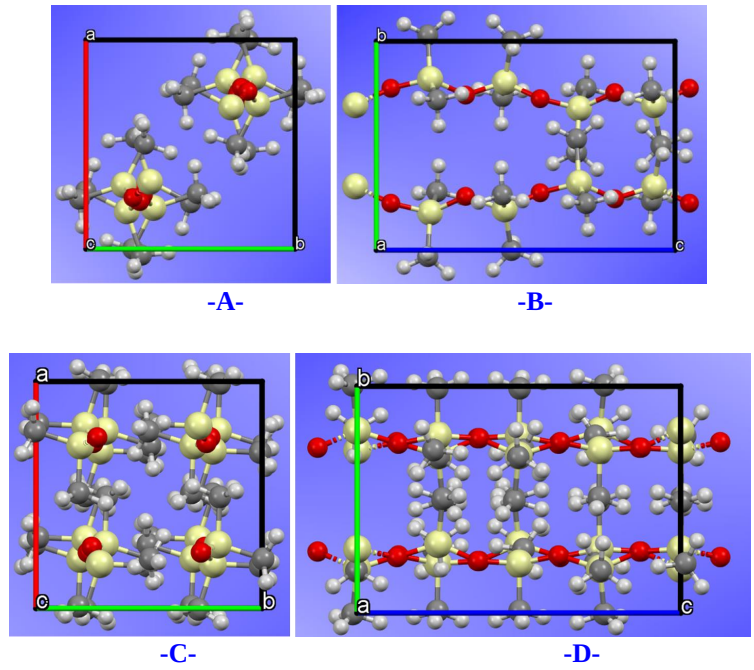

Figure 7 –A et B - Vue de face et latérale de l'empilement des chaînes polymères pour le groupe $I4_1$. – C et D- Vue de face et latérale de l'empilement des chaînes polymères pour le groupe $I4_1/a$

ÉTUDE DE DEUX ORGANOGÉLATEURS À BASE DE CHOLESTÉROL. Cette étude de la structure cristalline du PDMS a été complétée par des mesures de diffractions X sur différents organo-gélateurs dont les propriétés chromatiques sont sensibles à différents stimuli (voir **Figure 8**). Ceci constituait le sujet initial de cette thèse, qui a été modifié au vu de la trop importante chimie nécessaire.

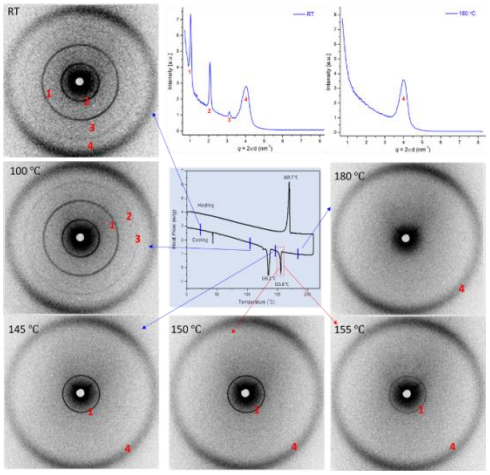

Figure 8 Exemples de diagrammes de diffraction obtenus sur différents organo-gélateurs.

Mots clef : poly(diméthylsiloxane) (PDMS), caoutchouc silicone, amplification des déformations, diagrammes de fibre, propriétés thermo-élastiques, cristallographie

Acknowledgements

At first, I would like to express my sincere thanks to everyone who supported me and gave me their help during my PhD duration.

The greatest support and help were from my supervisor Prof. Pierre-Antoine ALBOUY (Laboratoire de Physique des Solides, Université Paris-Saclay), I would like to thank him for giving me this great opportunity of performing X ray crystallographic research in Laboratoire de Physique des Solides. He was a humorous and passionate person that I extremely admire. I admire his spirit of hardworking in research of science and his strong capability of instrument design and renovation, his diligent and rigorous scientific attitude impresses me so much. Besides the fundamentals of X-ray diffraction and scattering, he taught me how to operate, assemble, troubleshoot and test different X-ray scattering instruments, he also gave me a lot of assistance in interpreting the experimental data and writing a thesis manuscript. I would also like to express my profound appreciation to my co-supervisor Prof. Min-Hui Li (École Nationale Supérieure de Chimie de Paris, Université PSL), I appreciate her kindness and lenience very much during my difficult time. She taught and helped me a lot, not only at research, but also at life.

Especially, I am grateful to Prof. Stéphan ROUZIERE (Laboratoire de Physique des Solides, Université Paris-Saclay) for his assistance of performing the low temperature WAXD experiments and to Prof. Pascale LAUNOIS (Laboratoire de Physique des Solides, Université Paris-Saclay) for her help of WAXD pattern simulation. I also acknowledge Prof. Alexandre GLOTER (Laboratoire de Physique des Solides, Université Paris-Saclay), Prof. Sandrine PENSEC (Institut Parisien de Chimie Moléculaire, Sorbonne Université), Prof. Zhi-Zhong LI (Laboratoire de Physique des Solides, Université Paris-Saclay) and Prof. Said YAGOUBI (Laboratoire d'Etude des Eléments Légers, CEA), their experimental aid in measurements of electron diffraction, DSC and powder XRD at low temperature did help my thesis a lot. I also benefited from the kind help of my PhD colleague Danilo Rosa Nunes for the crystallography software.

In addition, I should also express my thanks to all members in MATRIX group of Laboratoire de Physique des Solides and in MIM2 group of École Nationale Supérieure de Chimie de Paris, for all encouragement and help they gave.

Accordingly, I am also very thankful for the jury members of my thesis, for their seriously reading my thesis, providing valuable comments and being present at my defense.

Last but not the least, I sincerely appreciate my family for their support and believe in me. I wish to express my sincere appreciation for my beloved girlfriend Xu HE (何煦), thanks for her encouragement during the most helpless time in my life.

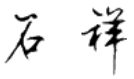

2020 SHI Xiang

Paris, France

I dedicate this thesis to my idol, my mother, to my beloved father and my adorable sister, as well as to my beautiful girlfriend, HE Xu, you are my sunshine!

Contents

Part I

Introduction and Background

Chapter 1

Introduction

Contents

This chapter gives a brief introduction of poly(dimethylsiloxane) (PDMS), together with addressing the research motivation of my thesis. The crystallographic study and the mechanical study of PDMS elastomers at low temperature were reviewed, and the objectives of the present work are presented in the last section.

1.1 What is Poly (dimethyl siloxane) (PDMS)?

Poly(dimethylsiloxane) (PDMS), also known as dimethylpolysiloxane or dimethicone, is by far the most important polymeric compound in silicon industry. The PDMS chain is made up of repeating [–Si(CH$_3$)$_2$O–] units, as shown in **Scheme 1.1**.

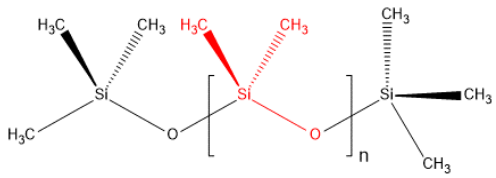

Scheme 1.1 The chemical structure of PDMS (*n* is the number of repeating units)

Like other types of polysiloxanes, PDMS can be obtained from mineral silica and the whole synthetic method[1] is typically divided into five steps: (i) Elemental silicon is first synthesized by reducing silica with carbon at high temperatures; it is followed by (ii) the so-called Direct Process or Rochow Process[2] [3], that essentially produces (CH$_3$)$_2$SiCl$_2$ together with byproducts that are separated by distillation. (iii) The further hydrolysis of dimethyldichlorosilane (CH$_3$)$_2$SiCl$_2$ gives dihydroxy structures that produces cyclic monomers with the basic [–Si(CH$_3$)$_2$O–] repeat unit by condensation (iv). Finally, poly(dimethylsiloxane) (PDMS) is obtained by ring-opening polymerization (v). The corresponding reactions are illustrated as follow:

(i) $SiO_2 + 2C \rightarrow Si + 2CO$

(ii) $Si + 2CH_3Cl \rightarrow (CH_3)_2SiCl_2$

(iii) $(CH_3)_2SiCl_2 + 2H_2O \rightarrow (CH_3)_2Si(OH)_2 + 2HCl$

(iv) $(CH_3)_2Si(OH)_2 \rightarrow [Si(CH_3)_2O]_{3,4} + 2H_2O$

(v) $[Si(CH_3)_2O]_{3,4} \rightarrow [–Si(CH_3)_2O–]_n$

where n is the degree of polymerization.

Commonly, PDMS materials made-up of free linear chains present as transparent oils whose viscosities can be finely tuned by controlling the average chain length. Cross-linked PDMS materials can be synthesized from either commercial silanol-terminated or vinyl-terminated precursor chains by means of condensation[4] [5]

or hydrosilylation[6] [7] reaction, and the obtained PDMS elastomers are often designated as silicone rubber in the literature. All these materials can be employed in a broad temperature range of use (typically −120 ℃ to 150 ℃), which explains their large domain of applications [1]. This is due to some specific features of the (Si–O) bond that are detailed below.

1.1.1 Specificity of the (Si–O) bond

First, the very high dissociation energy (460 kJ/mol) of the (Si–O) bond endows PDMS with unusual thermal stability. Furthermore, PDMS possesses some unique configurational properties due to the inequality of the (Si–O–Si) and (O–Si–O) bond angles, which have been experimentally determined to be respectively about 143 ° and 110 °. As a consequence, an all-trans form conformation would lead to a closing of the chain after ca. 11 units (ca. 360 °/ (143-110 °); see **Figure 1.1-a**). Conformational studies have been conducted by various authors: JA Darsey mapped the conformational energy surface obtained by rotating around the (Si–O) bond by the angles ϕ_1 and ϕ_2 (**Figure 1.1-b**) [8] . He found minima for pair of angles (156 °, 0 °) or (0 °, 204 °) that approximately correspond to the conformation given in **Figure 1.1-c**.

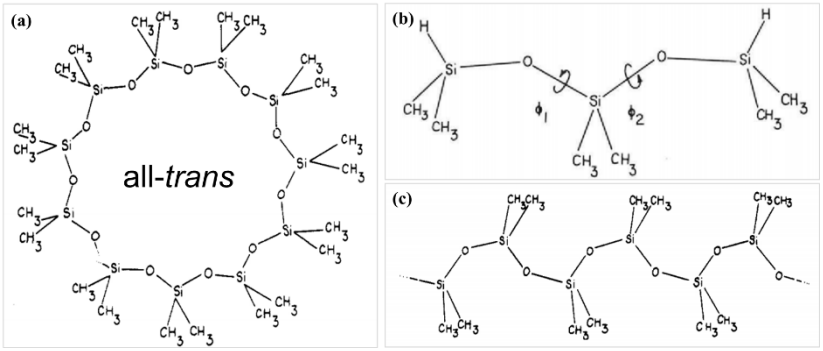

Figure 1.1 (a) all-trans conformation. (b) angles used for mapping the conformational energy surface. (c) conformation of minimum energy[8]

The (Si–O) bond length is 0.164 nm and this reduces steric hindrance between methyl groups (torsional flexibility) [9]. The (Si–O–Si) angle can have value between 140 ° and 180 ° and the barrier of linearization is small (0.3 kcal/mol). PDMS thus presents a high bending flexibility. All these features account for the high dynamic flexibility of the chain and the low value of the glass transition temperature (ca. −125 ℃, see below).

1.1.2 Mechanical properties of PDMS elastomers

As such PDMS elastomers have low tensile strength, poor wear and tear wear properties: as an example, elongation at break hardly exceeds 2. To counteract these drawbacks, fillers are systematically added and finely divided silica powder is most often used. This addition results in a dramatic increase of the mechanical modulus, tear strength and tensile strength. However numerous alternative fillers have been proposed [10] [11] [12] [13] . Silica surface is normally covered by silanol (–Si–OH) groups that strongly interact with the oxygen of the PDMS backbone that explains the increase in viscosity as silica is added to the PDMS oil. In these conditions, a proper dispersion of the silica filler may require industrial mixers and an easier dispersion of the silica particles can be obtained by surface modification (see **Chapter 2**) [31] . The in-situ sol-gel loading process described in **Chapter 2** is also an alternate solution to produce an intimate mixing of a silica phase into the PDMS matrix [7] [11] . The filler content is generally given in **phr**, which means parts per hundred: mass of filler (g) added to 100g of gum.

Silica-filled PDMS elastomers can exhibit "model" Mullins stress softening. **Figure 1.2** presents successive mechanical cycles: red, first cycle, blue, second cycle and yellow, third cycle [14] . The material presents stress softening after a previous cycle up to the maximal elongation reached during this cycle. This effect is general in filled elastomers and is called Mullins effect. It means that if a sample is to be characterized in a reproducible way up to an extension λ_{max}, it must be previously cycled up to λ_{max} at least one time. This procedure was not followed in the present work as we are not really interested by mechanical properties.

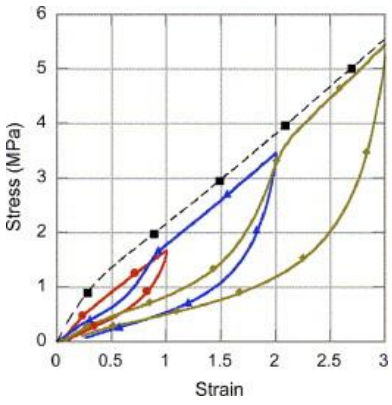

Figure 1.2 Mullins effect in a silica-filled PDMS sample (35phr; [14])

1.1.3 Crystallization and glass transition

Upon cooling, PDMS oils or rubbers readily crystallize at a temperature intermediate between the glass transition temperature (ca. −125 ℃) and the melting temperature (ca. −38 ℃). Preventing crystallization requires high cooling rates (typically 50 ℃/min, ref. [15]). Two melting peaks are most often observed upon warming that are attributed to two populations of crystallites with different average sizes (see below).

The morphology of crystallized PDMS was first studied in 2002 using a scanning electron microscope (SEM) equipped with a cold stage by Sundararajan[16] . **Figure 1.3** show the SEM micrographs of the crystalline PDMS (M_W=38900 and 182600) at different magnifications. Spherulites of nearly 100 μm in size are seen in both low and high molecular weight PDMS.

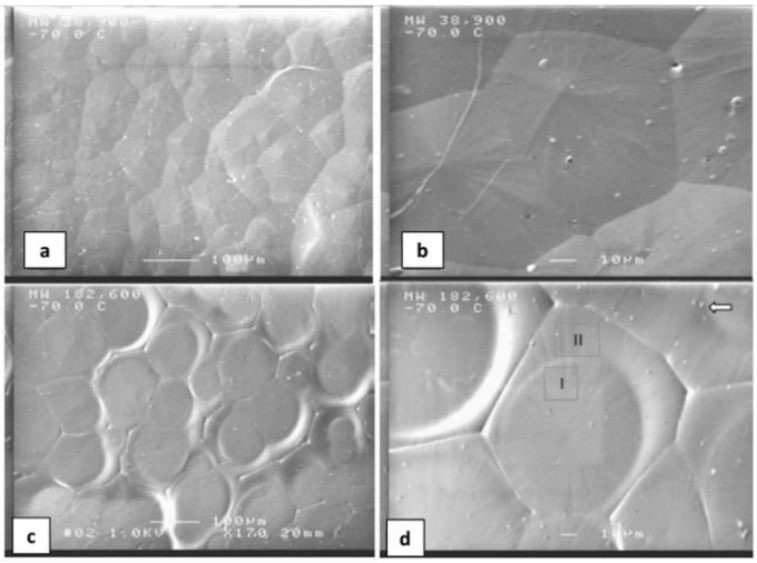

Figure 1.3 SEM micrographs[16] of (a, b) PDMS (MW=38900) and (c, d) PDMS (MW=182600) in lower and higher magnification (scale bar = 100, 10 μm) at −70 °C.

In 1985, Clarson *et al*[17] studied the thermal behavior of cyclic and linear poly(dimethylsiloxane) over the temperature range 103-298 K by differential scanning calorimetry (DSC). The glass transition temperature (T_g) of the linear siloxanes increases from 137 K to 150 K when the number-average of skeletal bonds increases from $n = 10$ to 682 but this last temperature is already reached for $n \approx 100$. As mentioned above, two melting endotherms are reported: the higher temperature endotherm is attributed to the melting of crystallites grown during cooling down. It is

nearly independent upon the chain length and close to $T_{m2} \approx -38$ ℃. Indeed, the temperature at which crystallization starts during cooling is typically intermediate between this value and the glass transition temperature, ca. -80 ℃. Cold crystallization is observed around -90 ℃ during warming-up when polymer chains have recovered enough mobility. Crystallites grown during this last phase melt at $T_{m1} \approx -49$ ℃ and their lower stability is attributed to a smaller size. Cold crystallization can be suppressed by cooling again after reaching a temperature intermediate between T_{m1} and T_{m2}.

Meanwhile, Maus *et al* [18] investigated the crystallization behavior in bimodal PDMS molecular-weight blends consisting of long entangled and short, essentially unentangled, chains by means of DSC and proton NMR spectroscopy. All blends show two melting peaks lower than 240 K, which were attributed to a melting/recrystallization of smaller and/or less stable crystallites. They postulated that the crystallization tendency of PDMS is generally facilitated by the presence of physical or chemical constraints, which can induce chain orientation correlations on the timescale of the lifetime of entanglements.

The influence of fillers and crosslinking density on the crystallization behavior in PDMS elastomers remains somehow controversial but this point is somehow anecdotic as regard to the purpose of this thesis. On the one hand, Aranguren[19] investigated the influence of silica filler and curing on the crystallization of PDMS elastomers based on the DSC measurement: the glass transition temperature was essentially unaffected by silica filler addition or crosslinking. Roland *et al*[20] have demonstrated that the increase of crosslinking density in PDMS networks reduces both the extent of crystallization and the thermodynamic stability of the crystal phase. On the other hand, the calorimetric studies of Dollase *et al*[15] gave an opposite conclusion: the presence of either physical or chemical crosslinks enhances PDMS crystallization from the melt, due to the substantial local chain ordering in the melt that facilitates conformational rearrangements necessary for crystallization. Moreover, Dollase *et al*[21] have also investigated the effect of interfaces on PDMS crystallization and found that the crystallization enhancement does not depend on the specific type of interfacial interaction between the additives and the polymer, but is rather affected by the presence of a surface, which is attributed to entropic interactions in the boundary layer.

Sbirrazzuoli *et al*[22] investigated the effect of crystallization and glass transition on the elastic modulus of PDMS and PDMS silica nanocomposites by means of Dynamic Mechanical Analysis (DMA) and DSC. Illustrative results obtained on an unfilled sample are displayed in **Figure 1.4** ($\tan\delta = E''/E'$, where E'' and E' is the loss modulus and the elastic modulus respectively). When cooling down is rapid, crystallization has no time to proceed before the glass transition is reached. Upon warming (black squares) the elastic modulus E' decreases rapidly at the glass transition temperature and increases again at ca. -100 ℃ when secondary crystallization becomes possible. No such a drop is observed after slow cooling (open triangles) as the sample is already partially crystallized. Between -60 ℃ and -40 ℃ the modulus decrease is due to crystallite melting. These results will be helpful to discuss the present work.

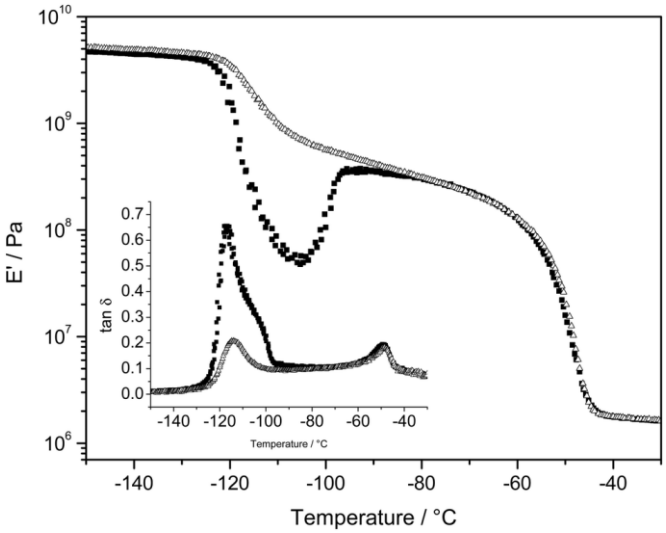

Figure 1.4 Elastic modulus (E′) and tan δ (inset) versus temperature measured on heating an unfilled PDMS elastomer at 1K min^{-1}. Open triangle: heating after slow cooling from the melt. Solid squares: heating after fast cooling from the melt [22].

By combining results from Broad Dielectric Spectroscopy (BDS), Small and Wide-Angle Neutron Scattering (SANS and WANS) and DSC, Lund *et al*[23] have highlighted the relationships between alpha-relaxation dynamics of PDMS and structure evolution during cold crystallization. They evidenced that the conventional amorphous phase disappears during crystal growth and is replaced by that a "constrained amorphous phase" located between crystalline lamellae.

1.2 Role of a preset strain on the crystallization behavior

In 1958, Ohlberg *et al.*[24] were probably the first to study the influence of an applied strain on crystallization. Indeed, their main purpose was to follow the orientation of crystallites grown under strain and to evaluate crystallinities in a silica-filled PDMS elastomer. Values for this last parameter are in the range $0.5-0.6$, which is typically what is now reported. They also reported a strong increase of the crystallization temperature from ca. -55 ℃ in the quiescent state to ca. -14 ℃ for a draw ratio 6.3. Crystallization temperature is actually not a very pertinent parameter by itself as it depends upon the cooling rate, cross-link density… However, -14 ℃ is well-above the equilibrium melting temperature in the quiescent state which unambiguously demonstrates an increase of the melting temperature with elongation. The most interesting point is their report of an anomalous change of X-ray diffraction patterns with increasing elongation: it is a point that has gone somehow unnoticed and that is clearly seen in **Figure 1.5** (-60 ℃; compare patterns at draw ratios 2.4 and 6.2).

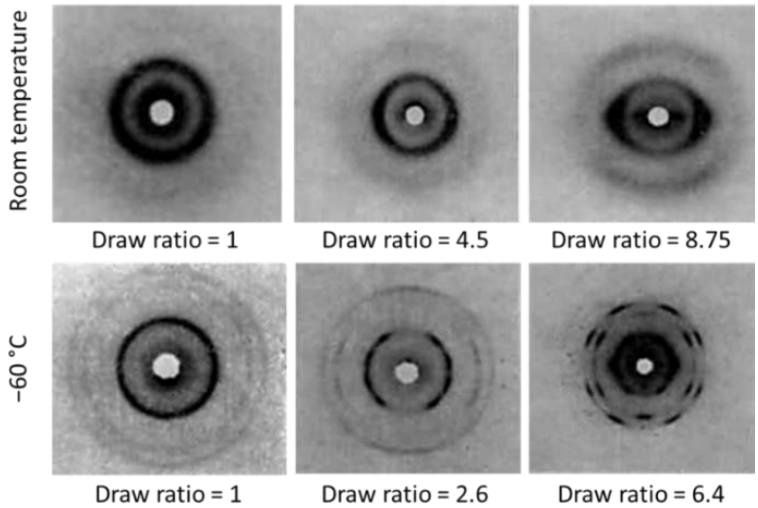

Figure 1.5 X-ray diffraction patterns[24] of silicone rubber measured in amorphous and crystalline state under different draw ratio. Extension axis is vertical.

Room temperature patterns are also interesting to discuss. They essentially consist in an inner intense amorphous halo (now mainly associated to inter-chain correlations) followed by a weaker ring (now mainly associated to intra-chain correlations). Although images are of rather poor quality, an equatorial intensity reinforcement is clearly seen at a draw ratio 4.5 that become more finely structured at very high elongation (8.75).

In the second section of this study, Warrick[25] performed tension-temperature measurements with a low-temperature apparatus. It was found that the silica filled

PDMS elastomers exhibit an atypical thermo-elastic behavior shown in **Figure 1.6**. The retractive force shows a dramatic and sudden rise during cool-down which Warrick attributed to crystallization without giving further proof. One difficulty arises from the fact that all measurements are made during cool-down that are out-of-equilibrium conditions and as mentioned above the "incipient crystallization temperature" is not a really pertinent parameter. Elucidating the relation between the stress rise and crystallization is one objective of the present work.

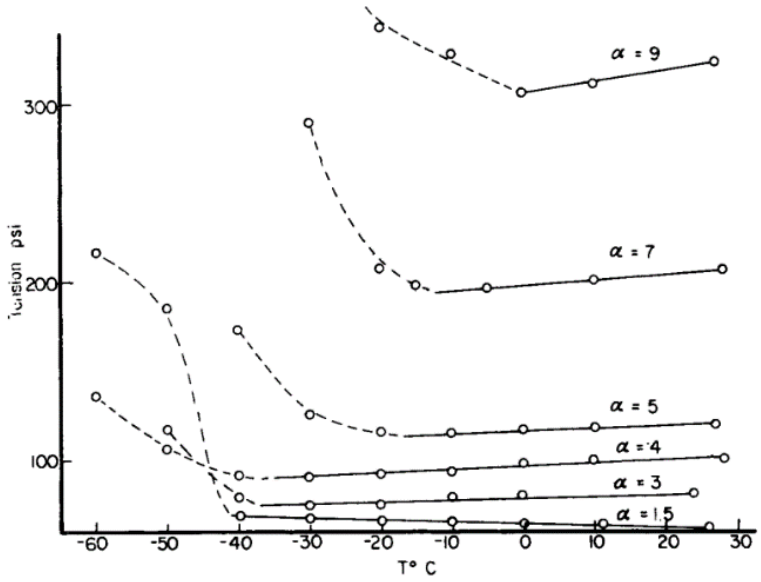

Figure 1.6 Tension of silica filled PDMS samples as a function of temperature[25], α is the draw ratio.

1.3 The enigma of the PDMS crystal structure

The first investigation of the crystalline structure was performed by Damaschun[26] in 1962. It was based on the analysis of a diffraction pattern taken at −90 ℃ on a highly stretched silicone rubber (draw ratio of 5; 35% Aerosil silica). **Figure 1.7-a** is the drawing provided by this paper to illustrate the obtained X-ray fiber pattern. We see that it clearly corresponds to the photograph "−60 °C; draw ratio = 6.4" in **Figure 1.5**. The draw axis is along the vertical and is supposed to correspond to the chain axis. Due to the absence of a 010 reflection this axis was assumed to be a 2_1 screw axis. The chain has been accordingly attributed a two-fold helical conformation (**Figure 1.7-b**, see below). In agreement with the 2_1 symmetry a monoclinic unit cell was proposed with parameters a = 1.3 nm, b = 0.83 nm, c = 0.775 nm, and β = 60 °. Possible space groups are P 2_1/m and P 2_1/c. Based on the estimated density of the crystalline phase, a loose 2_1 helical chain conformation was proposed (**Figure 1.7-b**): there are six

monomers per unit cell among which three are independent (the other three are symmetry-related to these ones).

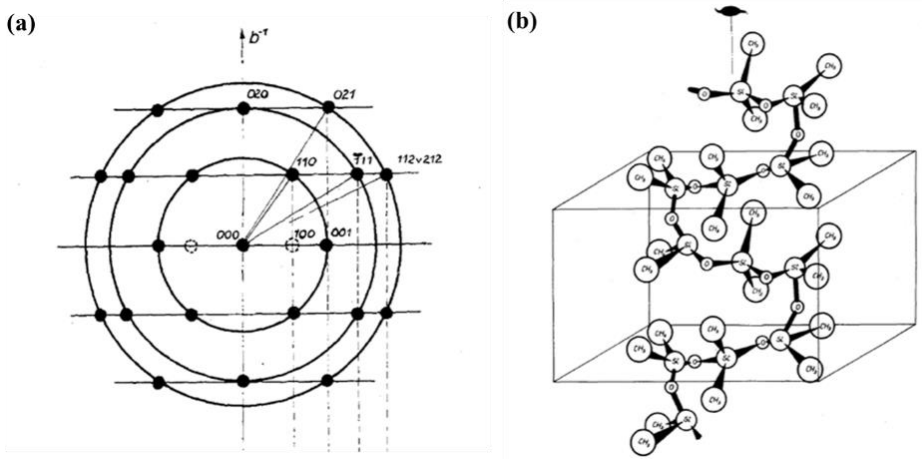

Figure 1.7 (a) Drawing used to represent the X-ray diffraction pattern. (b) The proposed chain conformation in the crystalline state. Both were obtained in ref. [26] .

In 1980, Sundararajan *et al.*[27] performed some measurements on linear PDMS crystallized from solution in n-heptane and toluene. They observed that lower molecular oils would give crystals of better quality than very high molecular weight ones. The observed position of nine diffraction lines could be correctly fitted with Damaschun's monoclinic unit cell (see **Table 1.1**).

Table 1.1 Comparison of the observed and calculated d-spacings; the indexation is based on Damaschun's monoclinic cell (the monoclinic axis is the *c*-axis in the table) [27]

d(obsd), Å	*d*(calcd), Å	*hkl* indices
6.80	6.71	010
4.11	4.15	002
3.54	3.53	320, 210, 012
2.97	2.99	312
2.71	2.69	121, 322, 212, 103
2.40	2.40	220, 113
2.26	2.25	223
2.07	2.08	222, 004
1.99	2.00	130, 321, 403, 123 114, 014

The first questioning about Damaschun's two-fold model came from a solid-state ^{13}C and ^{29}Si NMR study by Schilling *et al.*[28] in 1991. The observation of a single resonance for both the ^{13}C and ^{29}Si nuclei was totally inconsistent with Damaschun's proposal of three independent monomers per unit cell. As shown in the projections represented in **Figure 1.8**, the three corresponding silicon atoms have different

environment and the two-fold helical, ribbon-like chain conformation should thus give rise to multiple resonances.

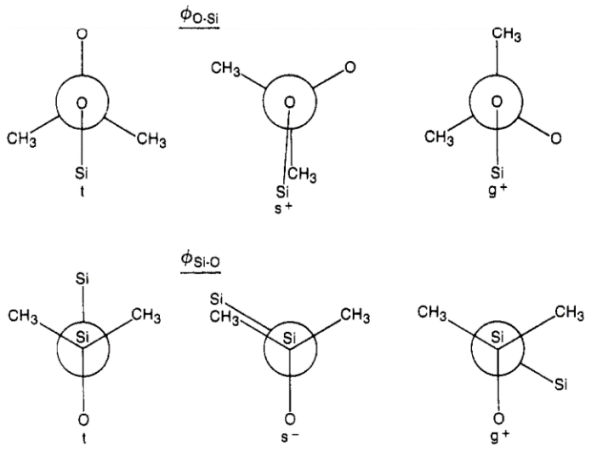

Figure 1.8 Newman projections along the O-Si and Si-O bonds for the crystalline conformation of PDMS suggested by Damaschun.[28]

Later in 2000, Albouy[29] analyzed fibber patterns at low elongation as he had only unfilled PDMS rubbers at disposition at first (in that case the maximal draw ratio that can be applied does not exceed 2). He observed a quite different diffraction pattern, reproduced in **Figure 1.9**, which corresponds to a sample drawn to an extension of 1.5.

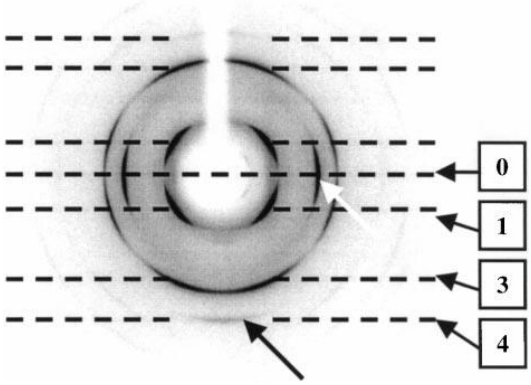

Figure 1.9 Low temperature X-ray pattern[29] of a 30 wt% silica filled PDMS rubber submitted to vertical extension (draw ratio λ=1.5; exposure time, 20 min).

The black arrow in **Figure 1.9** points to the first azimuthal reflection: we call $\vec{c}$ the crystallographic axis that aligns along the vertical stretching direction and the indexation of this reflection is (004). Patterns taken at wider angles reveal that only the (008) reflection can be also observed. The absence of $(00l)$ reflection with $l \neq 4n$ indicates that the $\vec{c}$ axis corresponds to a 4_1 screw axis. It points to a tetragonal space group and all line positions can be precisely accounted for with cell parameters of a = b = ca. 0.83 nm and c (fiber axis) = ca. 1.20 nm (precise values are given for two

different temperatures [29]: see **Table 1.2**). It is to notice that the angular positions of the intensity reinforcements seen in **Figure 1.9** are also precisely accounted for. Reflections hkl that do not satisfy $h + k + l = 2n$ are furthermore systematically absent which indicates a centered tetragonal lattice. The crystalline density was estimated from X-ray absorption measurements: values of 1.16 g/cm^3 at 183K and 1.21g/cm^3 at 59K are reported. Both determinations point to eight monomers per unit cell and the most straightforward space group that satisfies this condition is $I\,4_1$.

Table 1.2 Comparison between experimental and measured d-spacings and angular positions δ of intensity reinforcements (183K; a = 0.835nm, c = 1.192nm)

(h,k,l)-indices	Experimental d_{hkl} (nm)	Calculated d_{hkl} (nm)	Experimental δ angle (deg.)	Calculated δ angle (deg.)
(0,1,1)	0.685	0.684	54.9	54.9
(0,2,0)	0.417	0.417	88.9	90
(1,2,1)	0.358	0.356	72.8	72.2
(0,1,3)	0.358	0.358	19.4	22.5
(0,0,4)	0.298	0.298	0.6	0
(1,2,3)	0.272	0.272	43.3	44.6
(1,3,2)	0.242	0.241	65.1	64.8
(0,2,4)	0.242	0.242	31.2	31
(0,3,3)	0.228	0.228	53.5	52.6
(0,4,0)	0.209	0.209	89.2	90

A single monomer unit will generate eight equivalent monomers through the symmetry operations of the space group: this is consistent with the NMR results [28]. One obtains two chains related by the centering condition and running along the $\vec{c}$ axis. The helical pitch of 1.2 nm requires a rather extended conformation as proposed in **Figure 1.10**.

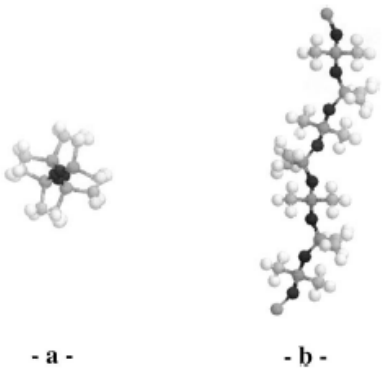

Figure 1.10 Model for the fourfold helical conformation of the PDMS chain. (a) top view, (b) side view. Oxygen atoms are in black [29]

When comparing **Table 1.1** with **Table 1.2**, we see that the line positions can be accounted for by Damaschun's and Albouy's unit cells. It is explicitly assumed by Albouy that the structure is similar in both cases and that differences in the diffraction

patterns only reflect a change in the crystalline texture. This change would give rise to the apparent 2_1 symmetry.

In 2013, Tosaka *et al.*[30] were the first to publish evidences of a continuous transformation of the diffraction patterns in the PDMS elastomer with increasing draw-ratio: see **Figure 1.11**.

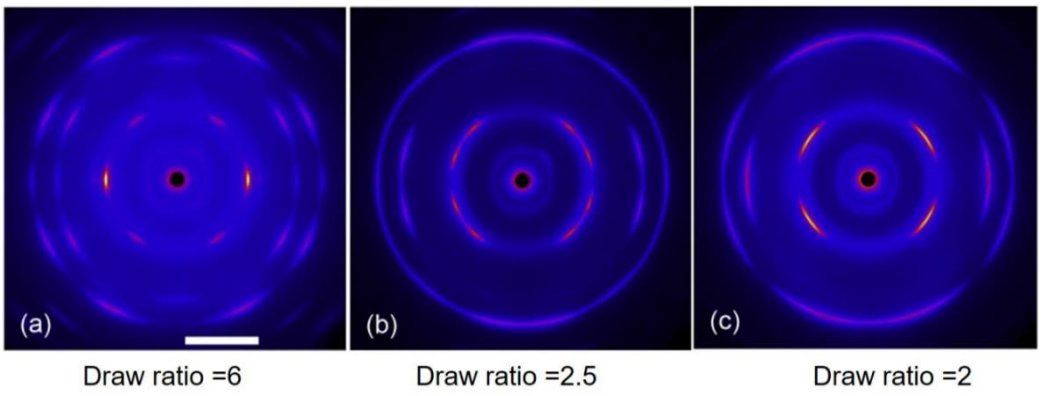

Figure 1.11 WAXD patterns[30] of cross-linked PDMS samples crystallized at −90 °C (scale bar = 10 nm^{-1}). Stretching direction is vertical. Cu Kα radiation was used as the X-ray source.

They also reported the previous observation made by Ohlberg *et al.*[24] of the apparition of a strong intensity reinforcement localized in equatorial position at room temperature at higher extension: see **Figure 1.12-a**; it is clear that this reinforcement is localized close to the "amorphous halo" though at a different position (see **Figure 1.12-b**). It is attributed by these authors to a "mesomorphic" phase that develops at higher draw ratios. The most intense crystalline spot in **Figure 11-a** ("yellow" spot) grows at this position and there is thus a relation between this "mesomorphic" phase and the crystalline one.

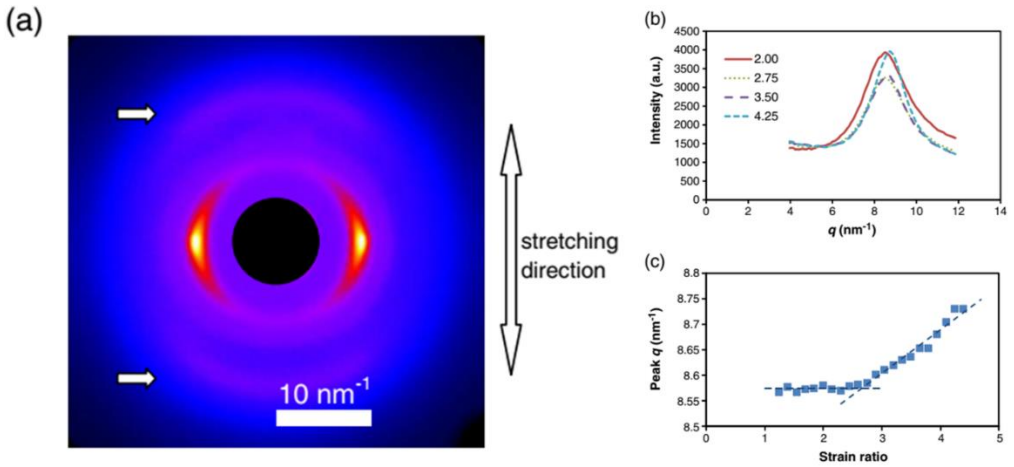

Figure 1.12 (a) Diffraction pattern of a silicone rubber sample stretched to a draw-ratio of 6 at room temperature; (b) equatorial intensity profiles at various draw ratios (c) peak position as a function of draw ratio [30]

They interpreted the difference in diffraction patterns between low and high strain in terms of polymorphism: the ***β* form** crystal was assigned to the low strain phase, and similar to the crystal structure model reported by Albouy[29], while the ***α* form** was associated to the structure proposed by Damaschun[26]. The *d*-spacings for both phases are similar and the authors perceived it actually as problematic: the explanation they proposed is rather intricate.

Recently, Tosaka deepened his structural analysis in association with Tashiro[31]. They used the technique of the selected area electron diffraction (SAED) to explore the supposed crystal polymorphism. Examples of single crystals grown on the carbon grid and the associated diffraction patterns are displayed in **Figure 1.13**.

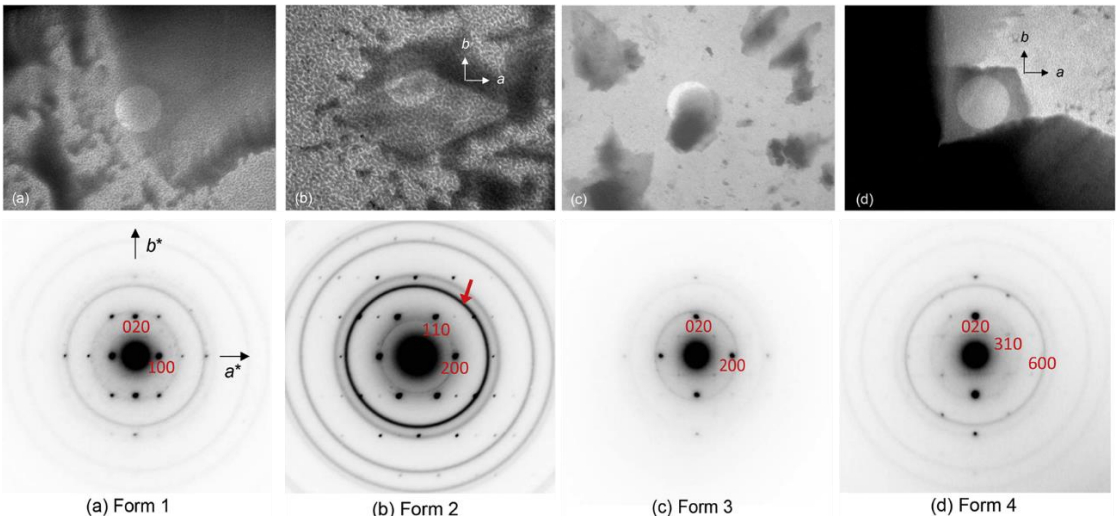

Figure 1.13 TEM images and the corresponding SAED patterns (taken at the bright circular area with diameter of about 10 μm) of the PDMS single crystals measured below −100 °C.

These diffraction patterns were analyzed in terms of four different crystal structures. Such a rich polymorphism is indeed intriguing and it is our opinion that each assignment is based on limited information (essentially one diffraction plane). We give in **Table 1.3** the crystallographic parameters proposed of each crystalline form: $\alpha = \beta = \gamma = 90°$ in all cases including orthorhombic cells (the term "fiber axis" refers to the polymer chain direction). Computed densities are 1 g/cm^3 for Form 1 and Form 4, 1.6 g/cm^3 for Form 2 and Form 3. The density value determines by Albouy for the crystalline phase is compatible with a mixture of the different forms. The chain

conformations proposed for each crystalline form are based on simulation and are highly speculative. They can be found in their publication.

Table 1.3 Four-form crystal structure model for PDMS[31]

Crystal structure	Space group	Cell parameters*		
		a	***b***	***c***
Form 1	$P\ 2_1/b$ (No. 14)	0.69nm	0.84 nm	0.84 nm (fiber axis)
Form 2	$P\ 2_12_12_1$ (No. 19)	0.88nm	0.41 nm	0.84 nm (fiber axis)
Form 3	$I\ \bar{4}$ (No. 82)	0.85 nm	0.85 nm	0.84 nm (fiber axis)
Form 4	C m (No. 8)	1.45 nm	0.83 nm	1.20 nm (tilted)

* ***a*** and ***b*** were determined by SAED pattern while ***c*** was determined by WAXD pattern

Quite recently, Li's group[32] used in situ synchrotron radiation wide-angle X-ray scattering technique to study the structural evolution of silica filled PDMS during uniaxial tensile deformation at temperatures from −40 to −65 ℃. They analyzed their results in terms of polymorphism following closely Tosaka et *al.* analysis without further proof.

1.4 Objectives and Aims

The main objective of this work is trying to elucidate the enigma of the crystalline structure of PDMS, and to find out an explanation for the change in diffraction patterns with strain. The stress-upturn during cooling down of pre-stretched samples is also of interest.

Chapter 2 will briefly present different synthesis routes that were explored to prepare unfilled and filled samples; a rapid mechanical characterization was performed in order to find PDMS elastomeric materials that can withstand large elongation as this step is crucial to reproduce Tosaka's observations.

More detailed tensile/WAXS measurement at room temperature are presented for some selected samples in **Chapter 3**. In particular, the effect of the silica filler on the strain state of the amorphous phase during extension is discussed. Interesting results are obtained as regard to the strain amplification factor.

A fundamental question is to know if the change in the diffraction patterns with increasing extension is due to (1) a change in the crystalline texture keeping the same crystalline structure (2) a change in the crystal structure implying polymorphism. For this purpose, diffraction and mechanical measurements were simultaneously performed

during cooling and warming sequences on samples submitted to static elongation: this is the object of **Chapter 4**. **Chapter 5** is dedicated to the study of the anomalous low-temperature thermoelastic behavior observed in stretched PDMS during cooling and heating.

Chapter 6 is a crystallographic study where we tried to adjust experimental line intensities with a structural model. It is completed by some electron microscopy results. Consideration about some orientation effects observed in cooled PDMS oils are also added.

The subject of my thesis was originally the study of some liquid-crystal polymers. The west wing of the Laboratory was closed six months for renovation and during this time, I went to Chimie ParisTech, Paris to analyze X-ray characterizations that had been performed on two cholesterol-based organogelators: this is object of **Chapter 7.**

Finally, **Chapter 8** summarizes all the results and gives suggestions for future work.

References

[1] Mark, J. E., Schaefer, D. W., & Lin, G. (2015). The polysiloxanes. Oxford University Press.

[2] Stark, F. O., Falenda, J. R., & Wright, A. P. (1982). Silicones in comprehensive organometallic chemistry. vol, 22, 305.

[3] Rochow, E. G. (1987). Silicon and Silicones: about stone-age tools, antique pottery, modern ceramics, computers, space materials, and how they all got that way. Springer Verlag.

[4] Schmidt, D. F., Clément, F., & Giannelis, E. P. (2006). On the Origins of Silicate Dispersion in Polysiloxane/Layered-Silicate Nanocomposites. *Advanced functional materials*, 16(3), 417-425.

[5] Bokobza, L., & Rahmani, M. (2009). Carbon nanotubes: Exceptional reinforcing fillers for silicone rubbers. *KGK. Kautschuk, Gummi, Kunststoffe*, 62(3), 112-117.

[6] Patel, S. K., Malone, S., Cohen, C., Gillmor, J. R., & Colby, R. H. (1992). Elastic modulus and equilibrium swelling of poly(dimethylsiloxane) networks. *Macromolecules*, 25(20), 5241-5251.

[7] Dewimille, L., Bresson, B., & Bokobza, L. (2005). Synthesis, structure and morphology of poly(dimethylsiloxane) networks filled with in situ generated silica particles. *Polymer*, 46(12), 4135-4143.

[8] Darsey, J. A. (1990). Self-consistent-field conformational energy study and configurational statistics of poly(dimethylsiloxane). *Macromolecules*, 23(25), 5274-5278.

[9] Voronkov, M. G., Mileshkevich, V. P., & Yuzhelevskii, Y. A. (1978). The siloxane bond. Consultants Bureau, New York, 196.

[10] Paul, D. R., & Mark, J. E. (2010). Fillers for polysiloxane ("silicone") elastomers. *Progress in polymer Science*, 35(7), 893-901.

[11] Rajan, G. S., Sur, G. S., Mark, J. E., Schaefer, D. W., & Beaucage, G. (2003). Preparation and characterization of some unusually transparent poly(dimethylsiloxane) nanocomposites. *Journal of Polymer Science Part B: Polymer Physics*, 41(16), 1897-1901.

[12] Osman, M. A., Atallah, A., Müller, M., & Suter, U. W. (2001). Reinforcement of poly(dimethylsiloxane) networks by mica flakes. *Polymer*, 42(15), 6545-6556.

[13] Wang, S., Long, C., Wang, X., Li, Q., & Qi, Z. (1998). Synthesis and properties of silicone rubber/organomontmorillonite hybrid nanocomposites. *Journal of Applied Polymer Science*, 69(8), 1557-1561.

[14] Hanson, D. E., Hawley, M., Houlton, R., Chitanvis, K., Rae, P., Orler, E. B., & Wrobleski, D. A. (2005). Stress softening experiments in silica-filled polydimethylsiloxane provide insight into a mechanism for the Mullins effect. *Polymer*, 46(24), 10989-10995.

[15] Dollase, T., Spiess, H. W., Gottlieb, M., & Yerushalmi-Rozen, R. (2002). Crystallization of PDMS: The effect of physical and chemical crosslinks. *EPL* (*Europhysics Letters*), 60(3), 390.

[16] Sundararajan, P. R. (2002). Crystalline morphology of poly(dimethylsiloxane). *Polymer*, 43(5), 1691-1693.

[17] Clarson, S. J., Dodgson, K., & Semlyen, J. A. (1985). Studies of cyclic and linear poly (dimethylsiloxanes): 19. Glass transition temperatures and crystallization behaviour. *Polymer*, 26(6), 930-934.

[18] Maus, A., & Saalwächter, K. (2007). Crystallization Kinetics of Poly (dimethylsiloxane) Molecular-Weight Blends—Correlation with Local Chain Order in the Melt? *Macromolecular Chemistry and Physics*, 208(19-20), 2066-2075.

[19] Aranguren, M. I. (1998). Crystallization of polydimethylsiloxane: effect of silica filler and curing. *Polymer*, 39(20), 4897-4903.

[20] Roland, C. M., & Aronson, C. A. (2000). Crystallization of polydimethylsiloxane end-linked networks. *Polymer Bulletin*, 45(4-5), 439-445.

[21] Dollase, T., Wilhelm, M., Spiess, H. W., Yagen, Y., Yerushalmi-Rozen, R., & Gottlieb, M. (2003). Effect of interfaces on the crystallization behavior of PDMS. *Interface Science*, 11(2), 199-209.

[22] Bosq, N., Guigo, N., Persello, J., & Sbirrazzuoli, N. (2014). Melt and glass crystallization of PDMS and PDMS silica nanocomposites. *Physical Chemistry Chemical Physics*, 16(17), 7830-7840.

[23] Lund, R., Alegria, A., Goitandia, L., Colmenero, J., Gonzáez, M. A., & Lindner, P. (2008). Dynamical and structural aspects of the cold crystallization of poly(dimethylsiloxane)(PDMS). *Macromolecules*, 41(4), 1364-1376.

[24] Ohlberg, S. M., Alexander, L. E., & Warrick, E. L. (1958). Crystallinity and orientation in silicone rubber. I. X-ray studies. *Journal of Polymer Science*, 27(115), 1-17.

[25] Warrick, E. L. (1958). Crystallinity and orientation in silicone rubber. II. Physical measurements. *Journal of Polymer Science*, 27(115), 19-38.

[26] Damaschun, G. (1962). Röntgenographische Untersuchung der Struktur von Silikongummi. *Kolloid-Zeitschrift und Zeitschrift für Polymere*, 180(1), 65-67.

[27] Sundararajan, P., Hamer, G., & Coucher, M. (1980). Low-temperature crystallization of poly(dimethylsiloxane) from solution. *Macromolecules*, 13(4), 971-973.

[28] Schilling, F. C., Gomez, M. A., & Tonelli, A. E. (1991). Solid-state NMR observations of the crystalline conformation of poly(dimethylsiloxane). *Macromolecules*, 24(24), 6552-6553.

[29] Albouy, P. A. (2000). The conformation of poly(dimethylsiloxane) in the crystalline state. *Polymer*, 41(8), 3083-3086.

[30] Tosaka, M., Noda, M., Ito, K., Senoo, K., Aoyama, K., & Ohta, N. (2013). Strain-and temperature-induced polymorphism of poly (dimethylsiloxane). *Colloid and Polymer Science*, 291(11), 2719-2724.

[31] Tosaka, M., & Tashiro, K. (2018). Crystal polymorphism and structure models of Poly (dimethylsiloxane). *Polymer*, 153, 507-520.

[32] Zhao, J., Chen, P., Lin, Y., Chang, J., Lu, A., Chen, W., & Li, L. (2018). Stretch-induced crystallization and phase transitions of poly(dimethylsiloxane) at low temperatures: An in-situ synchrotron radiation wide-angle X-ray scattering study. *Macromolecules*, 51(21), 8424-8434.

[33] Zhao, J., Chen, P., Lin, Y., Chen, W., Lu, A., Meng, L., & Li, L. (2020). Stretch-Induced Intermediate Structures and Crystallization of Poly (dimethylsiloxane): The Effect of Filler Content. *Macromolecules*, 53(2), 719-730.

Part II

Experimental Section

Chapter 2

Synthesis of Poly(dimethylsiloxane) Elastomeric Composites

Contents

2.1 Introduction

A lot of approaches were undertaken to prepare elastomeric networks, which thus endow PDMS materials rubberlike elasticity for further application in industry. The most popular precursors for producing PDMS elastomer are reactive polymers with end-link functional groups, which can be used with a crosslinker to produce high performance elastomeric materials.

The most frequent synthesis routes for PDMS elastomers are starting either from hydroxyl-terminated (Si-OH) or vinyl-terminated (Si- or O-CH=CH_2) precursor chains. A tin-based catalyst is most often used in the first case and a platinum-based one for the second case. For example, Schmidt *et al* [4] is using hydroxyl-terminated PDMS to prepare a network structure with tetraethoxysilane (TEOS) as cross-linker and tin (II) 2-ethylhexanoate as catalyst [4]. Patel *et al.* [3] is cross-linking a vinyl-terminated PDMS in the bulk using tetrakis(dimethylsiloxy)silane as cross-linker in the presence of the catalyst cis-dichlorobis(diethyl sulfide)-platinum(II); curing time was 72hrs at 35 ℃. In another example Dewimille *et al.* [4] are mixing vinyl-terminated precursor chains and 1,3,5,7-tetramethylcyclotetrasiloxan (cross-linker) with the milder catalyst Platinum (0)-1,3-divinyl-1,1,3,3-tetramethyldisiloxane complex solution (Karstedt's Catalyst); curing time is 24hrs at 80 ℃. In the work of Takeuchi *et al.* [5], both hydroxyl-terminated and vinyl-terminated PDMS precursors were used to fabricate the PDMS networks. In addition, Chaumont *et al.* [6] [7] synthesized silicon rubber at high temperature from vinyl-terminated PDMS by free-radical crosslinking adding of dicumyl peroxide (DCP). Other methods involve complicated precursor mixtures, for example, the most widely used product Sylgard® 184 from Dow Corning. Due to its simplicity of use, this bi-component product (base and curing agent) is widely used [8] [14]. Except these synthesis routines, radiation-induced crosslinking, including electron-beam [15] [16] and gamma irradiation [17] [18] was also applied to fabricate elastomers. Photo-initiated thiol-ene cross-linking has also been used for the synthesis of elastomeric structure in an environmental friendly way [19] [24].

Due to the poor mechanical properties of the neat PDMS, numerous kinds of fillers can be incorporated in order to improve their properties [25]. Among these fillers, silica nanoparticles are the most popular due to their good compatibility with the PDMS matrix. However, the addition of the silica powder into the PDMS oil results in a viscosity increase and it may be difficult to achieve a very good dispersion without

specific mixers. As regard to the lack of this type of apparatus in the Laboratory, we turned to silica with modified surface or in situ generated silica by sol-gel method [4] [26] Other fillers, like CNT [4] [27], graphite [28], carbon black [28], clay particles [30], mica flakes [31], layered silicate [32], organomontmorillonite [33], palygorskite [34] and oligomeric silsesquioxane [35], are also reported.

We present in this chapter the synthesis of silicone rubbers based on different PDMS precursor chains and fillers; their mechanical properties are compared with a particular accent on the elongation at break. As stressed in **Chapter 2**, our goal is to obtain samples with elongation at break in excess of 5.

2.2 Experimental section

2.2.1 Materials

For the whole experiment, the chemical reagents are listed in **Table 2.1**.

Table 2.1 the list of chemical reagents

Chemical reagent	CAS-No.	Vendor
PDMS precusor chains		
silanol-terminated (DMS-S21 and DMS-S27)	70131-67-8	Gelest Inc.
vinyl-terminated (DMS-V25, DMS-V31R and DMS-V33)	68083-19-2	
poly(hydromethyl-co-dimethylsiloxane) (HMS-301)	68037-59-2	
Sylgard®184		
crosslinking agent		
tetraethoxysilane (TEOS)	78-10-4	Sigma-aldrich
tetrakis(dimethylsiloxy)silane (A4)	17082-47-2	Gelest Inc.
catalyst		
Stannous-2-ethylhexanoate	301-10-0	Sigma-aldrich
chloroplatinic acid (0.1mM isopropanol solution)*		
platinum/divinyltetramethyldisiloxane complex (SIP6830.3)	68478-92-2	Gelest Inc.
dibutyltin dilaurate (DBTDL)	77-58-7	Sigma-aldrich
filler		
hexamethylsilazane-treated silicon dioxide (SIS6962.0)	68909-20-6/7631-86-9	Gelest Inc.
multiwall carbon nanotubes (NC7000 series)		Nanocyl

* it was synthesized by dissolving chloroplatinic acid hydrate into isopropanol

2.2.2 Swelling experiments

Swelling experiments were simply used to evaluate the soluble fraction, that is the amount of polymer chains that remained non cross-linked. The weight of PDMS sample m_0, is first measured and the sample is allowed to swell for 3 days in toluene

with daily change of toluene to permit maximum soluble components extraction. The sample is then put in a series of methanol/toluene mixtures with increasing methanol ratio to remove the solvent. It is then dried in a vacuum oven, and its weight after extraction m_1 is measured. The soluble fraction w_{sol} is calculated by the equation

$$w_{\mathrm{sol}} = \frac{m_0 - m_1}{m_0} \tag{2.1}$$

2.2.3 Casting mold and sol-gel loading method

In our experiments, three kinds of Teflon molds were used to fabricate flat film sample and dumbbell shape sample. **Figure 2.1** displays two molds: the dimension of the round-one is 10 cm diameter × 0.1 cm in depth. The volume of the mold is given and small so that it is helpful for the fabrication of small quantities of films. The other one is rectangular 25cm in length, 0.1cm in depth and 17 cm in width. The actual length can be adjusted between 0 and 21.5cm by moving the two casting bars. It can be used to make larger films or films with a very small thickness.

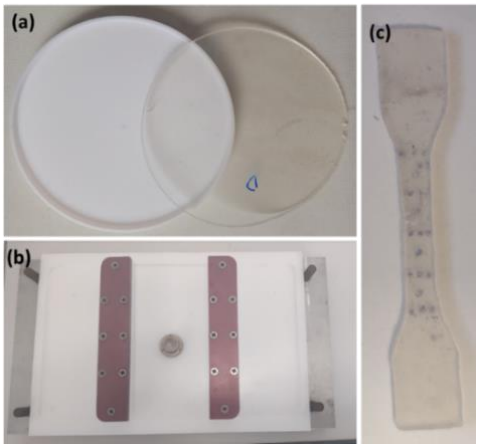

Figure 2.1 Elastomeric sheet obtained by (a) round-shape and (b) rectangle mold; (c) dog bone specimen.

After curing, dog-bone shape samples can be cut away with a steel puncher (see **Figure 2.1c**). In order to make films with a homogeneous width, the horizontality of the mold can be adjusted with the four lateral screws.

Slippage of the sample out of the holding grips during mechanical test can be a problem. It can be overcome by preparing dumbbell shape specimens (see **Figure 2.2d**). For this purpose, we also used a home-built double tunnel filling mold shown in **Figure 2.2**. The central film width is fixed to 0.75mm to limit the absorption of X-rays for

diffraction experiments (the optimal thickness at a wavelength 0.1542nm is ca. 0.3mm). However, if the viscosity of the mixture is too high, bubbles have difficulties to escape; as a result, it is better to spend a lot of time removing all bubbles and most solvent of the mixture before putting the mold in the oven for final curing. This is done using a rotary evaporator.

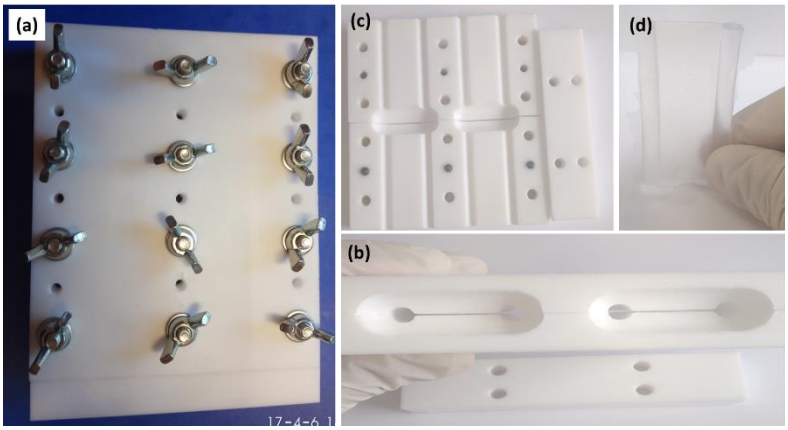

Figure 2.2 The double tunnel filling mold: (a) side view; (b) top view and (c) inner view; (d) dumbbell sheet.

An atmosphere saturated with water is needed for the in-situ generation of silica filler by the sol-gel process in the neat PDMS networks. After swelling in the TEOS in the presence of a tin catalyst (see below) for a set time, the film was laid in the upper place of the glass box with some water at the bottom. The box was then sealed and put in an oven at 30 ℃ for 24 hours.

2.3 Whole strategy

Based on the solution casting method, all PDMS elastomers were fabricated mainly in three steps, schematically shown in **Scheme 2.1**.

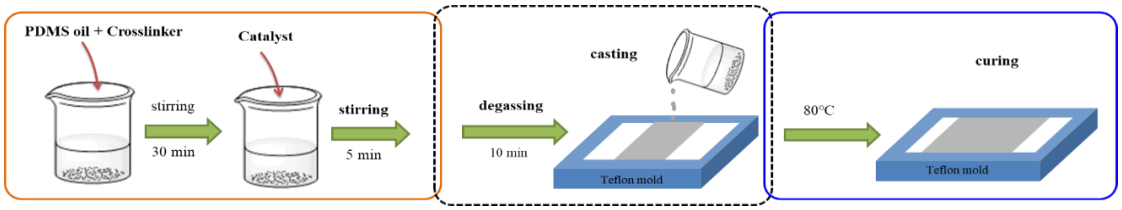

Scheme 2.1 The solution casting method

(1) in order to have a homogeneous dispersion, PDMS precursors are premixed with the cross-linker with some good solvent, like toluene, followed by the addition of the catalyst for a relatively short period.

(2) Degassing and casting steps are very crucial due to the great negative effect on the mechanical properties of bubbles created inside the mixture, especially for the case of fabricating dumbbell-shaped PDMS elastomeric specimen;

(3) The final curing was usually performed in an oven with optimum curing time.

In this section, different synthesis routines are carried out, and tensile tests are performed to test the mechanical properties of synthesized film. These results are compared and assessed to find the best strategy to obtain PDMS elastomeric materials with good mechanical properties (essentially elongation at break).

The whole strategy can be divided into two section: first is to the synthesis of neat and filled PDMS elastomers; in a second step, the results obtained from tensile test are compared in order to choose the proper solution to fabricate PDMS elastomers with good mechanical properties. It corresponds to a trial and test process that proved not straightforward.

It is known that mixing silica powder and the PDMS oil during the first steps of the synthesis is a difficult task as the mixture becomes highly viscous. In order to circumvent this difficulty, we first decided to follow the sol-gel loading method described by Liliane Bokobza (see below). As she also presented multiwall carbon nanotubes as a highly efficient filler at very low concentration, we also decided to try this method. In both cases silanol-terminated PDMS with high and low molecular weight are cross-linked in presence of a tin catalyst. However, both methods seemingly gave not satisfying results and we turned to commercial Sylgard® 184. The obtained film is more rigid and with low elongation at break which is not good for our purpose. Afterwards, we turned to vinyl-terminated PDMS with high molecular weight and a platinum catalyst. The neat PDMS behaves better when compared with networks synthesized from silanol-terminated PDMS oil, but it still cannot meet our later experimental need. Therefore, filled PDMS elastomers were fabricated by physical mixing with surface modified silica or in-situ sol-gel generation of silica, expecting to achieve good dispersion of the fillers in the soft matrix. The result shows great enhancement of their mechanical property, which turns out to be best choice of method to obtain PDMS elastomer with good mechanical properties.

2.4 Preparation of unfilled PDMS networks

Neat PDMS elastomers were fabricated from polydimethylsiloxane precursor chains by means of different multifunctional cross-linking agent in the presence of corresponding catalysts, according to published research papers.

2.4.1 from silanol-terminated PDMS precursor

Unfilled elastomer networks were synthesized using silanol-terminated poly(dimethylsiloxane) precursor chains (M_W=18000) and a tetrafunctional alkoxysilane cross-linker. The cross-linking reaction involved is a condensation reaction that produces ethanol as a by-product (that rapidly evaporates out of the sample). It is catalyzed with a tin catalyst (see below).

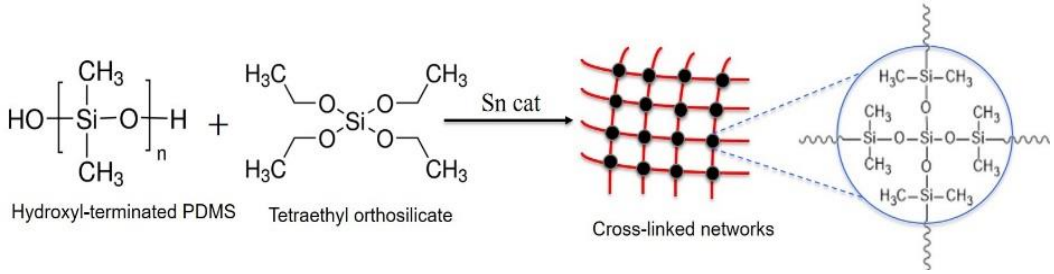

13.12 g silanol-terminated PDMS oil is mixed with cross-linking agent TEOS (tetraethyl orthosilicate; see amount below) in toluene for 30 minutes; the tin catalyst (stannous-2-ethyl-hexanoate) is then added to the mixture in the extent of 1.2 g/100 g of chains, under magnetic stirring for another 5 minutes. The reacting mixture is slowly cast into a rectangle Teflon mold and left 30 minutes at room temperature then at 80 ℃ for one day for complete curing. The as-obtained film has a dimension of 17 cm length ×8 cm width × 0.1 cm thickness. It is cut into dog bone shape specimens of 7.5 cm length × 0.4 cm width, and four specimens are used for every single tensile test.

To verify the influence from the adding amount of crosslinker, the precursor chains is reacted with TEOS in different reaction ratio ***r*** [equal to n(TEOS)/n(PDMS), in which n(TEOS) and n(PDMS) refers to the mole amount of substance of TEOS and silanol-terminated PDMS]; six series (***r*** = 0.5, 1, 1.5, 2.5, 5, 7.5) were investigated.

Before we discuss the assessment of networks, it is important to recall some definitions of quantities used in mechanics. The origin of the elastomer hyper-elasticity is also briefly discussed and the simplest formula for the retractive force is given.

The engineering stress σ is the ratio of the loading force to the initial sample cross-section (the true stress is the ratio of the loading force to the actual sample cross-section), formula 2.2. The strain ε is the relative length variation (formula 2.3) while

the elongation is the ratio of the actual length by the original one. Extension, stretch-ratio or draw-ratio are synonyms of elongation often found in the literature.

$$\sigma = F/A_0 \tag{2.2}$$

$$\varepsilon = \Delta L/L_0 = (L - L_0)/L_0 \tag{2.3}$$

$$\lambda = L/L_0 = \varepsilon + 1 \tag{2.4}$$

The polymer chains in an elastomeric network are in a molten state and the monomers present a constant thermal agitation. They are thus randomly oriented in absence of applied strain; an applied elongation will impose some preferential orientation which is opposed by the monomer continuous thermal motion: it creates a retractive force. The thermal agitation of monomers increases with temperature and so does the retractive force. The force origin is entropic and does not involve changes in bond angles or bond length. An energetic contribution, generally small, comes from the fact that chain conformations with different energies can be favored by the applied elongation.

The so-called Gaussian theory of hyper-elasticity in its simplest form gives formula 2.5 which is valid for limited elongation. N is the number of active (= cross-linked at both ends) chains, k_B is the Boltzmann constant and T the absolute temperature:

$$\sigma = Nk_BT\left(\lambda - \frac{1}{\lambda^2}\right) \tag{2.5}$$

The multiplying factor Nk_BT is also called the shear modulus G (it appears in pure shear experiments that are specific mechanical tests) and is written (formula 2.8):

$$G = Nk_BT = \frac{\rho RT}{M_c} \tag{2.8}$$

where ρ is the sample density, R the gas constant and M_c the number average chain molecular weight. Elastomer fabricated with different molar ratio $\boldsymbol{r}$ of TEOS vs silanol-terminated PDMS (M_W=18000) are investigated, with r ranging from 1 to 7.5: the tensile test results are shown in **Figure 2.3** (room temperature).

Networks prepared at stoichiometric conditions (r = 0.5) are not shown in the above-given figure, because the as-obtained samples are too sticky. It indicates a low crosslink density that could be due to the volatility of the TEOS cross-linker. A higher amount of cross-linker is required for the alkoxy-functional condensation reaction between silanol-terminated PDMS and TEOS. From the stress-strain plot, it is obvious

that the modulus could be improved when increasing the adding amount of cross-linker. The elongation at break does not display a specific behavior in relation to ***r***.

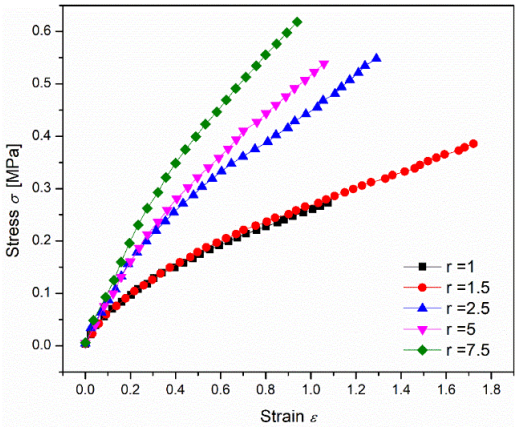

Figure 2.3 Stress vs. strain plot with respect to different reaction ratio ***r***.

As introduced before, the engineering stress is expected to depend linearly upon (λ-1/λ^2) and the slope is related to the average molecular weight between two crosslinks. We see on the plot given in **Figure 2.4** that this relation is rather well-followed. A closer examination reveals some discrepancies that are discussed in **Chapter 3**.

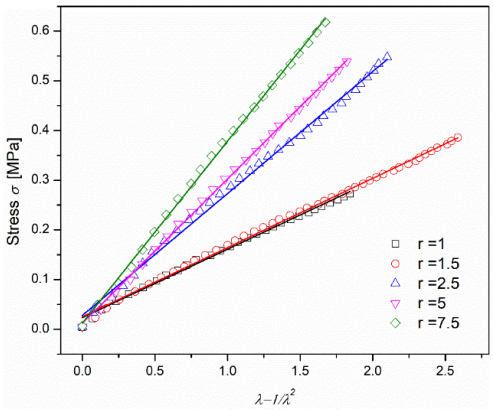

Figure 2.4 Stress vs (λ-1/λ^2) plot with respect to different reaction ratio ***r***.

Table 2.2 Summary of mechanical property in elastomeric networks synthesized from silanol-terminated PDMS (Mw=18000)

sample	w_{sol}	ε_b	σ_b [MPa]	G [MPa]	M_c [g/mol]
$r = 1$	4.041%	1.08	0.2727	0.1377	17.07k
$r = 1.5$	4.226%	1.72	0.3856	0.1392	16.89k
$r = 2.5$	4.195%	1.29	0.5479	0.2454	9.58k
$r = 5$	3.797%	1.06	0.5387	0.2905	8.09k
$r = 7.5$	3.383%	0.94	0.6185	0.3663	6.42k

where w_{sol} is the soluble fraction obtained by swelling experiments, ε_b and σ_b refers to strain and stress at break, G is the elastic modulus and M_c is the average molecular weight.

The resulting data are given in **Table 2.2**. When the reaction ratio exceeds 1.5, the ultimate strength increases but M_c experiences a sudden drop, probably due to the fact that too much cross-linker will produce a heterogeneous network. In these conditions $r = 1$ and $r = 1.5$ can be selected as optimal reaction ratios.

We also checked the influence of precursor chain length and mixtures of different silanol-terminated PDMS precursors (M_W = 18000, 4200) were selected for this purpose. They are denominated Mix000, Mix030, Mix050, Mix070, Mix100, where the number indicates the weight percentage of short chains.

7.58 g silanol-terminated PDMS oil (including long and short precursor chain) are mixed with cross-linking agent TEOS (tetraethyl orthosilicate) in toluene for 30 minutes, with a reaction ratio ***r*** = 1 [equal to n(TEOS)/n(PDMS), in which n(TEOS) and n(PDMS) refers to the mole amount of substance of TEOS and total silanol-terminated PDMS chains]. 0.09 g tin catalyst (stannous-2-ethyl-hexanoate) are then added to the mixture under magnetic stirring for another 5 minutes. The reacting mixture is slowly poured into the round shape Teflon mold and left 30 minutes at room temperature then at 80 ℃ for one day for complete curing. The as-obtained film was cut into dog-bone shape specimens and four specimens are used for mechanical testing.

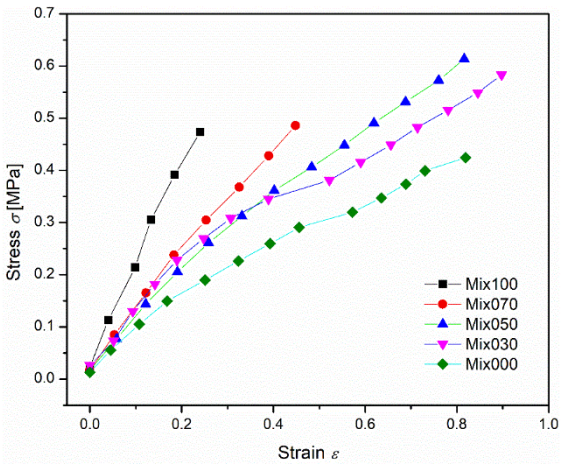

Figure 2.5 Stress vs strain plot of networks synthesized from long/short chains mixing in different weight ratio.

The tensile test results are displayed in **Figure 2.5**: it is expected that the short chains act primarily to increase the ultimate strength due to their limited deformability, while the long chains somehow thwart the spread of rupture nuclei that would otherwise lead to catastrophic failure. On the contrary mechanical properties appeared degraded and these neat PDMS networks synthesized from silanol-terminated PDMS precursor

mixtures (including long and short chains) do not satisfy our final target as they exhibit poor extensibility.

2.4.2 from commercial Sylgard® 184

Commercial Sylgard® 184 from Dow Corning was also tried to make PDMS rubberlike specimen: **Table 2.3** presents the detailed composition of Sylgard® 184.

Table 2.3 Composition of PDMS silicone elastomer kit, Sylgard® 184

	CAS-No.	Concentration (wt%)
Base		
Dimethyl siloxane, dimethylvinyl-terminated	68083-19-2	50–70
Dimethyvinylated and trimethylated silica	68988-89-6	30–50
Tetra(trimethylsiloxy) silane	3555-47-3	1–5
Ethylbenzene	100-41-4	0.1–1
Curing agent		
Dimethyl, methylhydrogen siloxane	68037-59-2	50–70
Dimethyl siloxane, dimethylvinyl-terminated	68083-19-2	20–30
Dimethyvinylated and trimethylated silica	68988-89-6	10–20
Tetramethyl tetravinyl cyclotetrasiloxane	2554-06-5	1–5
Ethylbenzene	100-41-4	0–0.1

11.93 g base part are first dissolved in ethanol, and magnetically stirred for 1 hr., until complete evaporation of ethanol; 1.193 g of curing agent are then added into the mixture under stirring for 10 min; Finally, the mixture is poured into the rectangle or the double tunnel filling mold and let to stay at 60 ℃ for 3 hours in a vacuum oven.

Although the film is easy to peel off from the mold, the elastomer obtained is too tough with poor extensibility and this cannot satisfy our purpose.

2.4.3 from vinyl-terminated PDMS precursor

PDMS elastomers were also synthesized using the hydrosilylation reaction of vinyl-terminated PDMS (MW=28000) with cross-linker poly(methylhydrosiloxane) (PMHS) and a hot catalyst of platinum carbonyl complex (SIP 6829.0, 3–3.5% Pt). The whole chemical reaction is shown below:

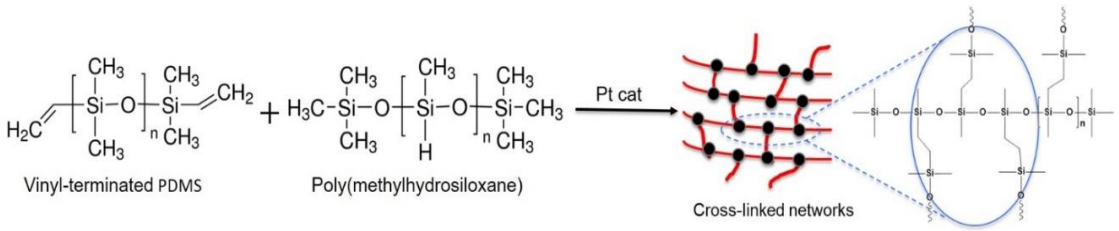

0.4 g methylhydrosiloxane-dimethylsiloxane copolymer (HMS-301, Gelest Inc.) are premixed with 20 ppm catalyst of platinum complex solution (SIP6830.3, Gelest Inc.) in toluene for 30 minutes at room temperature; 10 g vinyl-terminated PDMS (SIS6962.0, Gelest Inc.) are then added under magnetic stirring. The well-stirred mixture was then poured into a Teflon mold and cured at room temperature for 4 hrs. This method failed because the reaction is too rapid ("hot catalyst") and we had no time pouring the mixture into the mold before it cross-links.

After that, a more moderate platinum catalyst (called Speier catalyst) was used to catalyze the crosslinking reaction between the tetrakis(dimethylsiloxy)silane (A4) cross-linker and the precursor chain of vinyl-terminated PDMS oil (M_W=43000). Speier catalyst was prepared as follows: chloroplatinic acid hydrate was quickly weighted by a balance (typically 0.04g) and dissolved into isopropanol to prepare 0.1 mol/L chloroplatinic acid-isopropanol solution. The solution was kept in a fridge prior use.

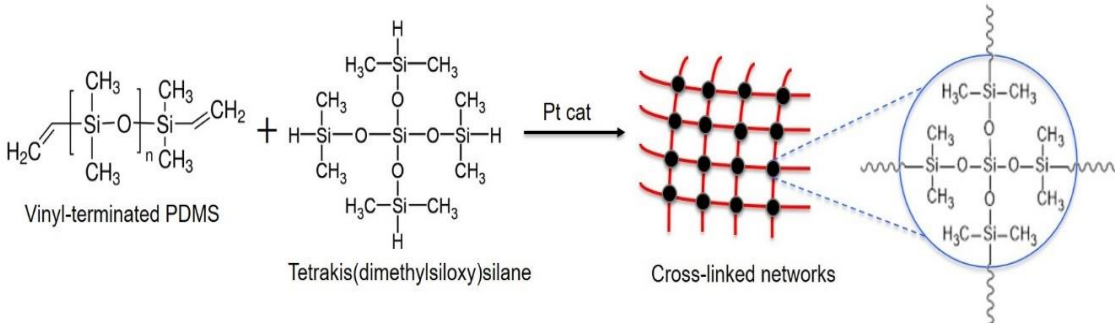

10 g vinyl-terminated PDMS (M_W=43000) oil are then mixed with 0.1261 g cross-linker of tetrakis(dimethylsiloxy)silane in toluene at room temperature for 30 minutes with a mixing ratio ***r*** ca. 1.65 [equal to *n*(tetrafunctional hydrosilane)/*n*(PDMS)]. Afterwards, 19.8 μL chloroplatinic acid-isopropanol solution (the adding amount is 9.8 μL for 5 g of sample mixture) were added under vigorous stirring for another 10 minutes. After degassing in vacuum for 5 minutes, the mixture was poured into the mold and cured at 90 ℃ for 24 hrs.

It must be pointed out that the degassing step should be repeated at least 5 times when fabricating the dumbbell-shape specimen and using the homemade mold with two vertical two filling tunnels. The 0.75 mm thick sheet obtained was carefully released from the mold to avoid scratching the surface, and cut into dumbbell shape specimens 6 mm in width.

The mechanical properties of unfilled PDMS networks prepared from different PDMS precursor chains are compared in **Figure 2.6**. As expected, the modulus

increases with decreasing molecular weight and higher elongation at break is obtained with the higher molecular weight. As for networks prepared from silanol-terminated PDMS, the mechanical properties of the neat networks are not sufficient.

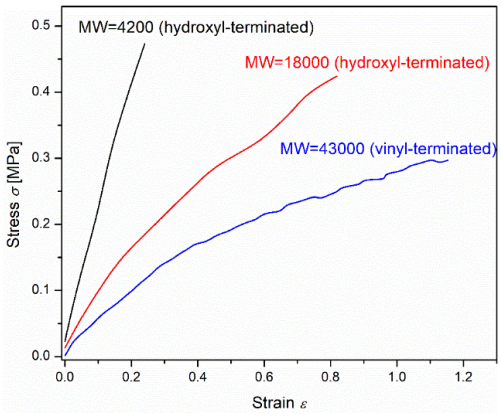

Figure 2.6 Comparison of unfilled PDMS networks from different precursor chains ($r = 1$)

2.5 Preparation of filled PDMS elastomers

Silica powder is normally used to improve the resistance to tear of PDMS networks. However, as stressed above, pristine silica may be difficult to disperse correctly during the mixing process: this is due to the presence of –OH groups at the particle surface that strongly interact with the Si-O-Si moieties. The silica surface can be modified with silanes to reduce hydroxyl content allowing thus improved dispersion. *In-situ* generation of silica into the PDMS matrix by a sol-gel process is also another way to insure perfect mixing. We first present some attempts conducted with another filler, surface modified multi-wall carbon nanotubes (MCNT), as impressive reinforcement effects have been reported in the **Section 2.1**.

2.5.1 PDMS@MCNTs (base: silanol-terminated PDMS)

Commercial multiwall carbon nanotubes MCNTs (NANO® CYLNC7000 series), are produced via a Catalytic Chemical Vapor Deposition (CCVD) process: they have an average diameter of 9.5 nm with an average length of 1.5 μm. All PDMS samples were filled with 0.5 phr MWCNTs following previous publications [36]. The functionalization of the MWCNTs is a two steps process:

(1) synthesis of MWCNTs–COOH: 3g MWCNTs are dispersed into 300 mL of concentrated H_2SO_4/HNO_3 (3:2 v/v) solution at 50 ℃ and stirred for 24 hrs. The solution is filtered, washed with water and acetone. The resulting functionalized MWCNTs (named HO-MCNT) are then dried under vacuum at 100 ℃ for 24 hrs.;

(2) synthesis of MWCNTs–APTES: about 1 g of MWCNTs–COOH is dispersed into 250 mL of ethanol via ultrasonication for 2 hrs. Then the reaction is conducted with 0.1 g APTES (3-aminopropyltriethoxysilane, bought from Sigma-Aldrich) (10.0 wt% of MCNTs) while stirring at 70 ℃ for 4 hrs. After completion of the reaction, the product is purified by repeated washing with water followed by acetone. Finally, the resulting silanized nanotubes (named Si-MCNT) are dried under vacuum at 80 ℃ for 12 hrs.

In terms of fabricating PDMS@MCNT composites, the pristine and functional MCNT were dispersed in propanol separately and sonicated in an ultrasonic bath for 60 min to achieve uniform dispersion. Then, about 7.58 g silanol-terminated PDMS (M_W=18000) oil and 0.179 g TEOS (TEOS: PDMS = 1:2 M ratio) were added into the MCNT suspension and sonicated for another 30 min. This mixture was stirred for about 2 hrs to completely evaporate propanol, followed by addition of the tin catalyst. After degassing, the mixture was poured into the round Teflon mold. The mold was kept in an oven and the mixture was cured at 80 ℃ for 12 hrs. The degassing and curing cycles were applied on the basis of trial and error. Finally, PDMS filled with 0.5 phr pristine MCNT, 0.5 phr HO-MCNT and 0.5 phr Si-MCNT were synthesized.

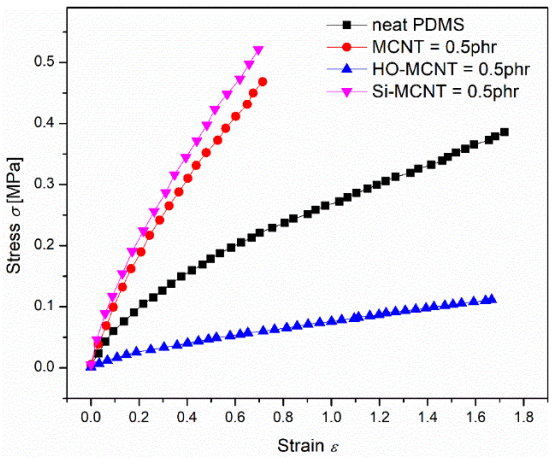

Figure 2.7 stress vs strain plot of PDMS@MCNTs composites by physical mixing.

Due to the different filler loading method, the final composites are synthesized by using different reaction ratio ***r*** [equal to n(TEOS)/n(PDMS)]. For the case of PDMS@MCNTs (showed in **Figure 2.7**), ***r*** was set the value of 2 in order to assure the full crosslinking of the silanol-terminated PDMS. Compared with the neat PDMS elastomer, both MCNT filled and Si-MCNT filled elastomer were showing high

strength but very low elongation at break (see **Figure 2.7**). Although Si-MCNT should have an improved compatibility with the soft matrix, the impact is not obvious compared to unmodified MCNT. The HO-MCNT filled sample shows an opposite behavior and the stiffness is decreased compared to neat PDMS. It may indicate a condensation reaction between the carboxyl groups on the surface of MCNT and the alkoxy groups from cross-linker TEOS, giving rise to partially cross-linked networks.

To conclude, both pristine MCNT and surface modified MCNT are not efficient to improve the mechanical property of PDMS networks and they are ruled out.

2.5.2 PDMS@ sol-gel silica (base: silanol-terminated PDMS)

The *in situ* generation of silica into the unfilled PDMS networks by the sol-gel process first involves swelling by TEOS in the presence of a tin catalyst (dibutyltin dilaurate (DBTDL) at 3 wt%; the catalyst act as Lewis acid to catalyze this reaction). By controlling the swelling time, we can get PDMS composites with different filler loadings. In the present case, we first synthesized elastomeric networks from silanol-terminated PDMS (M_W=18000) with reaction ratio ***r*** of 1.5; the unfilled flat films were then swelled in TEOS/DBTDL solution for 1 min, 5 min, 10 min and 30 min.

Once swollen, the film was put in a sealed glass box containing water at its bottom for 24 hours and maintained at a constant temperature (30 ℃) in an oven. The silica filler is generated inside the PDMS matrix during the exposure to saturated water vapor according to the reaction:

$$Si(OC_2H_5)_4 + 2H_2O \rightarrow SiO_2 + 4C_2H_5OH$$

The films were then vacuum-dried at 80 ℃ for several days to constant weight in order to remove any alcohol generated during the reaction and remaining unreacted TEOS. The final silica content can be computed as

$$SiO_2 \text{ content} = (m_i - m_0)/m_0 \qquad (2.9)$$

where m_i and m_0 is the final weight (after drying) and primary weight of the specimen.

The final silica loading content is influenced by the swelling temperature and swelling time, and by the thickness of the sample. Thus, we cannot repeat perfectly similar silica contents even though all experimental conditions are nearly the same. **Figure 2.8** gives the mechanical results for PDMS@silica composites (***r*** = 1) fabricated with different swelling times. With increasing swelling time, silica loading content can be as high as 56 phr and the sample becomes very rigid and prone to breakage. The

mechanical property turns out to be best for a swelling time of 5 minutes as the toughness is increased without impairing extensibility.

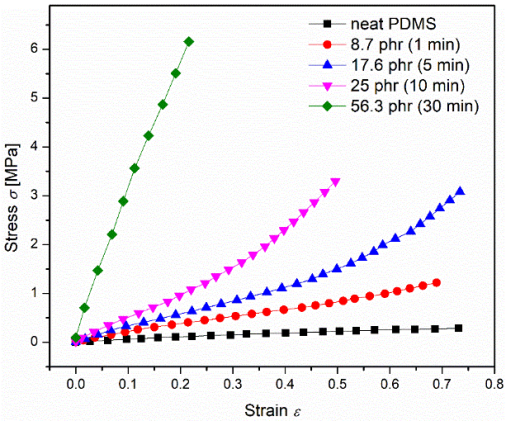

Figure 2.8 stress vs strain plot of PDMS@silica composites by sol-gel method.

To sum up, it appears that PDMS elastomers filled either with surface modified MCNTs or silica via sol-gel process are not satisfying. We decided to turn to nano-particulate silica: vinyl-terminated PDMS oil was used to avoid problems linked to the adsorption of silanol-terminated PDMS oil. However, it was also decided to test in situ sol-gel generation for this type of network.

2.5.3 PDMS@ powder silica (base: vinyl-terminated PDMS)

We first tried to synthesize PDMS@silica composites according to a method proposed by the chemical supplier Gelest. Specifically, 15 wt% hexamethyldisilazane-treated silicon dioxide fillers (SIS6962.0, Gelest Inc.; ultimate particle size = 20 nm; as mentioned above grafting with hexamethyldisilazane modifies the silica surface and promotes dispersion of silica into PDMS) were mixed with vinyl-terminated PDMS oil (DMS-V31, Gelest Inc.; M_W=28000) to produce the so-called DMS-V31S15 mixture. Then, 99.85 wt% DMS-V31S15 mixture and 0.15 wt% platinum carbonyl complex (SIP6831.2, Gelest Inc.) catalyst were mixed to prepare Part A. On the other hand, 90 wt% vinyl-terminated PDMS oil (DMS-V31, Gelest Inc.; M_W=28000) was blended with 10 wt% cross-linker of methylhydrosiloxane-dimethylsiloxane copolymer (HMS-301, Gelest Inc.), to prepare Part B. The curing step proceeds at room temperature for over 4 hrs after mixing 3 parts A to 1 part B. The method did not succeed because the mixture suddenly turned solid into the beaker and could not be casted into films. Hence, this method will be excluded and another milder catalyst will be tried.

Subsequently, vinyl-terminated PDMS (DMS-V33, Gelest Inc.; Mw=43000) oil was selected to prepare the composites. The hexamethylsilazane-treated silicon dioxide filler was first dispersed into toluene by sonication for 30 minutes, followed by addition of 10g of vinyl-terminated PDMS and 0.1261g cross-linker (tetrakis-(dimethylsiloxy)-silane) [the reaction ratio of n(crosslinker)/n(PDMS) is 1.65]. A higher proportion of cross-linker was used to achieve full crosslinking in the composites. The filler content ranges from 5 phr to 40 phr by changing the amount of added silica. After stirring for 30 minutes, about 30 μL catalyst of chloroplatinic acid-isopropanol solution were added and mixed for another 15 minutes. The mixture was degassed and poured into the teflon mold, cured in an oven at 90 ℃ for 12 hrs. The final flat film (17 cm length × 6 cm width × 0.1 cm thickness) was cut into dog bone shape specimens with dimension 50mm × 4 mm for further mechanical tests. Concerning dumbbell samples that are manufactured in a rather closed mold, complete removal of bubbles before the curing step requires at least five vacuum degassing & air venting sequences to obtain good samples (venting is necessary to prevent spill out of the mixture).

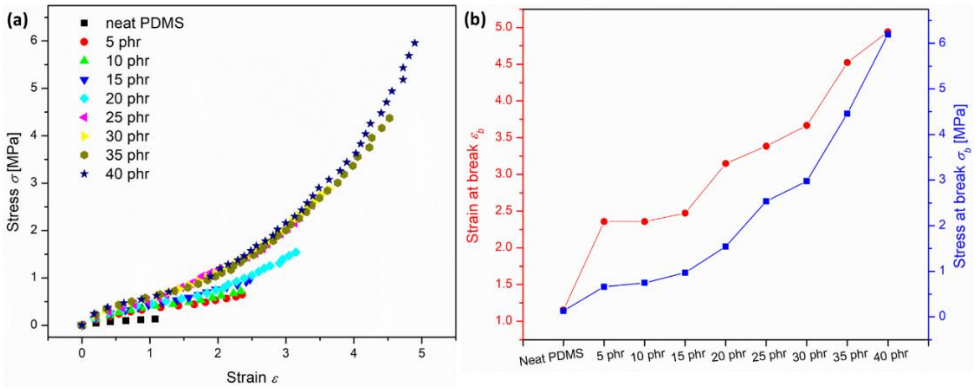

Figure 2.9 (a) stress vs strain plot; (b) stress and strain at break vs filler content plot.

Tensile tests obtained on theses samples are shown in **Figure 2.9**. It is obvious that the silica filler significantly improves the mechanical property of neat PDMS elastomer, both in terms of strength and elongation at break. When the silica content exceeds 20 phr, the elastomer can be stretched to more than 400%, which is sufficient to observe the expected changes in the diffraction patterns.

2.5.4 PDMS@ sol-gel silica (base: vinyl-terminated PDMS)

The *in situ* generation of silica by sol-gel method is the same as for silanol-terminated PDMS networks: six neat PDMS elastomeric films with similar dimensions

(60mm × 60mm; 1mm in thickness) were swollen into 200 mL TEOS in the presence of a 3 wt% tin catalyst of dibutyltin dilaurate; the swelling time for each sample was set to 1 min, 2min, 3min, 5 min, 7min and 10 min respectively. The original mass and the final mass were measured to compute the silica content. Thereafter, the flat film sample was cut into dog bone shape with dimension of 5 mm in length and 4 mm width.

The measured elongations at break did not match those obtained with the modified silica powder and these samples were not initially retained. However, they revealed some surprising features under X-ray diffraction examination and this will be presented in the next chapter.

2.6 Final choice of materials

The results obtained with the different methods are summarized in following table:

Precusor chain	Filler	Advantages/disadvantages
silanol-PDMS (MW=18000, 4200)	surfaced modified MCNT sol-gel silica***	simple and easy synthesis steps easy to remove bubble relatively poor mechanical property
Sylgard® 184	---	super-easy synthesis steps obtained film is tough with relative low elasticity
Vinyl-PDMS (Mw=28000)	powder silica**	simple and easy synthesis steps very quick reaction, unable to cast into film
Vinyl-PDMS (Mw=43000)	powder silica** sol-gel silica***	simple and easy synthesis steps good mechanical properties *difficult to remove bubble

* refers to the fabrication of dumbbell rather than dog-bone shape specimen
** hexamethylsilazane-treated silica (physical mixing)
*** in situ generated silica (sol-gel loading)

In term of elongation at break, the most obvious choice is the combination of vinyl-terminated chains as starting material and modified silica as filler. As mentioned above *in situ* generation of silica into networks obtained from vinyl-terminated chains proved to be very interesting for the study of changes in the diffraction patterns. The following chapter is devoted to a cross-study of these materials by simultaneous tensile tests and X-ray diffraction.

References

[1] Schmidt, D. F., Clément, F., & Giannelis, E. P. (2006). On the Origins of Silicate Dispersion in Polysiloxane/Layered-Silicate Nanocomposites. *Advanced functional materials*, 16(3), 417-425.

[2] Bokobza, L., & Rahmani, M. (2009). Carbon nanotubes: Exceptional reinforcing fillers for silicone rubbers. *KGK. Kautschuk, Gummi, Kunststoffe*, 62(3), 112-117.

[3] Patel, S. K., Malone, S., Cohen, C., Gillmor, J. R., & Colby, R. H. (1992). Elastic modulus and equilibrium swelling of poly (dimethylsiloxane) networks. *Macromolecules*, 25(20), 5241-5251.

[4] Dewimille, L., Bresson, B., & Bokobza, L. (2005). Synthesis, structure and morphology of poly (dimethylsiloxane) networks filled with in situ generated silica particles. *Polymer*, 46(12), 4135-4143.

[5] Takeuchi, H., & Cohen, C. (1999). Reinforcement of poly (dimethylsiloxane) elastomers by chain-end anchoring to clay particles. *Macromolecules*, 32(20), 6792-6799.

[6] Mani, S., Cassagnau, P., Bousmina, M., & Chaumont, P. (2009). Cross-linking control of PDMS rubber at high temperatures using TEMPO nitroxide. *Macromolecules*, 42(21), 8460-8467.

[7] Mani, S., Cassagnau, P., Bousmina, M., & Chaumont, P. (2010). Rheological modelling of the free-radical crosslinking of PDMS rubber in the presence of TEMPO nitroxide. *Polymer*, 51(17), 3918-3925.

[8] Johnston, I. D., McCluskey, D. K., Tan, C. K. L., & Tracey, M. C. (2014). Mechanical characterization of bulk Sylgard 184 for microfluidics and microengineering. *Journal of Micromechanics and Microengineering*, 24(3), 035017.

[9] Hopf, R., Bernardi, L., Menze, J., Zündel, M., Mazza, E., & Ehret, A. E. (2016). Experimental and theoretical analyses of the age-dependent large-strain behavior of Sylgard 184 (10: 1) silicone elastomer. *Journal of the mechanical behavior of biomedical materials*, 60, 425-437.

[10] Park, S., Mondal, K., Treadway III, R. M., Kumar, V., Ma, S., Holbery, J. D., & Dickey, M. D. (2018). Silicones for stretchable and durable soft devices: beyond sylgard-184. *ACS applied materials & interfaces*, 10(13), 11261-11268.

[11] Luo, X., & Mather, P. T. (2009). Preparation and characterization of shape memory elastomeric composites. *Macromolecules*, 42(19), 7251-7253.

[12] Zhang, A., Cheng, L., Hong, S., Yang, C., & Lin, Y. (2015). Preparation of anti-fouling silicone elastomers by covalent immobilization of carboxybetaine. *RSC advances*, 5(107), 88456-88463.

[13] Bhattacharjee, N., Parra-Cabrera, C., Kim, Y. T., Kuo, A. P., & Folch, A. (2018). Desktop-Stereolithography 3D-Printing of a Poly (dimethylsiloxane)-Based Material with Sylgard-184 Properties. *Advanced Materials*, 30(22), 1800001.

[14] Jeong, S. H., Zhang, S., Hjort, K., Hilborn, J., & Wu, Z. (2016). PDMS-based elastomer tuned soft, stretchable, and sticky for epidermal electronics. *Advanced Materials*, 28(28), 5830-5836.

[15] Frounchi, M., Dadbin, S., & Panahinia, F. (2006). Comparison between electron-beam and chemical crosslinking of silicone rubber. *Nuclear Instruments and Methods in Physics Research Section B: Beam Interactions with Materials and Atoms*, 243(2), 354-358.

[16] Bhowmick, A. K., & Vijayabaskar, V. (2006). Electron beam curing of elastomers. *Rubber chemistry and technology*, 79(3), 402-428.

[17] Palsule, A. S., Clarson, S. J., & Widenhouse, C. W. (2008). Gamma irradiation of silicones. *Journal of Inorganic and Organometallic Polymers and Materials*, 18(2), 207-221.

[18] Mashak, A., & Taghizadeh, S. M. (2006). In vitro progesterone release from γ-irradiated cross-linked polydimethylsiloxane. *Radiation Physics and Chemistry*, 75(2), 229-235.

[19] Goswami, K., Skov, A. L., & Daugaard, A. E. (2014). UV-Cured, Platinum-Free, Soft Poly (dimethylsiloxane) Networks. *Chemistry–A European Journal*, 20(30), 9230-9233.

[20] Zuo, Y., Gou, Z., Zhang, C., & Feng, S. (2016). Polysiloxane-Based Autonomic Self-Healing Elastomers Obtained through Dynamic Boronic Ester Bonds Prepared by Thiol–Ene "Click" Chemistry. *Macromolecular rapid communications*, 37(13), 1052-1059.

[21] van den Berg, O., Nguyen, L. T. T., Teixeira, R. F., Goethals, F., Ozdilek, C., Berghmans, S., & Du Prez, F. E. (2014). Low modulus dry silicone-gel materials by photoinduced thiol–ene chemistry. *Macromolecules*, 47(4), 1292-1300.

[22] Müller, U., Kunze, A., Herzig, C., & Weis, J. (1996). Photocrosslinking of silicones. Part 13. photoinduced thiol-ene crosslinking of modified silicones. *Journal of Macromolecular Science, Part A*, 33(4), 439-457.

[23] Ozmen, M. M., Fu, Q., Kim, J., & Qiao, G. G. (2015). A rapid and facile preparation of novel macroporous silicone-based cryogels via photo-induced thiol–ene click chemistry. *Chemical Communications*, 51(98), 17479-17482.

[24] Mongkhontreerat, S., Öberg, K., Erixon, L., Löwenhielm, P., Hult, A., & Malkoch, M. (2013). UV initiated thiol–ene chemistry: a facile and modular synthetic methodology for the construction of functional 3D networks with tunable properties. *Journal of Materials Chemistry A*, 1(44), 13732-13737.

[25] Paul, D. R., & Mark, J. E. (2010). Fillers for polysiloxane ("silicone") elastomers. *Progress in polymer Science*, 35(7), 893-901.

[26] Rajan, G. S., Sur, G. S., Mark, J. E., Schaefer, D. W., & Beaucage, G. (2003). Preparation and characterization of some unusually transparent poly (dimethylsiloxane) nanocomposites. *Journal of Polymer Science Part B: Polymer Physics*, 41(16), 1897-1901.

[27] Sonnier, R., Bokobza, L., & Concha-Lozano, N. (2015). Influence of multiwall carbon nanotube (MWCNT) dispersion on ignition of poly (dimethylsiloxane)–MWCNT composites. *Polymers for Advanced Technologies*, 26(3), 277-286.

[28] Bokobza, L., Bruneel, J. L., & Couzi, M. (2015). Raman spectra of carbon-based materials (from graphite to carbon black) and of some silicone composites. *C—Journal of Carbon Research*, 1(1), 77-94.

[29] Ha, H., Park, J., Ando, S., Kim, C. B., Nagai, K., Freeman, B. D., & Ellison, C. J. (2016). Gas permeation and selectivity of poly (dimethylsiloxane)/graphene oxide composite elastomer membranes. *Journal of Membrane Science*, 518, 131-140.

[30] Burnside, S. D., & Giannelis, E. P. (1995). Synthesis and properties of new poly (dimethylsiloxane) nanocomposites. *Chemistry of materials*, 7(9), 1597-1600.

[31] Osman, M. A., Atallah, A., Müller, M., & Suter, U. W. (2001). Reinforcement of poly (dimethylsiloxane) networks by mica flakes. *Polymer*, 42(15), 6545-6556.

[32] Chen, W., Zeng, X., Li, H., Lai, X., Fang, W., & Zeng, X. (2017). Influence of nonuniform network on mechanical properties of nano-silica reinforced silicone rubber. *Journal of Elastomers & Plastics*, 49(4), 332-344.

[33] Wang, S., Long, C., Wang, X., Li, Q., & Qi, Z. (1998). Synthesis and properties of silicone rubber/organomontmorillonite hybrid nanocomposites. *Journal of Applied Polymer Science*, 69(8), 1557-1561.

[34] Cheng, L., Li, Z., & Zhang, Z. (2011). Poly (dimethylsiloxane)/palygorskite composites: preparation, characterization, and properties. *Polymers for Advanced Technologies*, 22(12), 2596-2601.

[35] Liu, L., Tian, M., Zhang, W., Zhang, L., & Mark, J. E. (2007). Crystallization and morphology study of polyhedral oligomeric silsesquioxane (POSS)/polysiloxane elastomer composites prepared by melt blending. *Polymer*, 48(11), 3201-3212.

[36] Kathi, J., Rhee, K. Y., & Lee, J. H. (2009). Effect of chemical functionalization of multi-walled carbon nanotubes with 3-aminopropyltriethoxysilane on mechanical and morphological properties of epoxy nanocomposites. *Composites Part A: Applied Science and Manufacturing*, 40(6-7), 800-809.

[37] Bokobza L. (2007) Multiwall carbon nanotube elastomeric composites: A review. *Polymer*, 48 (17): 4907-4920.

Chapter 3

Tensile Tests of PDMS@SiO_2 Elastomers at Room Temperature

Contents

3.1 Introduction

As underlined in **Chapter 1**, the most important specification for our samples is the elongation at break (λ_{break}): it must be high enough to permit the observation of the passage from the lower elongation ($\lambda < 2$) to the higher elongation ($\lambda > 4–5$) crystalline diffraction patterns at low-temperature and values in excess of 5 are thus typically targeted. Ultimate extensions up to 9 are reported in the literature for silica-filled PDMS and our goal seems modest, but it is in relation with the simplicity of means we have for the material synthesis.

We present here the mechanical tests at room temperature that have been conducted on the most promising materials. Moreover, the tensile test machine also allows to simultaneously record X-ray diffraction patterns and we thought it senseless not to use this additional information. It will be shown that it actually proved useful and the last section of this chapter concentrates on this point.

3.2 Technical section

3.2.1 The tensile WAXS machine

The tensile WAXS machine shown in **Figure 3.1-A** is mounted on a rotating anode X-ray generator (Rigaku RU200BEH; focus size: 0.2 × 0.2 mm^2; operated at 40 kV, 40 mA) and the K_α radiation of the copper anode is selected by a doubly-curved graphite monochromator ($\lambda = 0.1542$ nm; source-to-optics distance = optics-to-sample distance = 24 cm). This type of optics delivers a very intense beam but with a limited resolution (typically $\delta q_{1/2} \approx 0.15\ nm^{-1}$).

The sample is located at the focalization point close to the collimator exit (see **Figure 3.1-B**): the beam impact on the sample is a circle ca. 1mm in diameter and the delivered intensity is of the order of 10^9 photons/s. Diffraction patterns were recorded with a hybrid-pixel X-ray camera (Pilatus 200K) that combines high dynamic, sensitivity and absence of noise. Exposure time were set at 10s and the transfer time from the camera to the computer is ca. 0.3s. The beam-stop is fixed on the detector and contains a photodiode to monitor the intensity transmitted through the sample: this information is necessary for a proper correction of the air scattering contribution. The sample is stretched symmetrically at a selectable speed (1 to 800 mm/ min) and the force sensor is located on one of the holding stages (Sensy miniature force sensor 5932 series, 30daN max.). Punctured vertical stainless pipes can blow thermalized air onto

the sample but this option is presently not used as all experiments were conducted at room temperature. The same remark applies to the infrared sensor that measures the surface temperature of the sample. An optical camera takes a magnified image of the sample simultaneously with the X-ray pattern acquisition: the analysis of these images is our only way to extract precise draw ratios (see below).

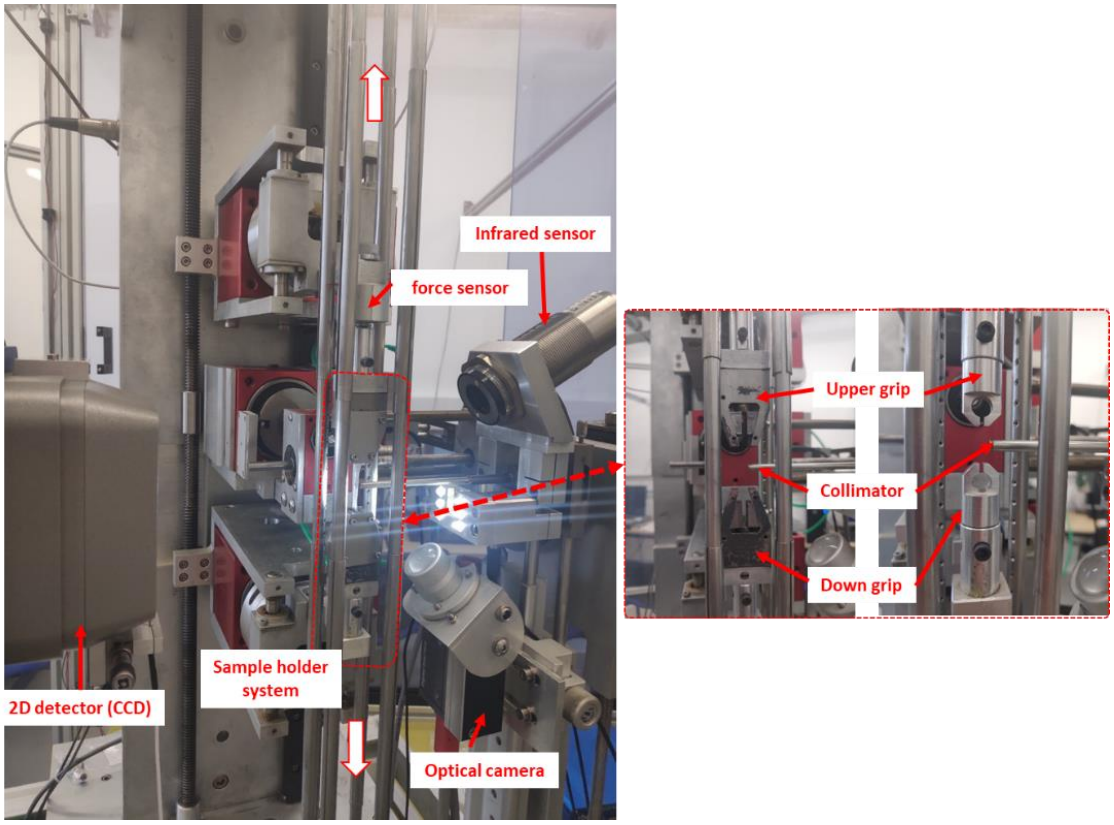

-A- -B-

Figure 3.1 The tensile test machine.

As mentioned in **Chapter 2**, two types of tensile specimens have been made and their dimensions are summarized in **Figure 3.2**. Dog-bone shape samples are most often used for elastomer mechanical testing. Samples may be difficult to hold when the retractive force becomes important and we have developed the small pneumatic assisted grips presented in **Figure 3.1-A** (left) to minimize this problem. Indeed, PDMS elastomers are rather soft and no tendency to slippage was observed. Dumbbell shape samples are less prone to slippage and the grips can be made quite small (**Figure 3.1-B**, right). In all cases the sample thickness was limited to ca. 0.6mm to reduce X-ray absorption and optimize the amount of diffracted intensity. As mentioned in **Chapter 2**, PDMS@SiO_2 mixtures become quite viscous at higher SiO_2 content and this led to

difficulties for homogeneously fill the dumbbell mold with such a narrow gap between the two opposite mold plates (see **Figure 2.2** in **Chapter 2**).

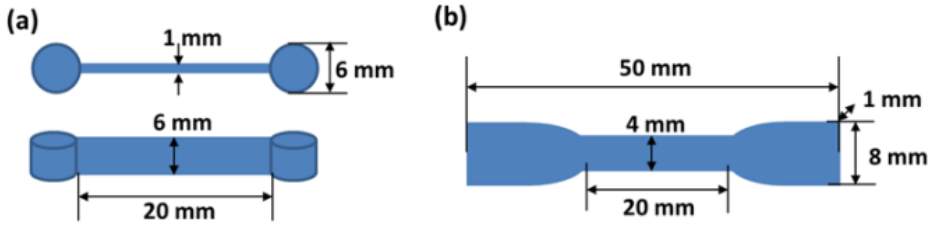

Figure 3.2 Dimension of tested specimen: (a) dumbbell shape and (b) dog-bone shape.

3.2.2 Evaluation of the draw ratio

Nowadays the precise determination of the strain field experienced by an elastomeric specimen is based on digital image correlation techniques [1] . Paint is generally sprayed on the sample to produce a speckle pattern whose evolution is followed image after image by the appropriate software (see **Figure 3.3-A**). Such softwares are expensive, the technique requires very uniform lightening conditions and the adequate paint spraying is not always easy to obtain. For these reasons, we preferred to use two simple but highly time-consuming techniques based on a visual inspection of images. It is first possible to follow how added marks progressively separate in the stretching direction: this is illustrated in **Figure 3.3-B**. One problem is that added marks quite often get out of the image field and alternative marks have to be found (for instance dust points or local visible irregularities).

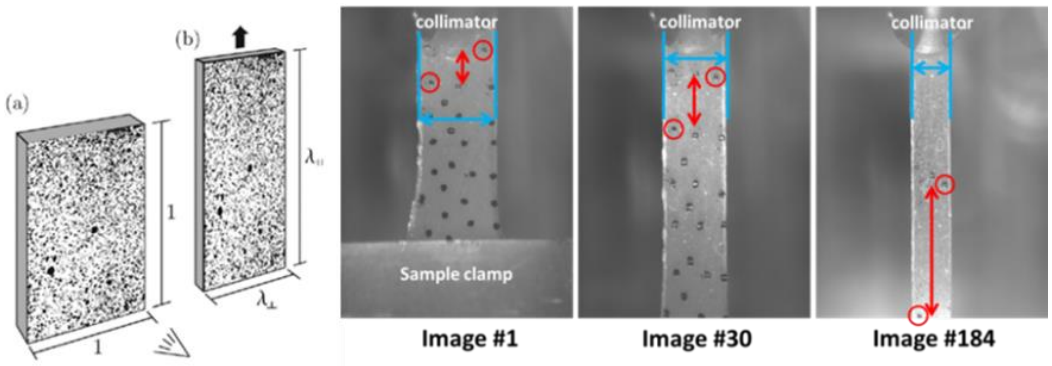

-A- **-B-**

Figure 3.3 -A- illustration of the digital image correlation technique (after [3]) **-B-** illustration of the two techniques used for the evaluation of the draw ratio (red: direct measurement along the stretching axis, blue: indirect measurement from the sample width). Silica powder filled sample of 18phr.

The second technique relies on the measurement of the sample width: it varies as $1/\sqrt{\lambda}$ where λ is the draw ratio with the hypothesis of an uncompressible material

(PDMS Poisson ratio: 0.500 ± 0.03 [3]). It is to notice that the software of the machine automatically measures the sample width, but changing lightening conditions may induce errors and we preferred to do it manually. This method is less precise than the first one at higher stretches.

We see in **Figure 3.4** that draw ratios obtained by the two techniques compare well. Averages between these two types of measurements are systematically used in what follows.

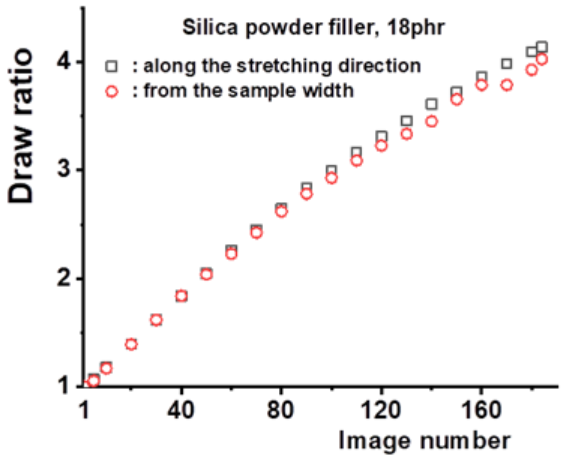

Figure 3.4 Comparison of draw ratio obtained with the two techniques (see text)

3.2.3 Stress-strain curves

In the present case, all samples have been submitted to a single pull test till breakage without any prior accommodation (ie. stress softening induced by repeated stretching). It means that stress-strain curves presented below are not equilibrium ones as regard to stress levels.

3.2.3.1 Unfilled samples

Six dog-bone samples of the same batch (vinyl terminated oil, M_w=48000; see **Chapter 2**) were tested at an extension speed of 10 mm mn^{-1}: we see in **Figure 3.5** that the different curves are close and the average elongation at break is ca. 2.3 in agreement with what is reported in the literature for unfilled PDMS elastomers[4]. As will be confirmed below, we remain in the Gaussian regime of the low elongations and data can be adjusted with the Mooney-Rivlin formula:

$$\sigma = (2C_1 + 2C_2/\lambda)(\lambda - 1/\lambda^2) \qquad (3.1)$$

It is recalled that the term $2C_1$ is generally identified with the shear modulus G for the ideal chain network (see **Chapter 2**) and the added correction $2C_2$ is attributed to the additional topological constraints exerted by the surrounding chains on a given polymer chain. We presently obtained $2C_1 = 0.1012$ and $2C_2 = 0.1342$ and the fact that $C_1 \sim C_2$ is often observed in various elastomers [5].

Identifying $2C_1$ with $G = \rho RT/M_w$ one obtains $M_w \approx 23236\ g/mol$, far from the expected value, 48000g/mole. This can be explained by the fact that one is well-above the entanglement molecular weight $M_e \approx 10000 g/mol$ [6]. Indeed the shear modulus at $\lambda = 1$ is $2C_1 + 2C_2$ that actually yields $M_w \approx M_e$. Entanglement free PDMS elastomers can be obtained using modified PDMS chains [7].

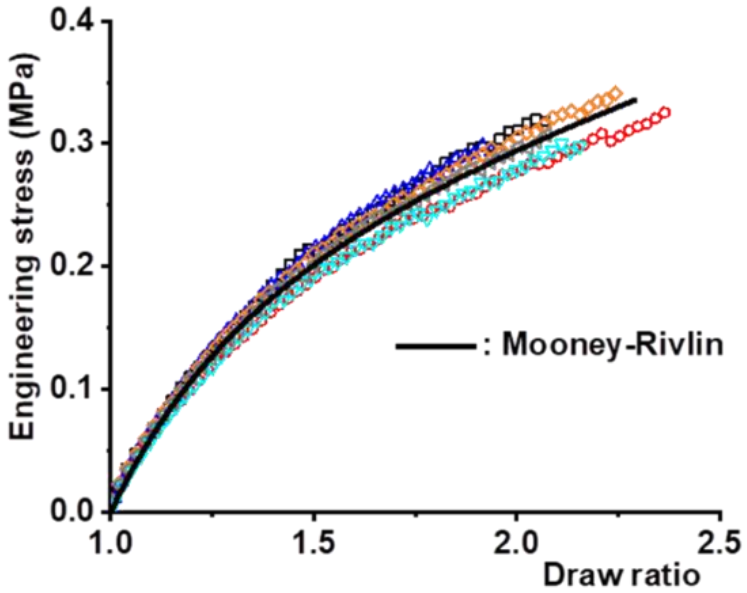

Figure 3.5 Stress-strain curves for unfilled PDMS material (material basis: vinyl-terminated oil M_W=48000g/mol).

3.2.3.2 Silica powder filled samples

Stress-strain curves and elongation at break are displayed in **Figure 3.6**: each curve corresponds to an average over a minimum of two test samples. As expected, the stress level increases in average with the silica content at a given draw ratio and some inconsistencies (for instance 40 phr curve) may due to the reduced number of test samples. The elongation at break exceeds our original goal $\lambda_{break} = 5$ for a silica content equal or in excess of 25 phr.

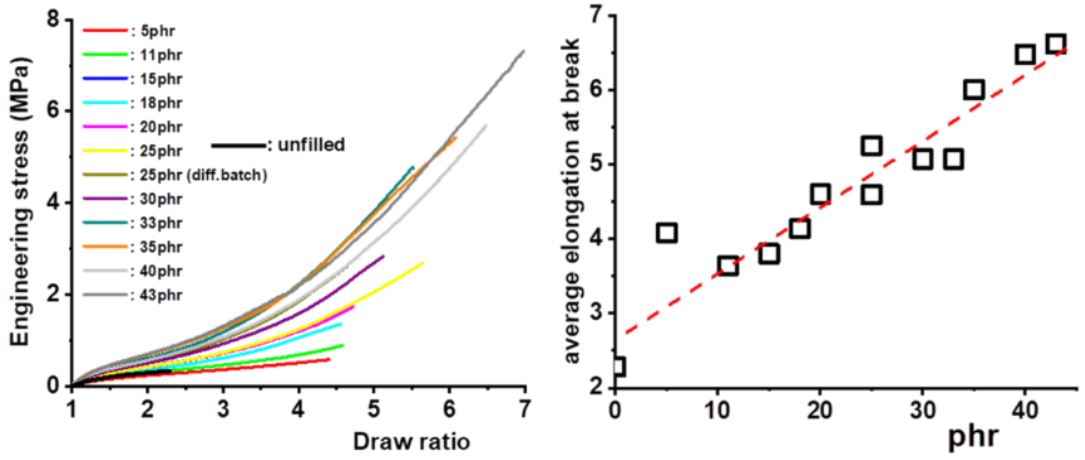

-A- **-B-**

Figure 3.6 -A- Stress-strain curves for the silica powder filled samples; each data set corresponds to a single specimen. **-B-** Elongation at break vs. silica content

3.2.3.3 Sol-gel silica filled samples

Unfilled elastomers similar to the ones presented above are first swollen with different contents of TEOS and put in a water vapor saturated atmosphere to induce silica condensation (see **Chapter 2**). We see in **Figure 3.7-A** that an important reinforcement is induced even for low silica contents: stress levels similar to those measured in silica powder filled samples are reached at significantly lower strain levels. This agrees with previous reports that silica produced by the sol-gel process is highly efficient for reinforcement [8]. However, λ_{break} (see **Figure 3.7-B**) is only moderately improved compared to unfilled networks and remains far from our target. We show in what follows that these sol-gel filled samples should not be rejected and that they can prove interesting for some experiments.

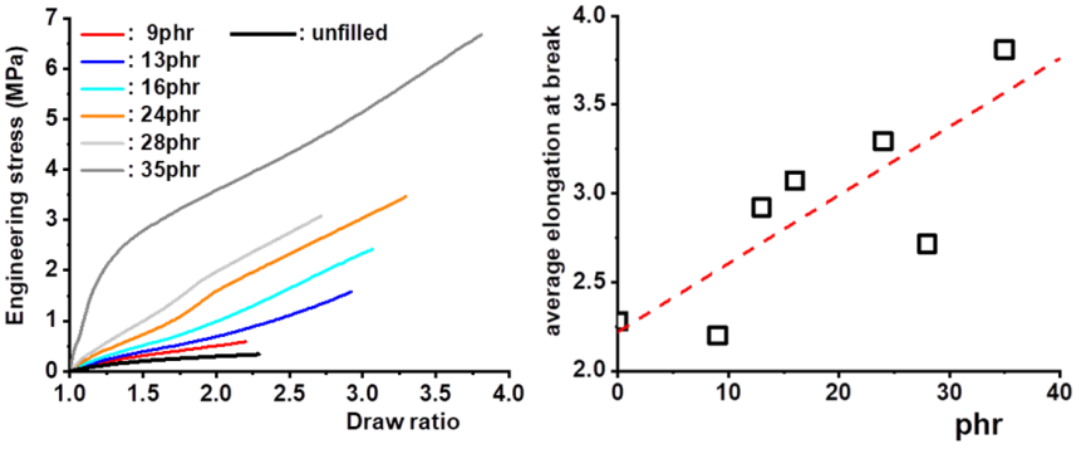

-A- **-B-**

Figure 3.7 -A- Stress-strain curves for the sol-gel filled samples; each data set corresponds to a single specimen. **-B-** Elongation at break vs. silica content.

3.2.3.4 The strain-amplification factor

We see that the addition of a silica filler results in an increase of the stress. For moderate filler content the stress increase is generally well accounted for by the Guth and Gold formula

$$\sigma_{filled}(\varphi,\varepsilon) \approx \left(1 + 2.5\varphi + O(\varphi^2)\right)\sigma_{unfilled}(\varepsilon) \tag{3.2}$$

where $\varepsilon = \lambda - 1$ is the applied strain and φ the volume fraction of filler [9]. According to T Inoue *et al.*[10], this formula can be rewritten

$$\sigma_{filled}(\varphi,\varepsilon) = a_\varepsilon(\varphi)a_\sigma(\varphi)\sigma_{unfilled}(\varepsilon) \tag{3.3}$$

where $a_\varepsilon(\varphi) = 1/(1-\varphi)$, $a_\varepsilon(\varphi)$ is the strain amplification factor which is the ratio between the strain experienced by the soft matrix to the applied strain. It originates from the fact that silica particles are rigid and cannot deform which results in an enhanced deformation of the soft fraction [11]. Based upon geometric consideration it is evaluated to be $1/(1-\varphi)$. The second term $a_\sigma(\varphi) \approx 1 + 1.5\varphi$ is the stress amplification factor and it comes from the fact that the free flow of chains during extension is hindered by the presence of the rigid filler particles.

We will now show how X-ray diffraction may give an access to the strain amplification factor $a_\epsilon(\varphi)$: the results will be compared with the theoretical prediction $a_\varepsilon(\varphi) = 1/(1-\varphi)$ for the two filling procedures.

3.3 Diffraction by amorphous PDMS

3.3.1 Quiescent state

At room temperature, polymeric chains within the PDMS network are molten and randomly oriented: the associated reciprocal space thus possesses spherical symmetry which means it consists in concentric spheres whose intensity $I(\vec{q})$ only depends upon $q = |\vec{q}|$. The scattering geometry of the tensile machine is depicted in **Figure 3.8** and we see that the intersection of a given reciprocal sphere with the Ewald sphere of reflection is a circle that results in an intensity ring on the X-ray camera.

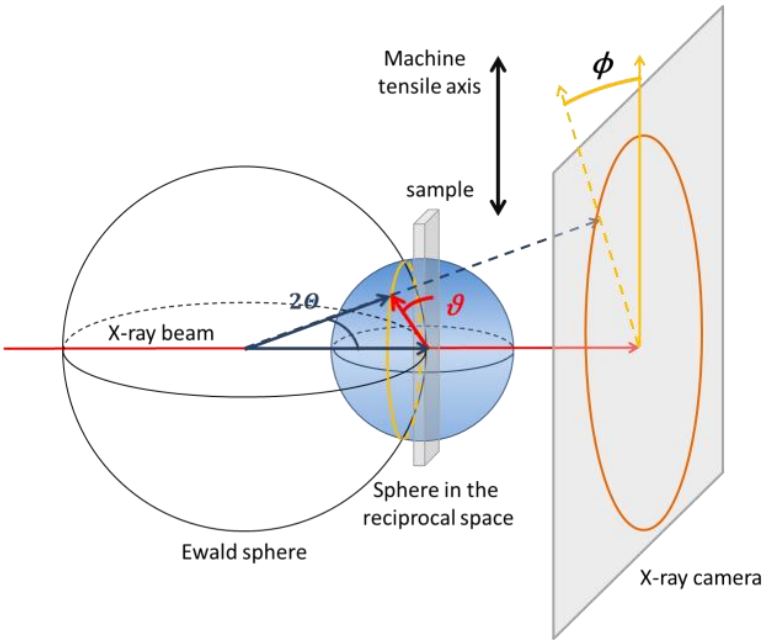

Figure 3.8 Scattering geometry for the tensile test machine

An example of such a pattern is given in **Figure 3.9-A** and the associated radial scan is displayed in **Figure 3.9-B** (in a radial scan, the plotted intensity is averaged on circles of increasing radii). It can be stressed that diffraction patterns of a PDMS rubber in the quiescent state or of a PDMS oil are similar as the concentration in cross-links is in any case too weak to induce any detectable change. We observe a rather intense and broad ring at smaller diffraction angles often called "amorphous halo" in the literature that is succeeded by weaker rings better seen on the radial scan. This succession of broad rings is typical for short-range order as only distances beween nearest neighbor atoms or moities are well-defined. If d is such a distance, a broad peak can be observed at a scattering vector of modulus q that approximately satisfies the relation $q \cdot d \approx 2\pi$.

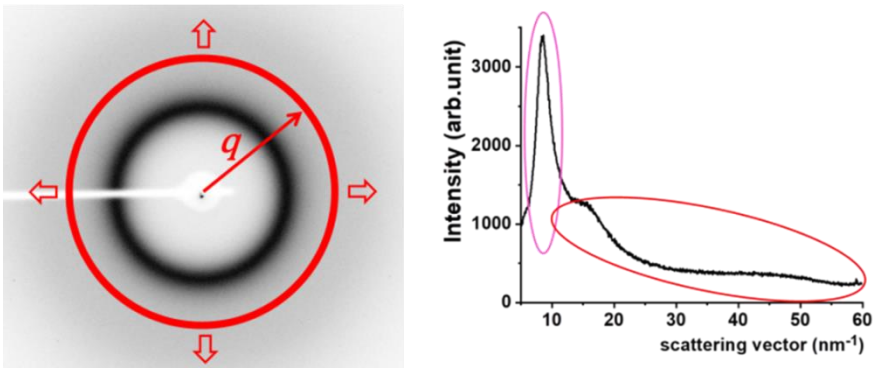

-A- **-B-**

Figure 3.9 -A- Representative diffraction pattern for a PDMS oil in the scattering geometry depicted in **Figure 3.8**. -B- Associated radial scan.

The inner intense broad peak is centered at $q \approx 8.45\ nm^{-1}$ and X-rays are not sensitive to atomic details for such a value of the scattering vector ($q \cdot a \ll 2\pi$ for inter-atomic distances a~$0.15\ nm$): each chain appears more or less like a tube of uniform density (see **Figure 3.10**) and the distance $d = 2\pi/q = 0.74\ nm$ gives an order of magnitude for the distance between these tubes, ie. between adjacent polymer chains. The main peak is thus mainly associated to **inter-chain correlations** while weaker peaks at larger scattering vectors in **Figure 3.9** mainly correspond to smaller distances, ie. **intra-chain correlations** (distances *a* in **Figure 3.10**). Of course the reality is more complex than that.

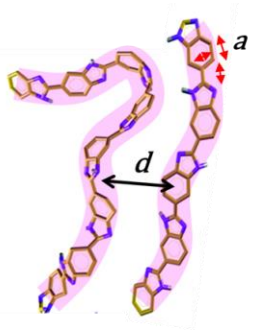

Figure 3.10 Schematization of distances observed by X-ray diffractionin a polymer melt

3.3.2 Effect of stretching

Stretching results in a preferential orientation of polymer chains along the stretching axis. This can quantified by the definition of a **segmental orientation function** $w(\vartheta, \varphi)$ such that the probability that the orientation of a segment lies within the solid angle $d\Omega$ (see **Figure 3.11**) is given by $dP(\vartheta, \varphi) = w(\vartheta, \varphi)d\Omega$. The distribution is uniform in the quiescent state ($w(\vartheta, \varphi) = 1/4\pi$) and becomes progressively centered at the poles under stretching.

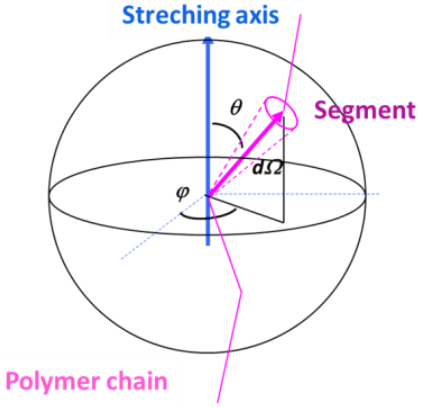

Figure 3.11 The definition of the segmental orientation function $w(\vartheta, \varphi)$

A spherical function can be developped on spherical harmonics $Y_l^m(\vartheta,\varphi)$ and this holds for the segmental orientation function:

$$w(\vartheta,\varphi)=\sum_{l=0}^{\infty}\sum_{m=-l}^{l}a_{l,m}Y_l^m(\vartheta,\varphi) \tag{3.4}$$

where $a_{l,m}=\int_0^{2\pi}d\varphi\int_0^{\pi}\sin\vartheta d\vartheta Y_l^{*m}(\vartheta,\varphi)f(\vartheta,\varphi)$. Simple stretch will impose uniaxial symmetry and the function does not depend upon φ: the coefficients $a_{l,m}$ are all equal to zero except for m = 0:

$$w(\vartheta)=\sum_l a_l Y_l^0(\vartheta)=\sum_l a_l\sqrt{\frac{2l+1}{4\pi}}P_l(\cos\vartheta) \tag{3.5}$$

where $P_l(\cos\vartheta)$ are Legendre polynomials. $w(\vartheta)$ is an even function of ϑ and its expansion can only contain even Legendre polynomials and we can write more conveniently:

$$w(\vartheta)=\sum_l\frac{4l+1}{2}\langle P_{2l}\rangle P_{2l}(\cos\vartheta) \tag{3.6}$$

where $\langle P_{2l}\rangle=\int_0^{\pi}\sin\vartheta\,d\vartheta\,P_{2l}(\cos\vartheta)w(\vartheta)$. In the Gaussian regime of low stretches and in the frame of the classical theory of elasticity [12], the coefficients $\langle P_{2l}\rangle$ are negligible for $l>1$ and

$$\langle P_2\rangle=\frac{1}{5N}\left(\lambda^2-\frac{1}{\lambda}\right)+O\left(\frac{\lambda^4}{N^2}\right) \tag{3.7}$$

One can notice that $\langle P_2\rangle\sim\sigma_t$ where σ_t is the true stress (related to the engineering stress σ by $\sigma_t=\lambda\sigma$ for incompressible materials). In real networks, a segment will be not only sensitive to the orientation imposed by the chain extremities but also to the orientational field exerted by the surrounding segments: the above-given formula for $\langle P_2\rangle$ is normally no more valid. However, the proportionality relation between σ_t and $\langle P_2\rangle$ generally holds for real elatomeric networks and this is the stress-optical law [13].

We saw previously that the reciprocal space for an unextended sample consists of concentric spheres characterized by their intensity $I(q)$. Simple stretch imposes uniaxial symmetry and the intensity $I(\vec{q})$ will now depend not only on the modulus $q=|\vec{q}|$ but also on the angle ϑ beween the stretching axis and $\vec{q}$:

$$I(q,\vartheta)=I_0\sum_l\frac{4l+1}{2}\langle P_{2l}^{RX}(q)\rangle P_2(\cos\vartheta) \tag{3.8}$$

It has been demonstrated that $\langle P_{2l}^{RX}(q)\rangle$ is proportional to $\langle P_{2l}\rangle$ at scattering vectors $\vec{q}$ that are only associated to **intra-chain correlations** [14] . GR Mitchell admits this to still hold at scattering vectors $\vec{q}$ associated to **inter-chain correlations** and in particular to the "amorphous halo" [15] . There is no demonstration of this point to our knowledge. GR Mitchell proposes to estimate the proportionality factor between $\langle P_2^{RX}\rangle$ and $\langle P_2\rangle$ based on geometrical considerations but he unfortunatly does not give details. At our level, the interest of measuring the coefficients $\langle P_{2l}^{RX}\rangle$ is twofold:

(1) In the gaussian regime of low stretches, only the coefficient $\langle P_2^{RX}\rangle$ is significant. It can be used to evaluate **the strain amplification factor** $a_\varepsilon(\varphi)$ in filled PDMS as follows [16] . Let us suppose that we know the draw-ratio dependence of $\langle P_2^{RX}\rangle_{unfilled}(\lambda)$ for the unfilled material and $\langle P_2^{RX}\rangle_{filled}(\lambda)$ for a filled material. The effective draw-ratio λ_{eff} experienced by the PDMS gum in the filled material is given by the equation that allows to link λ_{eff} and λ :

$$\langle \boldsymbol{P_2^{RX}}\rangle_{\boldsymbol{unfilled}}(\boldsymbol{\lambda_{eff}}) = \langle \boldsymbol{P_2^{RX}}\rangle_{\boldsymbol{filled}}(\boldsymbol{\lambda}) \qquad (\mathbf{3.9})$$

(2) The apparition of higher order $\langle P_{2l}^{RX}\rangle$ coefficients is a signal that the sample is out of the gaussian regime. For a chain of *N* statistical segments, this normally happens when the draw ratio is no more negigible compared to the maximum theoretical extension $\sqrt{N}$.

3.3.3 Measurement of the coefficients $\langle \boldsymbol{P_{2l}^{RX}}\rangle$

3.3.3.1 The diffraction geometry

The diffraction geometry for the tensile apparatus has been given in **Figure 3.8**. In order to determine the coefficients $\langle P_{2l}^{RX}(q)\rangle$ at a given *q*-vector modulus, it is necessary to measure the scattered intensity from the equator to the north pole as schematized in **Figure 3.12-A**. This is called an azimuthal scan and it is performed by giving the sample axis a kind of precession movement as schematized in **Figure 3.12-B**. An example of such a measurement is given by study by GR Mitchell [15] . This complicated movement is impossible to perform with our stretching apparatus that only allows the static geometry depicted in **Figure 3.8** and **3.12-C**.

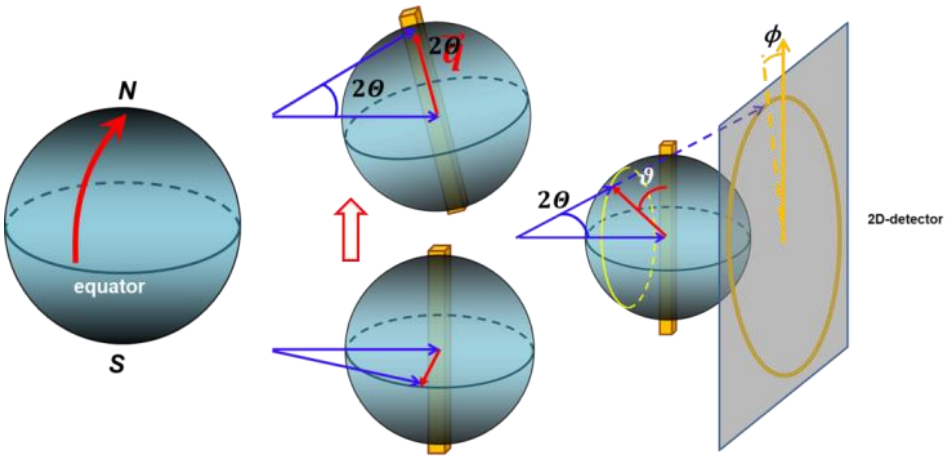

-A- **-B-** **-C-**

Figure 3.12 -A- An azimuthal scan, -B- how to perform an azimuthal scan, -C- the actual scattering geometry

In this case, only scans corresponding to the yellow circle are measured. One can apply the correction $\cos\vartheta = \cos\Theta\cos\phi$ to transform these scans into azimuthal scans. In the case of the amorphous halo of PDMS (see **Figure 9**), $\Theta \approx 6°$ for the K_α radiation of copper and $\cos\Theta \approx 0.994$: no correction is necessary and we can write:

$$I(q,\phi) \approx I_0 \sum_l \frac{4l+1}{2} \langle P_{2l}^{RX}(q) \rangle P_{2l}(\cos\phi) \qquad (3.10)$$

3.3.3.2 Correction for air and silica scattering

Air and silica scatterings bring a non negligible contribution to the recorded intensity and it has to be properly removed. Air scattering is measured in absence of sample and the associated ϕ-scan is flat: $I_{air}(\varphi) = I_{air}^0$. As mentioned above the intensity transmitted through the sample is continuously measured by a diode located into the beam-stop. We call I_0^{air} the intensity measured without sample and $I_{trans}^{air}(\lambda)$ the intensity transmitted through the sample for a draw ratio λ: the correction is simply $I_{air}^0 . \left(I_{trans}^{air}(\lambda)/I_0^{air}\right)$. The contribution of silica is different in that it contributes to the intensity scattered by the sample in a constant proportion. Silica particles are isotropic scatterers and the associated scattering does not depend upon ϕ: it has to be removed from the only zeroth order term $I_0\langle P_0^{RX}\rangle$.

We show in **Figure 3.13** that the scattered intensity for a silica-filled sample can be successfully accounted for as the sum of the scattering by an unfilled PDMS network and by the silica particles (sol-gel particles are assumed to scatter in a similar way to

amorphous silica powder). These measurements are conducted on unstretched samples for the sake of simplicity. The silica correction is computed within the interval given by the two vertical dotted black lines that correspond to the inner and outer limits of the ϕ-scans used below.

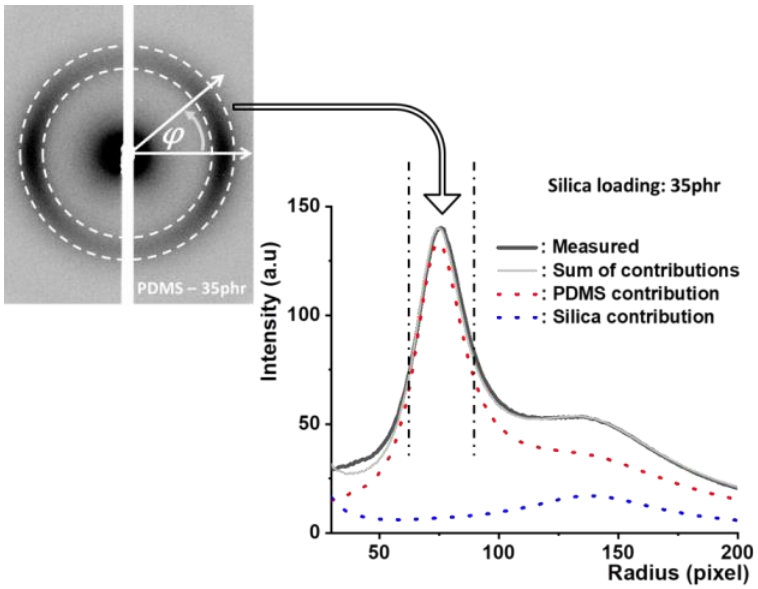

Figure 3.13 Evaluation of the silica contribution to the background. All radial scans have been previously corrected for air scattering. Vertical dotted black lines correspond to the inner and outer limits of the ϕ-scan.

We have plotted in **Figure 3.14** the ratio of the PDMS gum contribution to the total intensity for measurements performed at different silica contents. We observe an almost linear dependence and the zero[th] order contribution to the ϕ-scan intensity needs to be simply multiplied by the approximate factor $0.996 - 0.00182 * phr$ (black line in **Figure 3.14**); this correction remains actually limited.

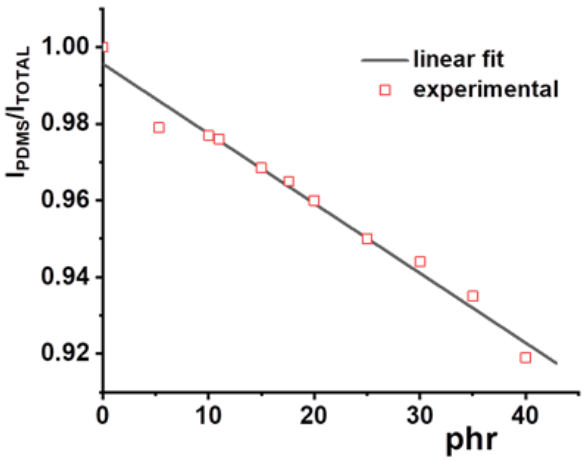

Figure 3.14 Correction for the silica contribution.

3.4 Results

3.4.1 Neat PDMS samples

We display in **Figure 3.15** the dependence of the Legendre coefficients upon elongation for six unfilled samples of the same batch. We see that $\langle P_4^{RX} \rangle_{unfilled}$ remains negligible which means that we stay in the Gaussian regime. Black heavy lines (labelled as "guide for the eye") are data averages. $\langle P_2^{RX} \rangle_{unfilled}$ is conveniently adjusted by a second-order polynomial relation of $\langle P_2^{RX} \rangle_{unfilled} \approx 0.02226 - 0.0189\lambda - 0.00295\lambda^2$.

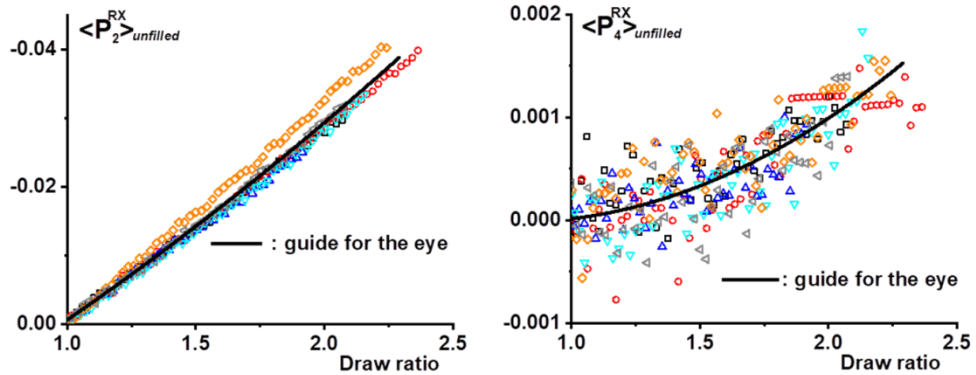

-A- -B-

Figure 3.15 Legendre coefficients $\langle P_2^{RX} \rangle$ and $\langle P_4^{RX} \rangle$ for the unfilled samples. The guide for the eye corresponds to the estimated average behavior.

As mentioned above, GR Mitchell did not present his methodology to estimate the proportionality factor that relates $\langle P_2^{RX} \rangle$ to $\langle P_2 \rangle$: it thus not possible to make a comparison with the prediction of the classical theory given by **Equation 3.7**[12]. We show in **Figure 3.16** that $\langle P_2^{RX} \rangle_{unfilled}$ and the true stress approximately follow a similar dependence upon elongation, which is in agreement with the stress optical law.

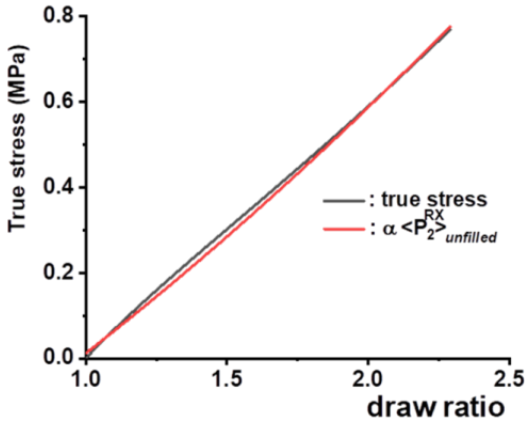

Figure 3.16 Comparison of true stress and $\langle P_2^{RX} \rangle_{unfilled}$ strain behavior

3.4.2 The strain amplification factor in the low-strain region

From the tensile WAXS analysis of neat PDMS network, we now know that :

$$\langle P_2^{RX}\rangle_{unfilled}(\lambda_{eff}) \approx 0.02226 - 0.0189\lambda_{eff} - 0.00295{\lambda_{eff}}^2 \quad (3.11)$$

In what follows, $\langle P_2^{RX}\rangle_{filled}(\lambda)$ will be evaluated in the region of low strains where higher order coefficients $\langle P_{2l}^{RX}\rangle$ are negligible and the strain amplification factor will be evaluated using formula **3.9**. It will be compared to the expression $a_\varepsilon(\varphi) = (\lambda_{eff} - 1)/(\lambda - 1) = 1/(1-\varphi)$ equivalently written

$$\lambda_{eff} = (\lambda - 1)a_\varepsilon(\varphi) + 1 = (\lambda - \varphi)/(1-\varphi) \quad (3.12)$$

where the silica volume fraction φ can be obtained from the *phr* content according to

$$\varphi = \frac{(phr/\rho_{SiO_2})}{(phr/\rho_{SiO_2} + 100/\rho_{PDMS})} \approx \frac{0.44phr}{(100 + 0.44phr)} \quad (3.13)$$

where ρ_{SiO_2} and ρ_{PDMS} are respectively the density of silica filler (ca. 2.2 g/cm^3) and PDMS oil (0.965 g/cm^3).

3.4.2.1 Powder silica filler

We used the above-mentioned **Equation 3.9** to plot the effective elongation vs. applied elongation for a representative example (see **Figure 3.17**; 30 phr powder silica filled PDMS). We see that the agreement with the expected behavior $\lambda_{eff} = (\lambda - \varphi)/(1-\varphi)$ is only approximate. The experimental strain amplification factor is simply obtained by a linear adjustment of the curve in **Figure 3.17**. All experimental strain amplification coefficients for the different silica content have been similarly obtained; they are listed in **Table 3.1** and an overall satisfying agreement between experimental and calculated strain amplification factors is observed.

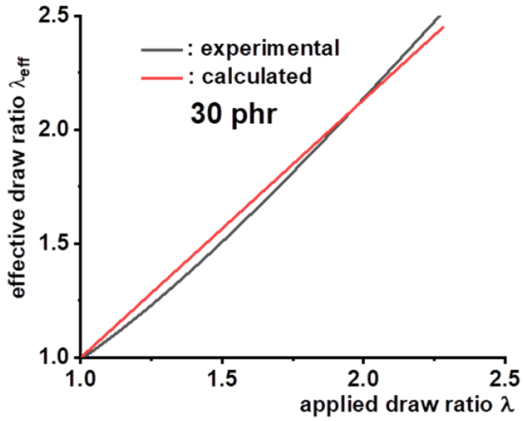

Figure 3.17 Effective draw ratio vs. applied draw ratio in a powder silica (30phr) filled PDMS elastomer

Table 3.1 Powder silica filled samples: experimental and calculated strain amplification coefficients ($a_\varepsilon(\varphi)_{exp}$ *and* $a_\varepsilon(\varphi)_{cal}$)

Silica content (phr)	11	15	18	20	25	25**	30	33	35	40	43
$a_\varepsilon(\varphi)_{cal}$*	1.05	1.07	1.08	1.09	1.11	1.11	1.13	1.15	1.15	1.18	1.19
$a_\varepsilon(\varphi)_{exp}$	0.9	1.03	1.2	1.01	1.14	1.28	1.15	1.26	1.19	1.13	1.24

* based on the formula $a_\varepsilon(\varphi)_{cal} = 1/(1-\varphi)$
** different batch

3.4.2.2 Sol-gel silica filler

Similar to what is done for powder silica filled PDMS elastomer, the effective elongation vs. applied elongation curve of a representative example (28 phr sol-gel silica filled PDMS) is given in **Figure 3.18**. Contrary to the case of powder filled samples, we observe a very strong mismatch between the two curves: the experimental effective elongation of the gum is much higher than the expected behavior $\lambda_{eff} = (\lambda - \varphi)/(1-\varphi)$.

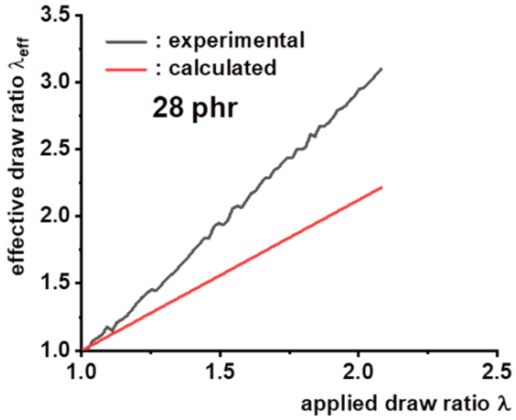

Figure 3.18 Effective draw ratio vs. applied draw ratio in a sol-gel silica (28phr) filled PDMS elastomer

The experimental strain amplification factors that are collected in **Table 2** for the different filler contents are systematically higher than the expected ones; an approximately linear increase with filler content is observed. To the best of our knowledge this effect has not been yet reported.

Table 3.2 Sol-gel silica filled samples: experimental and calculated strain amplification coefficients ($a_\varepsilon(\varphi)_{exp}$ *and* $a_\varepsilon(\varphi)_{cal}$)

Silica content (*phr*)	9	13	16	24	28	35
$a_\varepsilon(\varphi)_{cal}$*	1.04	1.06	1.07	1.11	1.12	1.15
$a_\varepsilon(\varphi)_{exp}$	1.47	1.54	1.58	1.92	1.97	2.31

* based on the formula $a_\varepsilon(\varphi) = 1/(1-\varphi)$

The high value for the strain amplification factor will be confirmed in **Chapter 4** where changes in the low-temperature crystalline texture are observed at much lower draw ratios in sol-gel filled samples. As anticipating example, we compare in **Figure 3.19** diffraction patterns obtained at a similar draw ratio for powder silica and sol-gel filled samples with close silica content. Differences are obvious and using sol-gel filled samples will prove useful when the sample holder does not permit to submit the sample to high draw ratios.

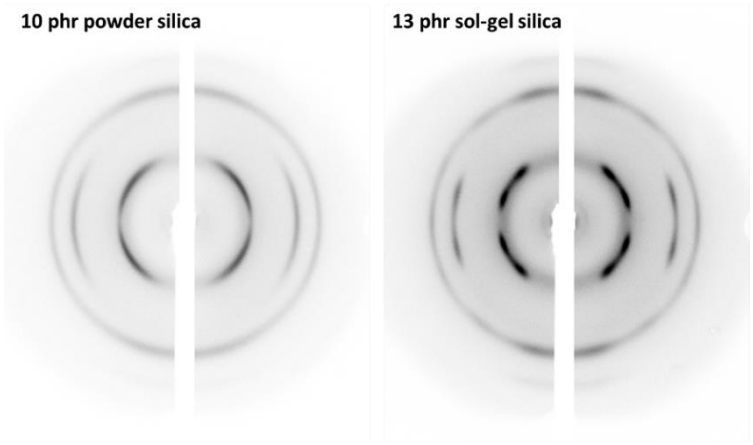

-A- **-B-**

Figure 3.19 Low-temperature crystalline texture obtained at a preset elongation of about 1.5: -A- powder silica filling; -B- sol-gel silica filling procedures. Stretching direction is vertical.

3.4.3 Silica-filled PDMS samples in high-strain region

Three pictures are displayed in **Figure 3.20** to illustrate the evolution of the diffraction patterns during deformation in the high-strain region. At λ = 4, the amorphous halo has become well-modulated in intensity and Legendre polynomials up to l = 3 are necessary to adjust the ϕ-scans (ie. up to $\langle P_6^{RX} \rangle$). At λ = 5, a well-defined spot appears in equatorial position (red arrow) and it becomes highly visible on the last pattern (λ = 6.4).

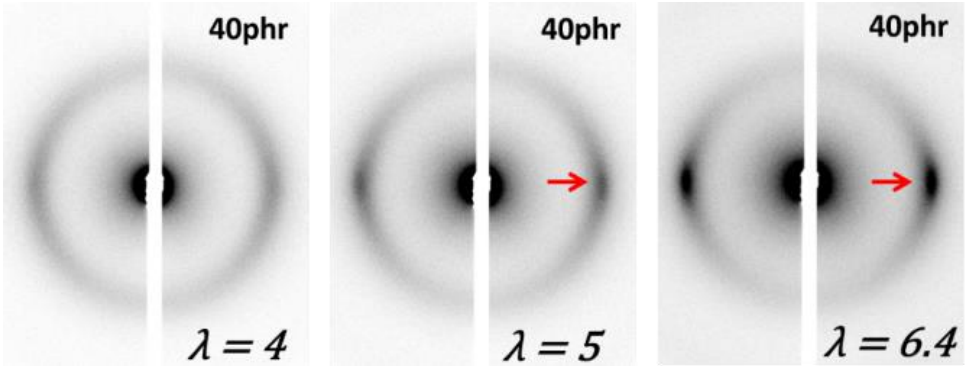

Figure 3.20 Evolution of the X-ray patterns at higher draw ratios (powder silica filled sample)

Tosaka *et al.*[17] have been probably the first to explicitly report this specific equatorial reinforcement that they associate to the apparition of a "mesomorphic phase". It is slightly off-centered with respect to the maximum of the amorphous halo (**Figure 3.21-B**) and this has been used by Tosaka *et al.* to quantify its development (**Figure 3.21-C**; beware that strain ratios are draw ratios minus one). This "mesomorphic phase" is also manifested by the faint azimuthal features indicated by white arrows in **Figure 3.21-A**.

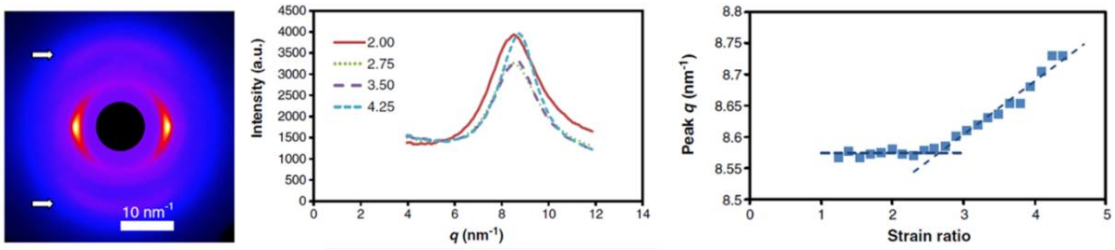

-A- **-B-** **-C-**

Figure 3.21 -A- "Yellow spot": equatorial reflection for the "mesomorphous phase". Additional features are pointed to by white arrows (unspecified draw ratio). -B- equatorial profiles -C- position of the maxima in Figure 3.20-B (after Tosaka *et al.*[17]).

We have plotted in **Figure 3.22** the ratio of the equatorial peak intensity to the total intensity as measured from the ϕ-scans on a 40 phr powder silica filled sample. Rather similar curves are obtained for other silica contents. It confirms that the "mesomorphous phase" essentially develops for elongation above 4 and does not account for more than 10% of the scattered intensity within the amorphous halo at ca. 6.5. We will see in **Chapter 4** it is interesting as a precursor of the high-strain crystalline texture.

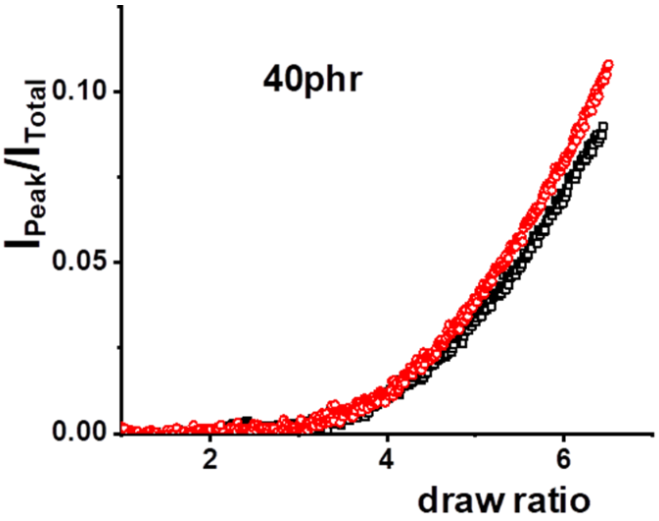

Figure 3.22 Elongation dependence of the proportion of the intensity scattered into the "mesomorphous" equatorial spot.

The equatorial peak associated to the "mesomorphous phase" is located within a ϕ-angular interval $\pm 20°$. This angular zone was removed from adjustement procedure in order to characterize the orientation of the only amorphous fraction. A development comprising Legendre polynomials $P_{2l}(\cos\phi)$ up to l = 3 is necessary to account for the observed intensity modulatio: three coefficients $\langle P_2^{RX}\rangle$, $\langle P_4^{RX}\rangle$ and $\langle P_6^{RX}\rangle$ are thus introduced and their elongation-dependence is given in **Figure 3.23** for all powder-silica filled samples (each curve corresponds to an average over at least two samples).

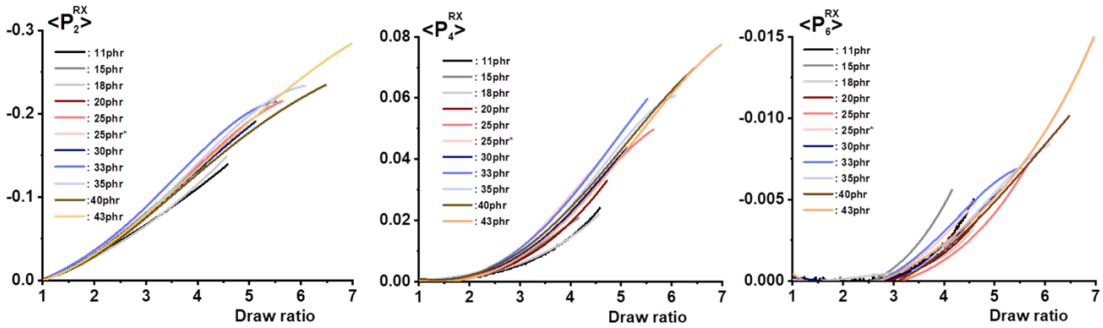

Figure 3.23 $\langle P_2^{RX}\rangle$, $\langle P_4^{RX}\rangle$ and $\langle P_6^{RX}\rangle$ Legendre coefficients for the **powder silica filled samples**. Each curve is an average over at least two samples.

We first see that all curves in each diagram are rather well-grouped, which is not astonishing as the strain-amplification factor does not markedly exceed 1 for all filling contents (see **Table 3.1**). A more surprising fact is that $\langle P_4^{RX}\rangle$ cannot be neglected for draw ratios above say 3: it means that we are out of the Gaussian regime at rather low elongations. Above elongations of ca. 3.5-4, the addition of 6th order Legendre polynomial becomes furthermore necessary.

Mechanical measurements presented in **Section 3.2.3.1** gave an estimate $M_w \approx 23236 g/mol$, that corresponds to 314 siloxane monomers (–Si(CH$_3$)$_2$O–, Mw = 74.15 g/mol). In the model of the freely jointed segments, a polymer chain is represented by *N* statistical segments that can freely oriente independently from each other. In that case, the chain can be drawn to a maximal extension $\sqrt{N}$. In real polymeric chains, there is contraints in the orientation of adjacent monomers and the statistical segment (also called Kuhn segments) is approximated by a few segments. In PDMS, this number of segments has been evaluated to 5-6. [18] . The maximal extensibility is thus reduced to

ca. $\sqrt{314/5.5} \approx 7.5$. Applied elongations of $\lambda > 2$ are no more negligible compared to this value which could explain we are rapidly out of the Gaussian regime.

We now turn to the sol-gel filled samples (**Figure 3.24**). Each curve corresponds to a single sample which somehow diminishes the reliability of the data. At the difference of what is observed with powder silica filled samples, increasing values are observed with increasing filler content at a given draw-ratio. This reflects the fact that strain amplification factor increases rapidly as the silica content increases (see **Table 3.2**).

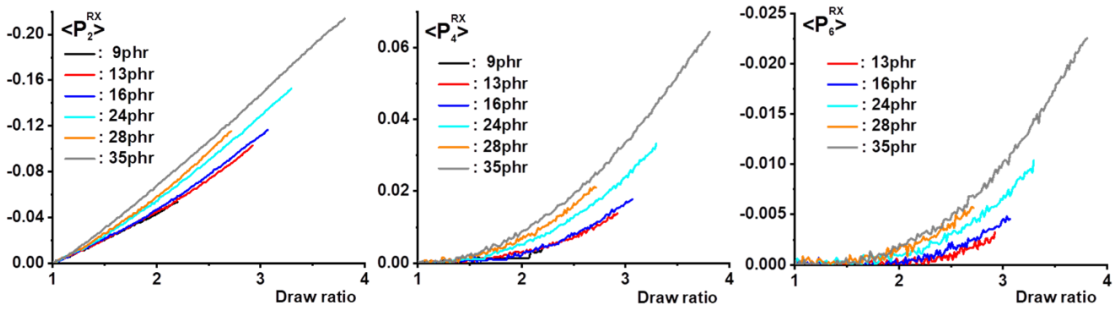

Figure 3.24 $\langle P_2^{RX} \rangle$, $\langle P_4^{RX} \rangle$ and $\langle P_6^{RX} \rangle$ Legendre coefficients for the **sol-gel silica filled samples**. Each curve corresponds to a single sample.

References

[1] Albouy, P. A., Guillier, G., Petermann, D., Vieyres, A., Sanseau, O., & Sotta, P. (2012). A stroboscopic X-ray apparatus for the study of the kinetics of strain-induced crystallization in natural rubber. *Polymer*, 53(15), 3313-3324.

[2] Farfán-Cabrera, L. I., Pascual-Francisco, J. B., Gallardo-Hernández, E. A., & Susarrey-Huerta, O. (2018). Application of digital image correlation technique to evaluate creep degradation of sealing elastomers due to exposure to fluids. *Polymer Testing*, 65, 134-141.

[3] Pritchard, R. H., Lava, P., Debruyne, D., & Terentjev, E. M. (2013). Precise determination of the Poisson ratio in soft materials with 2D digital image correlation. *Soft Matter*, 9(26), 6037-6045.

[4] Meunier, L., Chagnon, G., Favier, D., Orgéas, L., & Vacher, P. (2008). Mechanical experimental characterisation and numerical modelling of an unfilled silicone rubber. *Polymer Testing*, 27(6), 765-777.

[5] Mark, J. E. (1975). The Constants 2C1 and 2C2 in Phenomeno-Logical Elasticity Theory and Their Dependence on Experimental Variables. *Rubber Chemistry and Technology*, 48(3), 495-512.

[6] Mark, J. E. (Ed.). (2007). Physical properties of polymers handbook (Vol. 1076, p. 825). New York: Springer.

[7] Cai, L. H., Kodger, T. E., Guerra, R. E., Pegoraro, A. F., Rubinstein, M., & Weitz, D. A. (2015). Soft Poly (dimethylsiloxane) Elastomers from Architectur-Driven Entanglement Free Design. *Advanced Materials*, 27(35), 5132-5140.

[8] Wang, S., Xu, P., & Mark, J. E. (1991). Shear and biaxial extension measurements of reinforcement from in-situ precipitated silica. *Rubber Chemistry and Technology*, 64(5), 746-759.

[9] Domurath, J., Saphiannikova, M., Ausias, G., & Heinrich, G. (2012). Modelling of stress and strain amplification effects in filled polymer melts. *Journal of Non-Newtonian Fluid Mechanics*, 171, 8-16.

[10] Inoue, T., Narihisa, Y., Katashima, T., Kawasaki, S., & Tada, T. (2017). A rheo-optical study on reinforcement effect of silica particle filled rubber. *Macromolecules*, 50(20), 8072-8082.

[11] Bokobza, L. (2004). The reinforcement of elastomeric networks by fillers. *Macromolecular Materials and Engineering*, 289(7), 607-621.

[12] Nobbs, J. H., & Bower, D. I. (1978). Orientation averages for drawn rubber networks. *Polymer*, 19(9), 1100-1103.

[13] Doi, M., Edwards, S. F., & Edwards, S. F. (1988). The theory of polymer dynamics (Vol. 73). Oxford university press.

[14] Mitchell, G. R., & Windle, A. H. (1982). Conformational analysis of oriented non-crystalline polymers using wide angle X-ray scattering. *Colloid and Polymer Science*, 260(8), 754-761.

[15] Mitchell, G. R. (1984). A wide-angle X-ray study of the development of molecular orientation in crosslinked natural rubber. *Polymer*, 25(11), 1562-1572.

[16] Albouy, P. A., & Sotta, P. (2020). Draw ratio at the onset of strain-induced crystallization in cross-linked natural rubber. *Macromolecules*, 53(3), 992-1000.

[17] Tosaka, M., Noda, M., Ito, K., Senoo, K., Aoyama, K., & Ohta, N. (2013). Strain-and temperature-induced polymorphism of poly (dimethylsiloxane). *Colloid and Polymer Science*, 291(11), 2719-2724.

[18] Gilra, N., Cohen, C., Briber, R. M., Bauer, B. J., Hedden, R. C., & Panagiotopoulos, A. Z. (2001). A SANS study of the conformational behavior of linear chains in compressed and uncompressed end-linked elastomers. *Macromolecules*, 34(22), 7773-7782.

Chapter 4

Structural Evolution of Poly (dimethyl siloxane) during Stretching: X-ray Fiber Pattern Analysis and Simulation

Contents

4.1 Introduction

We emphasized in **Chapter 1** the impressive evolution of WAXD patterns at low temperature depending upon the applied extension. This observation has been reported by some authors, but Tosaka *et al*. were the first to investigate it carefully and record intermediate steps [30] : **Figure 4.1** is taken from their publication. We see that the inner reflections for example start to split as the draw ratio increases, and move continuously to their final locations: this splitting typically appears at a draw ratio exceeding 2 and no more evolution is observed above 5-6.

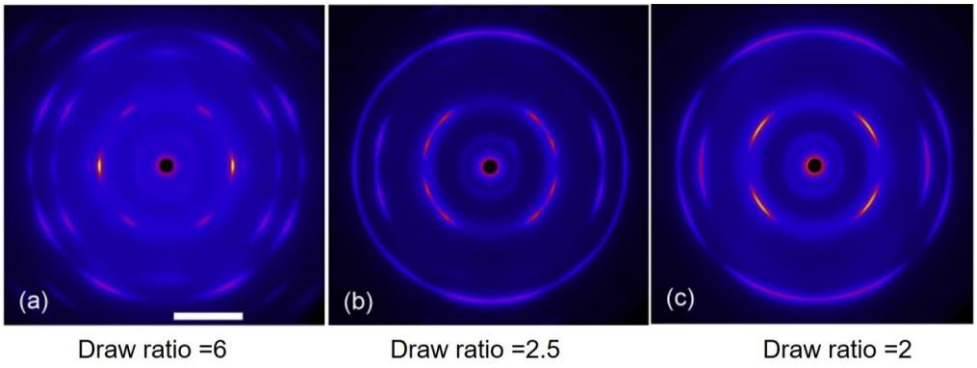

Figure 4.1 WAXD patterns[30] of cross-linked PDMS samples crystallized at −90 °C. Stretching direction is vertical. Cu Kα radiation was used as the X-ray source.

Two explanations were proposed to explain these changes: (1) in the above-mentioned publication, Tosaka *et al.* [30] proposed a polymorphism with two phases (this polymorphism was increased to four phases in a subsequent paper[2], see **Chapter 1)**: the high stretch phase called ***β*** that would correspond to the monoclinic phase proposed by Damaschun [3], while the low stretch phase called ***α*** that would correspond to the tetragonal phase described by Albouy[1] . (2) On the other side Albouy originally suggested that a simple texture change was responsible for this evolution, the crystalline structure remaining tetragonal [4]. In order to clarify this point, a systematic study was carried on: it is presented in what follows.

We present here only WAXD patterns obtained at low temperature; however, they were continuously recorded with the tensile force during the cooling sequence necessary to reach crystallization, and during the following warming. The evolution of the mechanical properties in relation to the crystallization process is presented in detail in the following **Chapter 5**.

4.2 Experimental section

4.2.1 Material and sample preparation

Silicone rubbers used for these experiments are two types: (i) hexamethylsilazane-treated silica-filled networks based on vinyl-terminated PDMS (M_W= 43000). Samples are given a dumbbell-shape that allows the use of rather small grips (ca 30mm in length, 6 mm in width and 1 mm in thickness). 1 mm thick samples are quite absorbing at the wavelength of copper (0.1542nm) but this is not a real problem as the thickness is diminished by a factor $\sqrt{\lambda}$ for an extension λ. (ii) We emphasized in **Chapter 3** the interest presented by sol-gel silica filled samples due to their high strain amplification factor. They have been used with a shorter wavelength set-up presented in the next section. WAXD patterns obtained in that case present a much better definition of the intensity reinforcements and they are presented below as representative examples for the two extreme strain-states.

4.2.2 Tensile WAXS measurements.

The homemade tensile WAXS setup (Cu Kα radiation, λ = 0.15418 nm) presented in **Chapter 3** does not allow to cool the sample below ca. $-10\,°C$. Some adaptation was thus necessary and they are presented in details in **Chapter 5**. Diffraction patterns presented here have been acquired at ca. $-110\,°C$ and this is the minimum temperature reached after cooling. It is close to T_g and no more evolution is expected at lower temperatures. The value of the preset elongation is obtained from the distance between red ink marks on the sample.

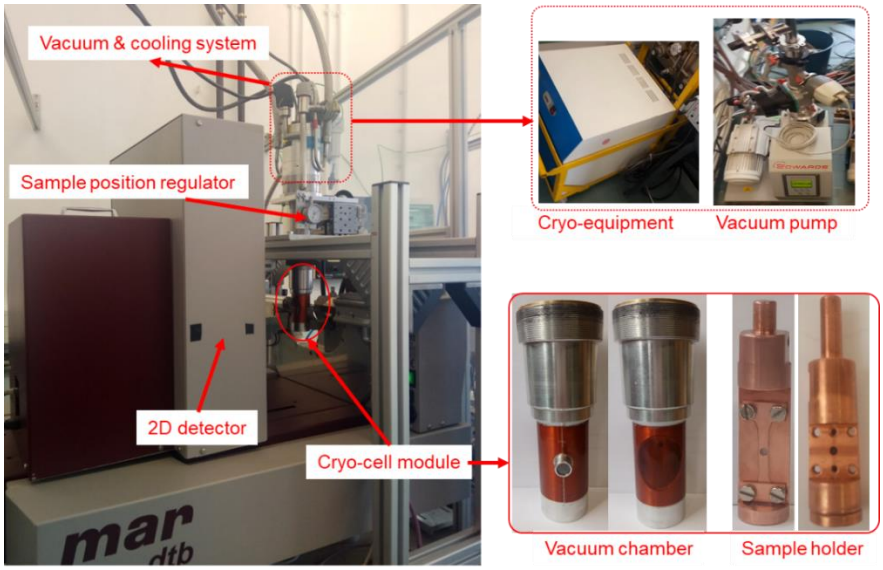

Figure 4.2 The setup used for WAXD pattern acquisition at low temperature and molybdenum wavelength (0.071nm). The reduced size of the sample holder only allows moderate extension.

As said above, these experiments have been completed by the acquisition of some patterns with another setup working at the wavelength of molybdenum (0.071nm). A shorter wavelength allows a larger fraction of the reciprocal space to be observed but the sample holder only allows the application of moderate draw ratios (**Figure 4.2**: see the size of the sample holder). Furthermore, cooling and warming times are quite long and do not allow for a rapid sample change. Only a few extensions were investigated.

4.3 WAXD pattern simulation methodology

Whatever explanation about the X-ray pattern evolution will turn correct, it is necessary to be able to simulate diffraction diagrams associated to a given texture (orientation of crystallites) for a given structure (structure of each crystallite). For this purpose, we received the help of Pascale LAUNOIS (LPS, team MATRIX), who developed a sophisticated software for the simulation of WAXD patterns. In what follows, we give a simplified overview of the way it operates.

4.3.1 Geometry of scattering

The scattering geometry that corresponds to the stretching apparatus is first recalled in **Figure 4.3**.

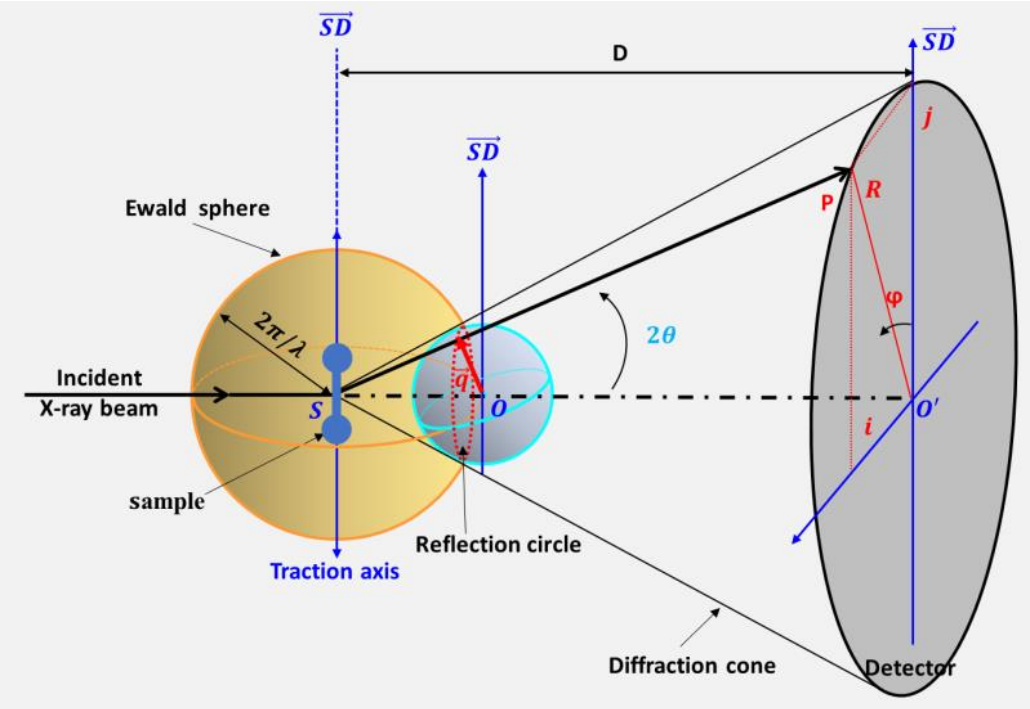

Figure 4.3 Sketch of the scattering geometry presently used. The blue sphere in the portion of the reciprocal space that corresponds to a given hkl reflection for the whole crystallites.

Sample and detector are normal to the X-ray primary beam. The stretching axis of the sample $\overrightarrow{\boldsymbol{SD}}$ is parallel to the plane of the detector. We have represented the Ewald sphere which is a geometric construction that allows visualize the occurrence of scattering points. It is a virtual sphere of radius $2\pi/\lambda$ (incident wave-vector modulus) centered on the sample, $\boldsymbol{S}$. The origin, $\boldsymbol{O}$, of the reciprocal space is at the intersection of the transmitted X-ray beam and of this sphere. The conservation of wave-vectors implies that scattering is observable only for reciprocal lattice points lying on the Ewald sphere.

The intensity of the hkl reflection associated to crystallites grown in the sample is distributed over a sphere of radius $2\pi/d_{hkl}$ in the reciprocal space. This distribution depends upon the crystallite orientation Only those crystallites that have the proper orientation with respect to the incident beam will diffract: they are oriented so that the extremity of the associated scattering vector is located on the red dotted circle that intercepts the Ewald sphere. The scattered intensity is localized on the grey cone whose intercept with the detector is represented by a black circle.

Specifically, the scattering vector $\vec{\boldsymbol{q}}$ colored in red is associated to those reflecting crystallites whose (hkl) planes are perpendicular to it (their orientation is represented by the light-blue circle in the figure). They give rise to the scattered intensity $\boldsymbol{I}(\boldsymbol{i},\boldsymbol{j})$ collected at point $\boldsymbol{P}(\boldsymbol{i},\boldsymbol{j})$ on the detector. The coordinates $(\boldsymbol{i},\boldsymbol{j})$ are related to the scattering angle $\boldsymbol{2\theta}$ and the azimuthal angle $\boldsymbol{\varphi}$ by:

$$\tan 2\theta = \sqrt{i^2 + j^2}/D = R/D$$
$$\tan \varphi = i/j \qquad (4.1)$$

Where the angle $\boldsymbol{\theta}$ is given by the Bragg relation

$$\sin \theta = \lambda/2d_{hkl} \qquad (4.2)$$

where λ is the X-ray wavelength, do not to confuse with the elongation.

It is recalled that the scattering vector $\vec{\boldsymbol{q}}$ (red vector in the figure) is perpendicular to the $(\boldsymbol{h}\ \boldsymbol{k}\ \boldsymbol{l})$ planes and its modulus is

$$|\vec{\boldsymbol{q}}| = q = \frac{4\,\pi \sin\theta}{\lambda} = \frac{2\pi}{d_{hkl}} \qquad (4.3)$$

In this way the scattering intensity $\boldsymbol{I}(\boldsymbol{2\theta},\boldsymbol{\varphi})$ in the 2D detector can be related to the intensity $\boldsymbol{I}(\vec{\boldsymbol{q}})$ associated to the specific scattering vector $\vec{\boldsymbol{q}}$, that is in turn associated to a specific orientation of the crystallites.

4.3.2 General simulation procedure

It is assumed in what follows that some specific direction $\overrightarrow{PA}$ within a given crystallite will preferentially align along the traction axis under stretch. This hypothesis is supposed to hold for all polymorphic phases if present. The simulation includes four steps:

(1) Calculate the overall scattering intensity in the framework of a crystallite. The program can compute diffusion structure factors if the atomic positions are known. Otherwise intensities are given preset values.

(2) The contribution of all crystallites whose framework share a similar orientation with respect to the direction $\overrightarrow{PA}$ is computed: it is obtained by rotation around $\overrightarrow{PA}$.

(3) Perform averages over all allowed $\overrightarrow{PA}$ orientations. For this purpose, it is necessary to introduce an orientation distribution function (ODF). Due to the uniaxial (cylindrical) symmetry of the problem, it only depends upon the angle β between the direction $\overrightarrow{PA}$ and the traction axis (also called "fiber axis"; averaging around the traction axis must be thus performed for each β value).

(4) Use the Ewald sphere construction to relate a pixel on the image to a wave-vector and thus to attribute an intensity to this pixel.

We now give some details about each of these steps.

(1) Calculate the scattering intensity $I(\vec{q})$ for a given crystallite

The direct space lattice associated to a given crystallite is characterized by the three basis vectors $\vec{a}, \vec{b}, \vec{c}$ and the reciprocal space lattice by the three basis vectors $\vec{a}^*, \vec{b}^*, \vec{c}^*$; those vectors are related by the relations: $\vec{a}_i \cdot \vec{a}_j^* = 2\pi\delta_{ij}$ (with $a_1 \leftrightarrow a$, $a_2 \leftrightarrow b$ etc…). For an infinite crystallite the intensity in the reciprocal space is localized at the scattering vectors (if the diffuse thermal scattering is neglected)

$$\vec{q}_{hkl} = h\vec{a}^* + k\vec{b}^* + l\vec{c}^* \tag{4.4}$$

and can be described by a δ-function:

$$I(\vec{q}) = \sum_{h,k,l} I_{hkl}(\vec{q})\delta(\vec{q} - \overrightarrow{q_{hkl}}) \tag{4.5}$$

where $I_{hkl}(\vec{q})$ are arbitrary or estimated intensity values.

The Bragg peaks are then convoluted by a Gaussian function to account for the experimental resolution (beam parallelism) and finite size broadening. Crystallite dimensions can be different according to the considered direction and a Gaussian ellipsoid around each Bragg peak is more appropriate. For the sake of simplicity, we presently chose an isotropic broadening and the intensity can be written:

$$I(\vec{q}) = \sum_{h,k,l} I_{hkl}(\vec{q}) \left(\frac{1}{2\pi\sigma^2}\right)^{\frac{3}{2}} e^{-\frac{|\vec{q}-\vec{q_{hkl}}|^2}{2\sigma^2}} \quad (4.6)$$

The Gaussian RMS width σ controls the width of the diffraction peak.

The calculation is performed on a parallelepiped network with "reasonable" steps so as to limit the computing time. Interpolation can be performed to reduce the mesh size without impacting the correctness of the space description.

(2) Calculate the averaged orientational scattering intensity $I(\vec{q})_{PA}$

As explained above we assume that some specific crystallographic direction ($\overrightarrow{PA}$) in a crystallite will preferentially align along the traction axis ($\overrightarrow{SD}$) of the sample: see **Figure 4.4**.

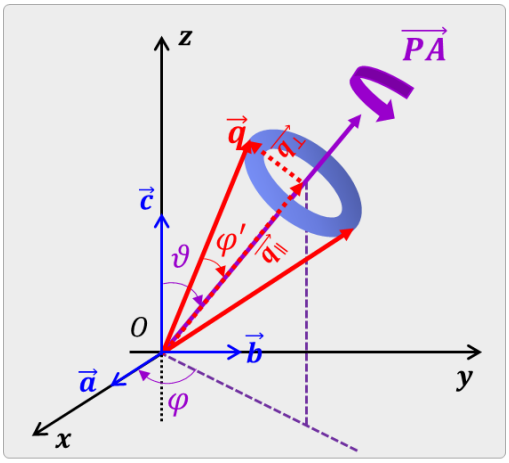

Figure 4.4 Second step: average around a given preferential orientation direction $\overrightarrow{PA}$.

We consider a scattering vector $\vec{q}$ associated to the hkl reflection: according to **Equation 4.6** it is located in a spherical area surrounding the node vector $\vec{q}_{hkl}$. The contribution of all crystallites that share the common direction ($\overrightarrow{PA}$) is obtained by rotating around ($\overrightarrow{PA}$). The corresponding scattering vectors $\vec{q}$ become localized in the blue-grey tore sketched in **Figure 4.4**.

(3) Calculate the averaged scattering intensity distribution $I(\vec{q})_{FA}$

We illustrate in **Figure 4.5** the two operations that finish the description of the crystalline texture: for each angle $\boldsymbol{\beta}$ (violet arrow) between the preferential orientation axis $\overrightarrow{\boldsymbol{PA}}$ and the fiber axis $\overrightarrow{\boldsymbol{FA}}$ (traction axis) a rotation around $\overrightarrow{\boldsymbol{FA}}$ is performed to take into account the uniaxial (ie. cylindrical) symmetry of the problem (blue arrows).

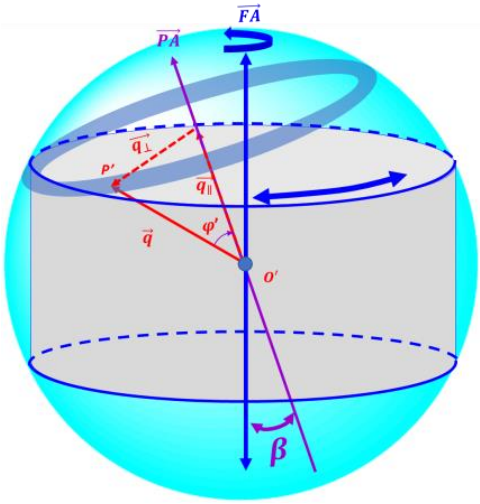

Figure 4.5 The projection of the spots in the reciprocal space onto the planar detector from the stretched sample.

The orientation distribution function is chosen Gaussian:

$$p(\beta) \propto e^{-ln(2)\frac{\beta^2}{w^2}} \qquad (4.7)$$

From a practical point of view, a relation must be established between the different relevant angles that are represented in **Figure 4.6**. At a given value of φ', angles φ and ψ are changed to account for the first operation that consists in a rotation around $\overrightarrow{PA}$. The cylindrical symmetry imposes rotation around $\overrightarrow{PA}$ for each β value.

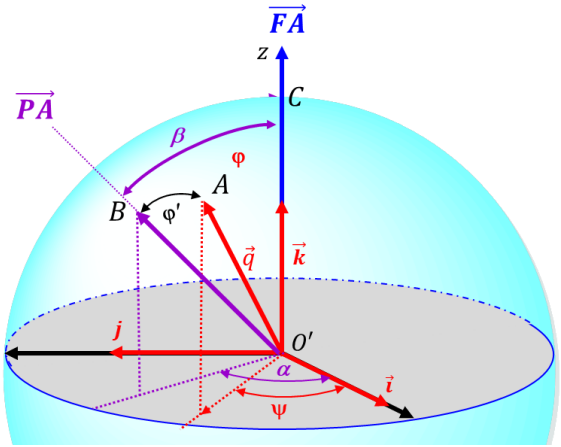

Figure 4.6 Illustration of the geometric relationship between the scattering vector $\vec{q}$ and the primary axes of the fiber $\overrightarrow{FA}$ and the preferred orientation $\overrightarrow{PA}$.

The following relation is implemented in the software

$$\cos\varphi' = \cos\beta\cos\varphi + \sin\beta\sin\varphi\cos(\alpha - \psi) \quad (4.8)$$

It is easily established noting that $\cos\varphi' = \overrightarrow{O'A} \cdot \overrightarrow{O'B}$ and using the following relation for the vectors $\overrightarrow{O'A}$ and $\overrightarrow{O'B}$

$$\overrightarrow{O'A}(\varphi,\psi) = \vec{\imath}\sin\varphi\cos\psi + \vec{\jmath}\sin\varphi\sin\psi + \vec{k}\cos\varphi$$
$$\overrightarrow{O'B}(\beta,\alpha) = \vec{\imath}\sin\beta\cos\alpha + \vec{\jmath}\sin\beta\sin\alpha + \vec{k}\cos\beta \quad (4.9)$$

(4) Construct the WAXD patterns

The last step consists in the reconstruction of the WAXS pattern: it is based on the diffraction geometry depicted in **Figure 4.3**, where the intensity at the extremity of red scattering vector $\vec{q}$ gets related to the intensity measured at $P(i,j)$ on the detector.

4.4 Results and discussion

4.4.1 WAXD patterns at increasing stretching ratios

We display in **Figure 4.7** the evolution of the WAXD patterns that we observed for a 10% silica-filled specimen from the quiescent state (**λ=1**) to a highly stretched state (**λ=7.7**; this last value is deduced from transmission data and is over-estimated).

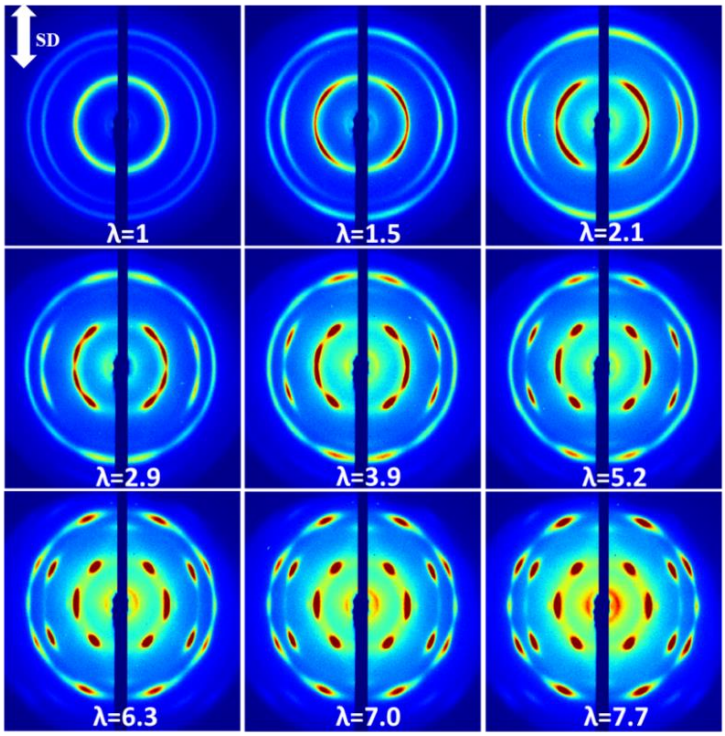

Figure 4.7 WAXD patterns measured at about -100 °C with respect to different elongation **λ** from dumbbell shape PDMS elastomer filled with 10 wt% silica. Cu Kα radiation was used as the X-ray source and the stretching direction (SD) is vertical as shown by the white double-headed arrow.

It comforts Tosaka *et al* observation (originally done by Ohlberg in 1957): starting from an isotropic pattern at **λ=1** a first structuration is observed similar to the one reported by Albouy. The various intensity reinforcements start to split and move at $\lambda > 2.1$. This progressive change is completed at $\lambda \geq 6$: at this stage, patterns are similar to Damaschun's report.

Radial scans performed on the patterns displayed in **Figure 4.7** are superimposed in **Figure 4.8-A**. As quoted above some diffraction patterns have been recorded at a shorter wavelength (0.07107nm) that results in a higher explored *q*-range. The corresponding radial scans are displayed in **Figure 4.8-B**: we plotted the square root of the intensity in ordinate so as to evidence weaker diffraction lines. It is clear that in neither case does the position of the diffraction lines changes. Similarly, only restricted changes in relative intensity are observed that can be due to the texturing effect. These similarities have been recognized as antagonistic to crystalline phase changes by Tosaka *et al* [1]: their explanation of this paradox is somewhat intricate. In view of these results, we tested the hypothesis that the observed changes might be simply related to texture changes, that is changes in the preferential orientation axis.

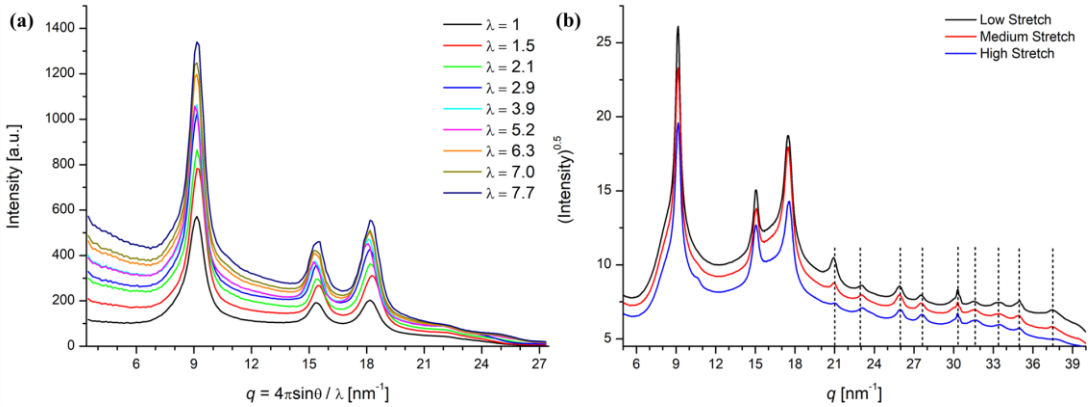

Figure 4.8 One-dimensional WAXD profile of PDMS elastomer measured at about -100 ℃ under different elongation **λ**. (a) copper radiation (0.1542nm), (b) molybdenum radiation (0.07107nm)

4.4.2 Fiber pattern simulation and comparison

A logical start for the lower stretches is the tetragonal unit cell initially proposed by Albouy [4]. The unit cell with parameters are a ≈ 0.836 nm and $\boldsymbol{c}$ =1.2 nm and the space group $I\,4_1$ (No. 80). The *d*-spacing for an ($\boldsymbol{hkl}$) family of planes is given by the relation.

$$\frac{1}{d_{hkl}^2} = \frac{h^2 + k^2}{a^2} + \frac{l^2}{c^2} \tag{4.10}$$

An important point is that the parameter ***c*** is very close to $a\sqrt{2}$, so that

$$\frac{1}{d_{hkl}^2} \approx \frac{2h^2 + 2k^2 + l^2}{c^2}$$

In these conditions and with regard to the limited experimental resolution of the set-up, most diffraction lines have more than one possible ***hkl*** assignment. We give in **Table 4.1** the line indexation for the four first lines that can be observed on the diffraction patterns in **Figure 4.7-A**. It is shown in **Chapter 6** that some of these lines can be separated with a higher resolution set-up and actually $c \neq a\sqrt{2}$.

Table 4.1 Indexation of the diffraction lines that can be observed in **Figure 4.7**.

Reflection	1st line	2nd line	3rd line	4th line
miller index (hkl)	(101)	(200) (112)	(103) (211)	(004) (220)

We first examined X-ray diagrams obtained at low extension, typically $\lambda \leq 2.1$ in **Figure 4.7**. As underlined above, it appeared that intensity reinforcements were much better defined for the sol-gel silica filled samples although the actual elongation the PDMS is subjected to is quite similar. The pattern displayed in **Figure 4.9** has been obtained with such a sample using the shorter wavelength apparatus presented in **Figure 4.2.** (see above) The fiber axis is the tetragonal *c*-axis and the different reflection layers are underlined by a dotted with line [4].

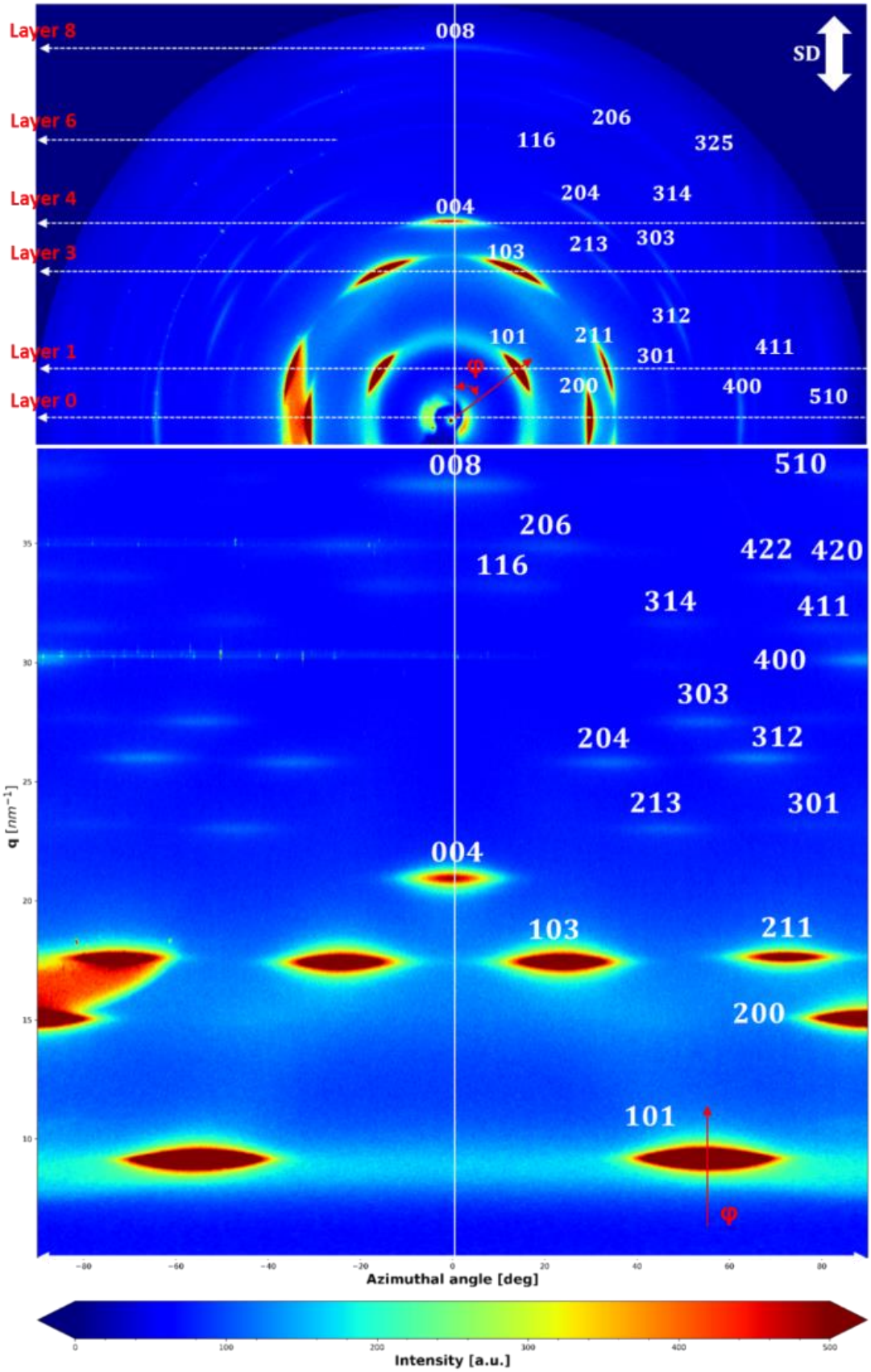

Figure 4.9 Pattern analysis of crosslinked PDMS measured at 130K (λ= ca. 1.4). Mo Kα radiation was used as the X-ray source, q is the scattering vector and its modulus satisfies $\boldsymbol{q} = |q| = 4\pi \sin\theta/\lambda = 2\pi/d$, ϕ is the azimuthal angle with respect to the vertical direction of stretching (SD).

A diffraction pattern simulation with the *c*-axis as fiber axis is given in **Figure 4.10**; the parameter ***w*** for the ODF is set to 20 °. The reinforcement positions are correctly accounted which supports Albouy's original claim [4].

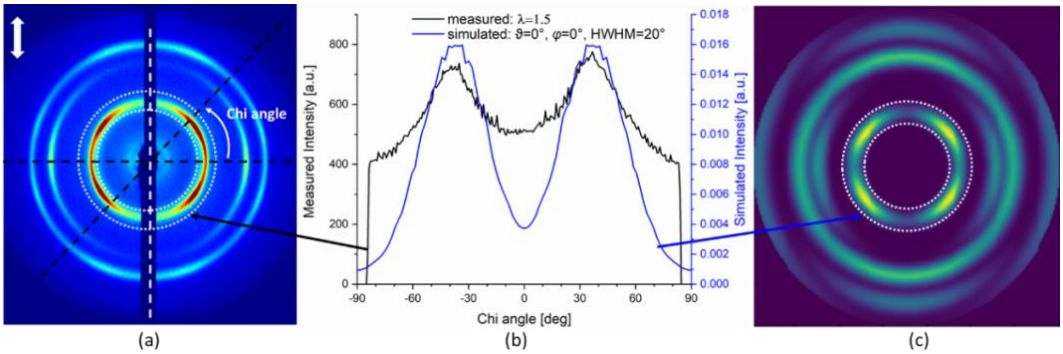

Figure 4.10 The (a) measured and (c) simulated WAXD patterns under small elongation ($\lambda = 1.5$), (b) the measured and simulated angular intensity distribution of the first reflection (101). The **Chi angle** refers to the angle between the angular direction of interest and the horizontal axis (which is normal to the vertical stretching direction, shown by the white double-headed arrow), Cu Kα radiation was used as the X-ray source.

The next step has been to determine if the high stretch pattern can be accounted for with this same tetragonal structure by choosing the appropriate crystallographic direction as new fiber axis. For this purpose, the preferential orientation $\overrightarrow{PA}$ defined by the spherical angles (ϑ, φ) within the referential of a given crystallite has been systematically changed by 5 ° increments (**see Figure 4.4**). The resulting simulations are compared to the experimental diagram till a proper agreement is found. This highly time-consuming step (ca. two days calculation) proved successful and a good correspondence was found for $(\vartheta, \varphi, \mathrm{w})$ = (45 °, 45 °, 7 °): see **Figure 4.11**.

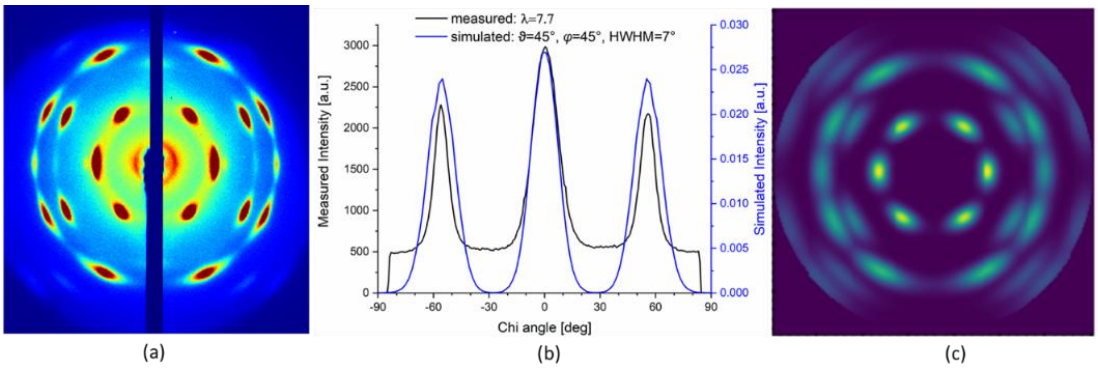

Figure 4.11 The (a) measured and (c) simulated WAXD pattern under high elongation ($\lambda = 7.7$), (b) the measured and simulated angular intensity distribution of the first reflection (101). Cu Kα radiation was used as the X-ray source and the stretching direction (SD) is vertical.

It is very close to the real space direction $\vec{a} + \vec{b} + \vec{c}$ for which $\varphi = 45°$ and $\vartheta \approx 44.6°$. Indeed, this result could have been guessed beforehand: it is clear in **Figure 4.11-A** and from the evolution of the patterns in **Figure 4.7** that the reflection that stays in azimuthal position in the high stretch diagrams originates from the second intense diffraction ring. This ring was originally indexed as **200** and intensity reinforcements at low stretch comfort this assignation. However, a closer examination of the patterns reveals that the ***112*** reflection although very weak is present. Localizing the **112** reflection in azimuthal position means that the fiber axis direction is $\vec{a}^* + \vec{b}^* + 2\vec{c}^*$; as $c \approx \sqrt{2}a$ this direction is very close to $\vec{\imath} + \vec{\jmath} + \vec{k}\sqrt{2}$, which is equivalent to the direction $\vec{a} + \vec{b} + \vec{c} = \boldsymbol{a} \cdot (\vec{\imath} + \vec{\jmath} + \vec{k}\sqrt{2})$ with the same degree of approximation. We give in **Figure 4.12** the diffraction diagram obtained at shorter wavelength with a sol-gel silica filled PDMS sample.

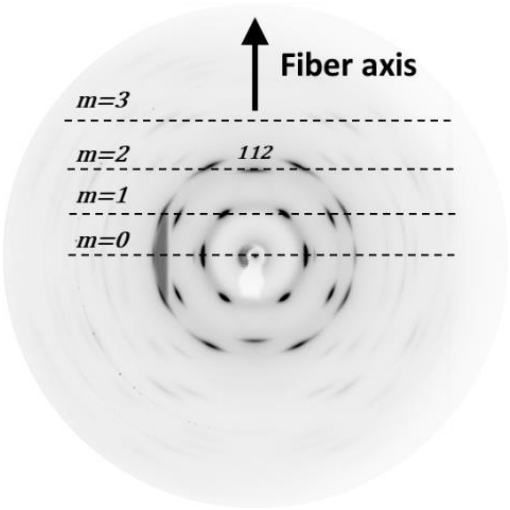

Figure 4.12 Fiber pattern taken at high stretch (λ ≈2.5) with a sol-gel filled (25%) sample (wavelength: 0.071nm; average on 15 patterns, exposure time: 1hr per pattern).

This pattern is similar to a rotating crystal pattern with the fiber axis as rotation direction. The reflection layers are underlined by dotted lines labelled with the ***m***-index in the figure; the **112** reflection was accordingly given the ***002*** indexation by Damaschun and Tosaka *et al.* [1,3]. They interpreted the absence of ***001*** reflections as the proof that the fiber axis was a $\mathbf{2_1}$ axis: this in turn implies a monoclinic structure. We just see that such an interpretation is not necessary.

We now turn to the intermediate stretching states. It was found that a good agreement with simulations was systematically associated to $\boldsymbol{\varphi}$ = 45 ° (see **Figure 4.4** for the definition of this angle): a representative example is displayed in **Figure 4.13**

with $(\vartheta, \varphi, w) = (45°, 30°, 7°)$. It means that the axis of preferential orientation is progressively tilting from the [001] direction to the [111] direction while remaining in the plane of equation ***x* = *y*** (see **Figure 4.4** for the definition of the tetragonal unit cell).

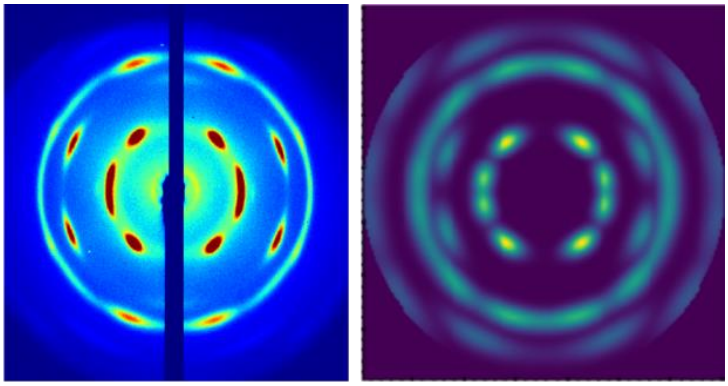

(a) (b)

Figure 4.13 The (a) measured and (c) simulated WAXD pattern under medium elongation ($\lambda = 3.9$).

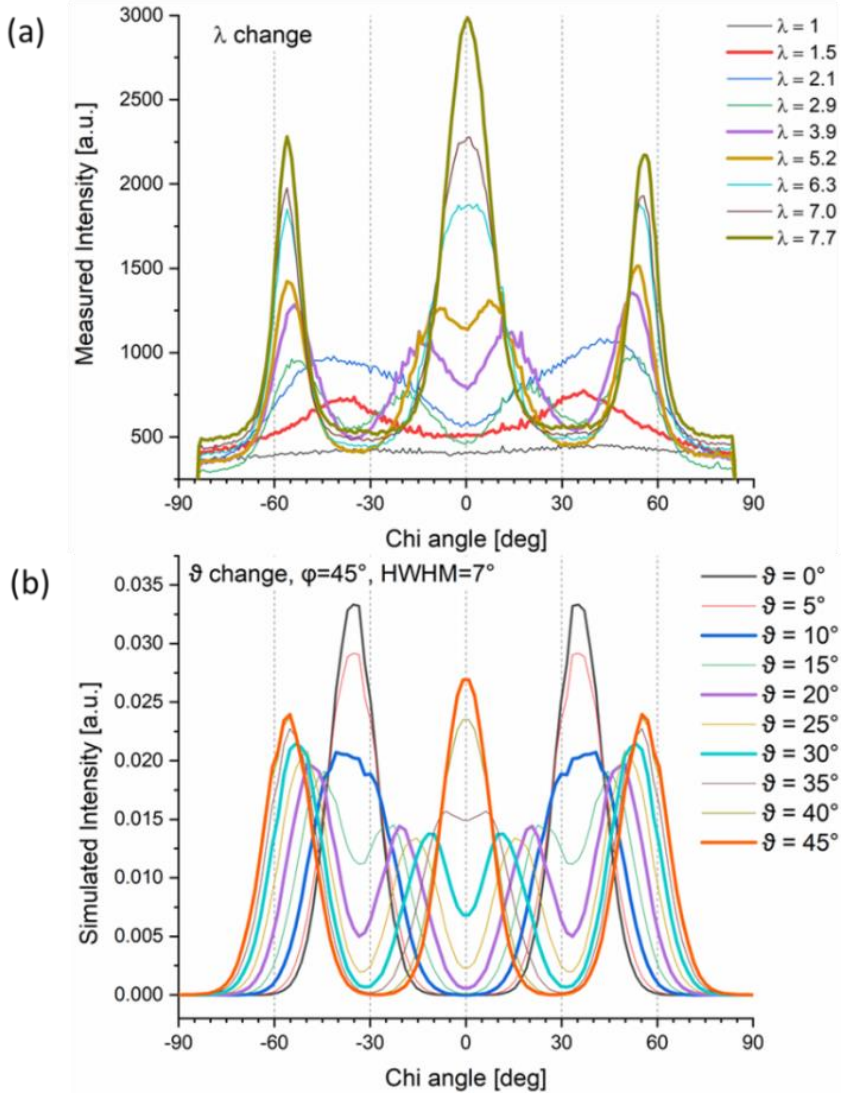

Figure 4.14 (a) measured and (b) simulated angular intensity distribution of the first inner ***101*** reflection.

We have plotted in Figure **4.14-a** angular plots for all experimental patterns displayed in **Figure 4.7** and in Figure **4.14-b** simulations associated to an increasing $\boldsymbol{\vartheta}$–angle ($\vartheta = 0°$ corresponds to the direction [001] as fiber axis and $\vartheta = 45°$ to the direction [111] as fiber axis); the angular width parameter $\boldsymbol{w}$ for the ODF is kept equal 7 °; line intensities are arbitrarily fixed. $\vartheta = 10°$ can be associated to $\lambda = 2.1$, $\vartheta = 30°$ to $\lambda = 3.9$ (see **Figure 4.43**) and $\vartheta = 35°$ to $\lambda = 5.2$.

To summarize, we propose the following mathematical relations for the axis of preferred orientation ($\overrightarrow{\mathbf{PA}}$):

$$\overrightarrow{\mathbf{PA}} = \begin{cases} \vec{\mathbf{c}} & \text{small elongation} \\ \boldsymbol{x}\left(\vec{\mathbf{a}} + \vec{\mathbf{b}}\right) + \vec{\mathbf{c}}\,, \mathbf{0} < \boldsymbol{x} < \mathbf{1} & \text{medium elongation} \\ \vec{\mathbf{a}} + \vec{\mathbf{b}} + \vec{\mathbf{c}} & \text{high elongation} \end{cases}$$

An obvious consequence of the hypothesis of a single crystalline structure with a texture evolution is that the polymer chain orientation changes during stretching: this point is fundamental and will be discussed in **Chapters 6 and 8**.

References

[1] Tosaka, M., Noda, M., Ito, K., Senoo, K., Aoyama, K., & Ohta, N. (2013). Strain- and temperature-induced polymorphism of poly (dimethylsiloxane). *Colloid and Polymer Science*, 291(11), 2719-2724.

[2] Tosaka, M., & Tashiro, K. (2018). Crystal polymorphism and structure models of Poly (dimethylsiloxane). *Polymer*, 153, 507-520.

[3] Damaschun, G. (1962). Röntgenographische untersuchung der struktur von silikongummi. *Kolloid-Zeitschrift und Zeitschrift für Polymere*, 180(1), 65-67.

[4] Albouy, P. A. (2000). The conformation of poly (dimethylsiloxane) in the crystalline state. *Polymer*, 41(8), 3083-3086.

Chapter 5

Thermoelastic Response in Silica filled PDMS Elastomer: Crystallization and Melting under Deformation

Contents

5.1 Introduction

We discussed in **Chapter 4** the effect of a static extension on the evolution of the low-temperature diffraction patterns in the semi-crystalline state. The cooling and warming sequence necessary to reach this state is interesting by itself and offers an occasion to revisit the very peculiar thermo-elastic behavior signaled by Warrick[1] . Indeed, a continuous drop in stress with decreasing temperature is normally expected for a non-crystallizing elastomer due to the entropic origin of the retractive force. This effect is partially offset at lower extension by the sample thermal contraction and the elongation at which both effects counter-balance corresponds to the so-called stress inversion. In some elastomers like cis-polyisoprene or polychloroprene, an applied strain favors crystallization, and this effect is called "strain-induced crystallization" (SIC). In that case crystallization is associated to an extensive decrease of the stress linked to a partial relaxation of the remaining amorphous phase. The explanation for this effect was first given by Flory in 1947 [2]. Crystallites are assumed to be of the extended type, which means that a chain entering a crystallite does not fold back into it. Such a crystallization process has a highly relaxing effect for the remaining amorphous fraction, similar to a loose rope getting stretched straight in some parts. SIC has been extensively studied experimentally and a nice example is given by the work of Luch and Yeh [3]. A quite opposite effect was observed by Warrick in PDMS rubbers as the measured stress displays a sudden and tremendous stress increase at some temperature during cooling. He attributed this phenomenon to crystallization and more specifically to the crystallites acting as physical cross-links. This chapter essentially aims to clarify this point.

5.2 Experimental section

5.2.1 Materials

Unfilled and filled poly(dimethylsiloxane) elastomeric samples were synthesized from vinyl-terminated PDMS (DMS-V33, M_W=43000) by a hydrosilylation crosslinking reaction as described exhaustively in **Chapter 2**. Only results obtained with modified silica powder as filler are presented here. The sample sheets were cut into either dumbbell or dog-bone shape specimens (presented in **Scheme 5.1**).

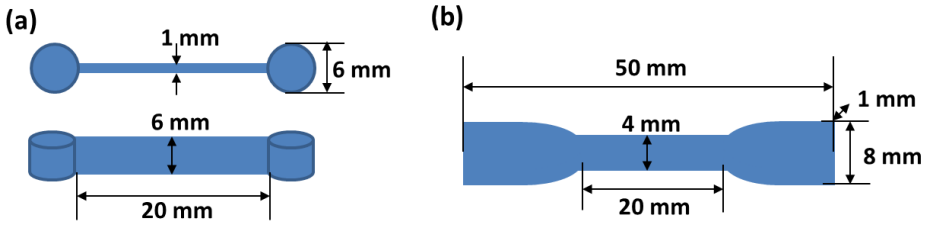

Scheme 5.1 The dimension of two kinds of tested specimen: (a) dumbbell and (b)dog-bone shape

5.2.2 Tensile WAXS measurements

The in-situ tensile machine used in **Chapter 3** does not allow reaching temperatures below -10 ℃ in normal operation mode and some adaptation had to be made. It was first decided to cool the sample by blowing cold nitrogen evaporated from a Dewar. It has the advantage that the gas is perfectly free of moisture which limits frost deposition. Blowing the gas directly onto the sample would not only result in a rather non-homogeneous cooling but also in too very rapid warming once the gas injection is stopped. To circumvent these problems, it was decided to enclose the sample into a copper tube equipped with a removable part for access and to blow gas on the outer surface of the tube (see **Figure 5.1-B**). The tube thickness is 5 mm to favor a good repartition of the temperature and limit gradients inside the tube. (see **Figure 5.1-B**).

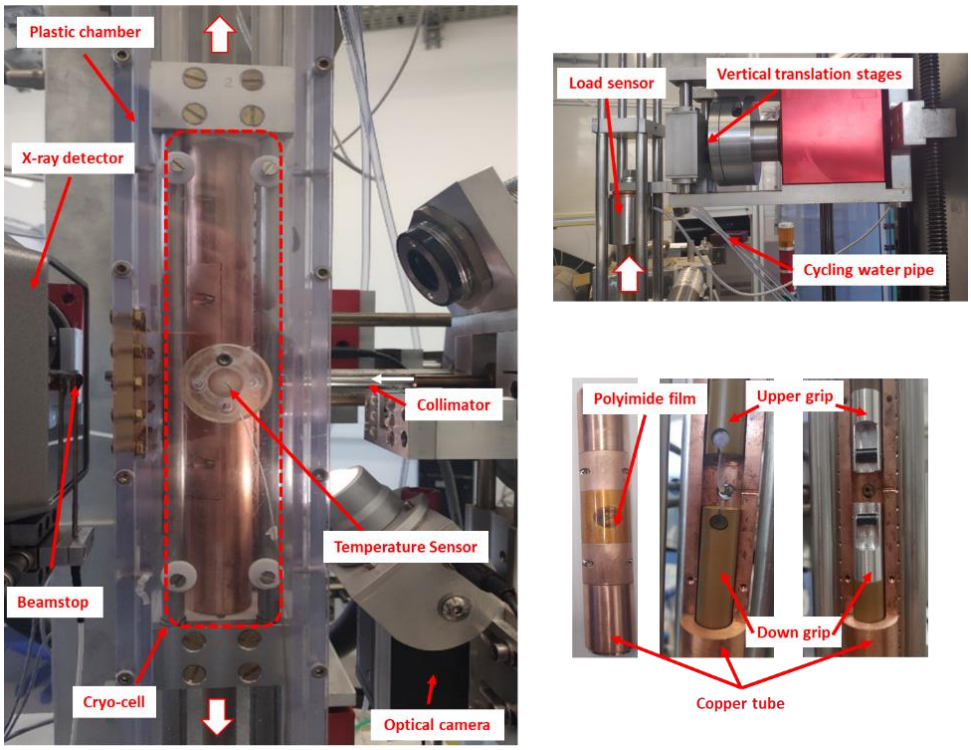

-A- **-B-**

Figure 5.1 The low temperature tensile WAXS test machine: -A- the general view; -B- the prsentation of load sensor (upper picture) and the two kinds of used sample holder within the copper tube (down picture).

The copper tube is hold in position by the upper and lower parts seen with four holding screws (**Figure 5.1-A**). When the polycarbonate housing ("plastic chamber") is put in place the volume containing the tube becomes isolated from the outside. Holes are drilled into the polycarbonate enclosure for the entry of the gas pipes. The cold nitrogen is blown directly on the copper tube external surface: in a first try, the gas was only injected at the central part of the tube and we measured the temperature at three points within the tube: upper part, middle and lower part.

We see in **Figure 5.2** that a temperature difference of ca. 17 ℃ between the tube extremities can be measured in the temperature interval -10 ℃ and -100 ℃; this essentially occurs during the more rapid cooling sequence. When injection is stopped the tube warms up more slowly (see below) and temperature differences are diminished by a factor ca.2. These results were dimmed not satisfying and it was decided to blow the gas both on the upper and lower parts of the tube. Temperature differences during the more critical cooling are reduced to ca. 4 ℃ between -10 ℃ and -100 ℃. This was estimated sufficient keeping in mind that the c is measured along the whole tube length while the sample is essentially located into the central part of the tube.

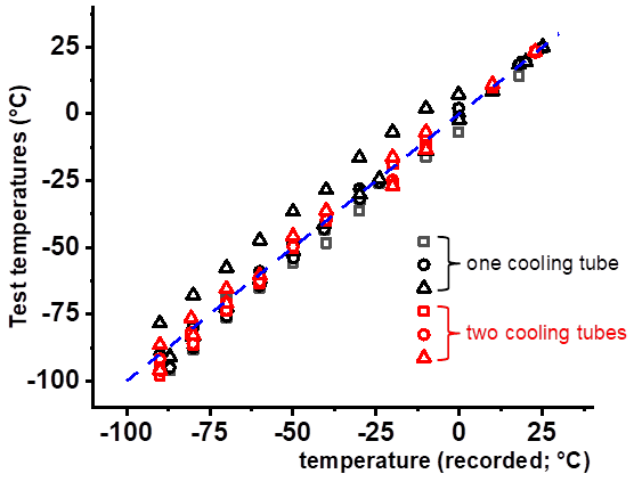

Figure 5.2 Temperatures measured at the tube extremities (squares and triangles) and in the central part (circles) for the two modes of cold gas injection.

The force sensor is located outside the tube enclosure so as to limit the effect of cooling on it. The sensor is actually compensated in temperature between -10 ℃ and 45 ℃ which means that the zero and the sensitivity do not significantly change in this range. However, this only holds once the sensor is perfectly thermalized. Any temperature gradient within the sensor results in a drift of the zero. To limit this effect, the sensor is linked to the sample by a Torlon bar (that appears in beige in **Figure 5.1-**

B). Torlon is a technical plastic that combines high mechanical strength and low thermal conductivity, so that cold transmission is minimized. We see in **Figure 5.3** that marked drifts of the zero are observed if the sensor is not protected (the full range of the sensor is 30daN): it comes from some cold air that manages to escape from the plastic enclosure. It was thus decided to cap the sensor with a water thermalized box. It is clear that drifts are diminished by a factor almost 2 which is sufficient for our observations.

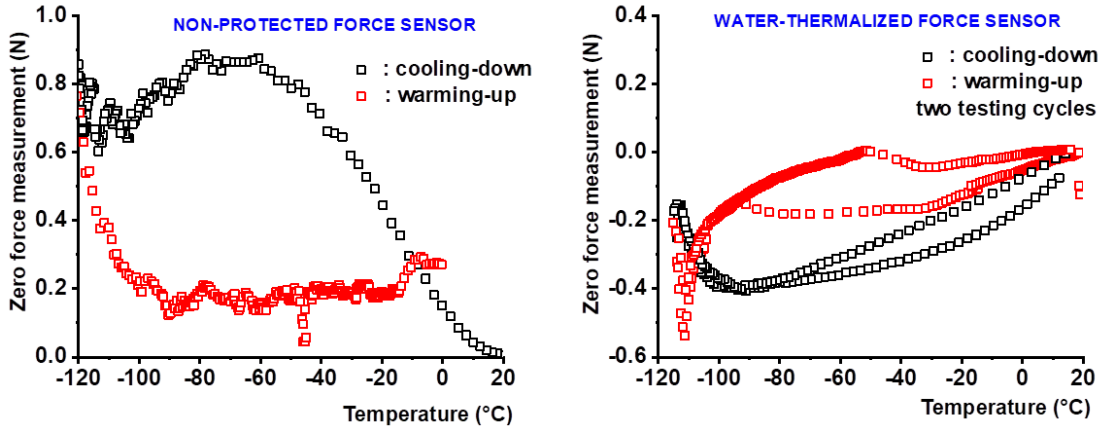

-A- **-B-**

Figure 5.3 Drift of the sensor in absence of any loading during a cooling cycle.

Another challenge is holding the samples without slippage. Grips adapted to dumbbell shaped samples normally prevent slippage. However due to viscosity issues not all the samples could be manufactured into this shape; furthermore, this type of samples often presented defects (inhomogeneity, bubbles) that rendered their use problematic. For this reason, we also used dog bone or rectangular samples that were hold by self-tightening grips (**Figure 5.1-B**, right). In that case some slippage was possible (see below).

Nitrogen is evaporated from the Dewar by means of a heating resistor and the evaporation rate is selected by changing the power dissipated into the resistor. A low evaporation rate leads to large cooling times with the risk of extensive frost formation. On the other hand, a very rapid cooling may result in an incomplete crystallization and excessive temperature gradients. We see in **Figure 5.4** that the chosen cooling rate is ca. 5 ℃/min, close to the one used in our DSC measurements (see **Chapter 6**). When the tube is let to warm-up after evaporation is stopped, the warming rate is ca. half this value.

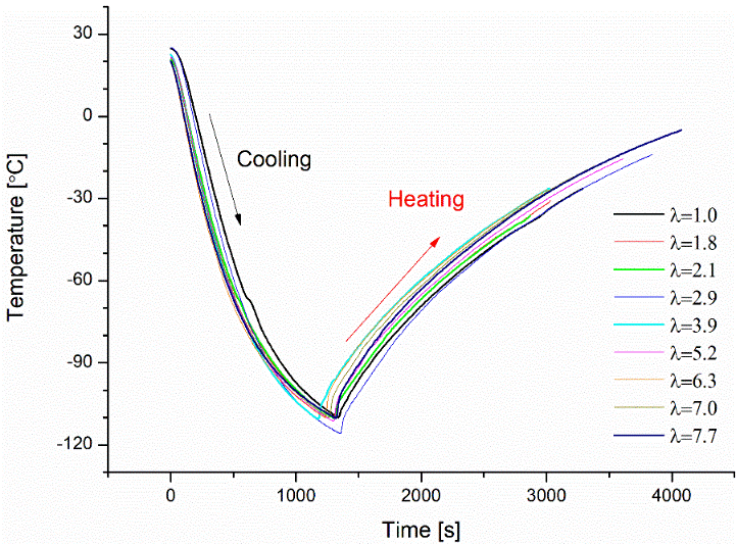

Figure 5.4 The cooling/heating rate inside the copper tube with regard to different WAXS measurements under deformation.

The diffraction patterns are sequentially recorded with a Pilatus 200K detector: the exposure time is 10s and the transfer time for the data is about 0.3s. The transmitted beam intensity and the force are also simultaneously measured. The main problem for the evaluation of the crystallinity came from frost deposition and condensation of water droplets: see examples in **Figure 5.5**. Scattering by tiny ice crystals deposited onto the inner tube window (kapton) is localized in predictable angular areas than can be avoided. Water condensation onto the outer kapton window is much more problematic as it happens at random and quite suddenly. It results in the partial shadowing of zones of interest and generally develops during the warming sequence after the whole polycarbonate enclosure had time to cool-down.

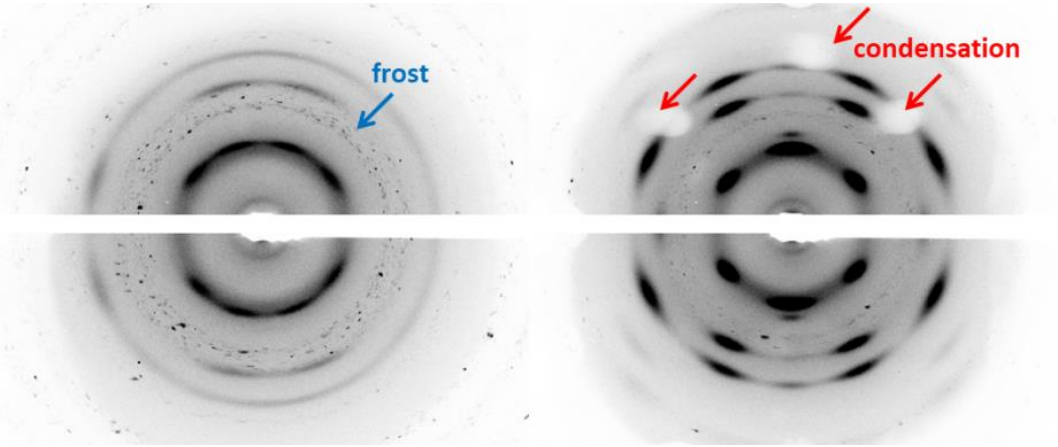

Figure 5.5 illustration of the effect of frost deposition (left) and water condensation (right) on the WAXD patterns.

We have to differentiate between the notion of crystallinity and crystallinity index. The crystallinity is the fraction of crystalline phase in the material. Its evaluation is not easy as it normally requires covering a very large angular scattering range. Furthermore, sophisticated corrections are needed. A crystallinity index is indicative for the relative variation of the crystalline content: it may reduce to the measure of the variation in intensity of a single diffraction ring or part of it. A crystallinity index that allows follow the general crystallization behavior is sufficient in the present case: according to the circumstances (where condensation appears) we used either radial scans on unaffected lines or linear scans to avoid the shadow of water droplets. Averages were systematically performed between the different types of scans performed on the same set of data.

5.3 Results and discussion

5.3.1 Structural evolution during the cooling-heating process

We first give in **Figure 5.6** results obtained with an unfilled and a slightly filled sample in the quiescent state. The evolution of the tensile force appears in red and the crystallinity index is in blue. In both cases crystallization starts at ca. -70 ℃ but the engineering stress only increases below -80 ℃ when the crystallization process is almost completed. As shown above temperature gradients inside the tube are not sufficient to explain this difference; this is inasmuch true that samples in the quiescent state are located in the central part of the tube and large temperature gradients are not expected.

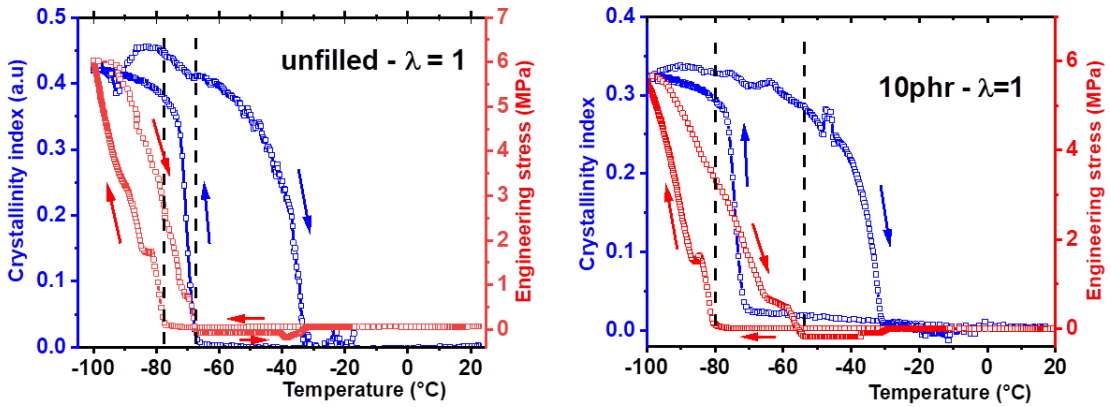

Figure 5.6 Variation of the crystallinity index and engineering stress during a temperature scan for samples in the quiescent state.

The tensile force starts to decrease as soon as the temperature change is reversed; it reaches a close-to-zero level at temperatures where the crystallinity index is still close to its maximum. It is to notice that complete melting is accompanied by a very slight stress increase that returns to its original value. We now turn to the case of samples submitted to a static extension. Representative examples are given in **Figure 5.7**.

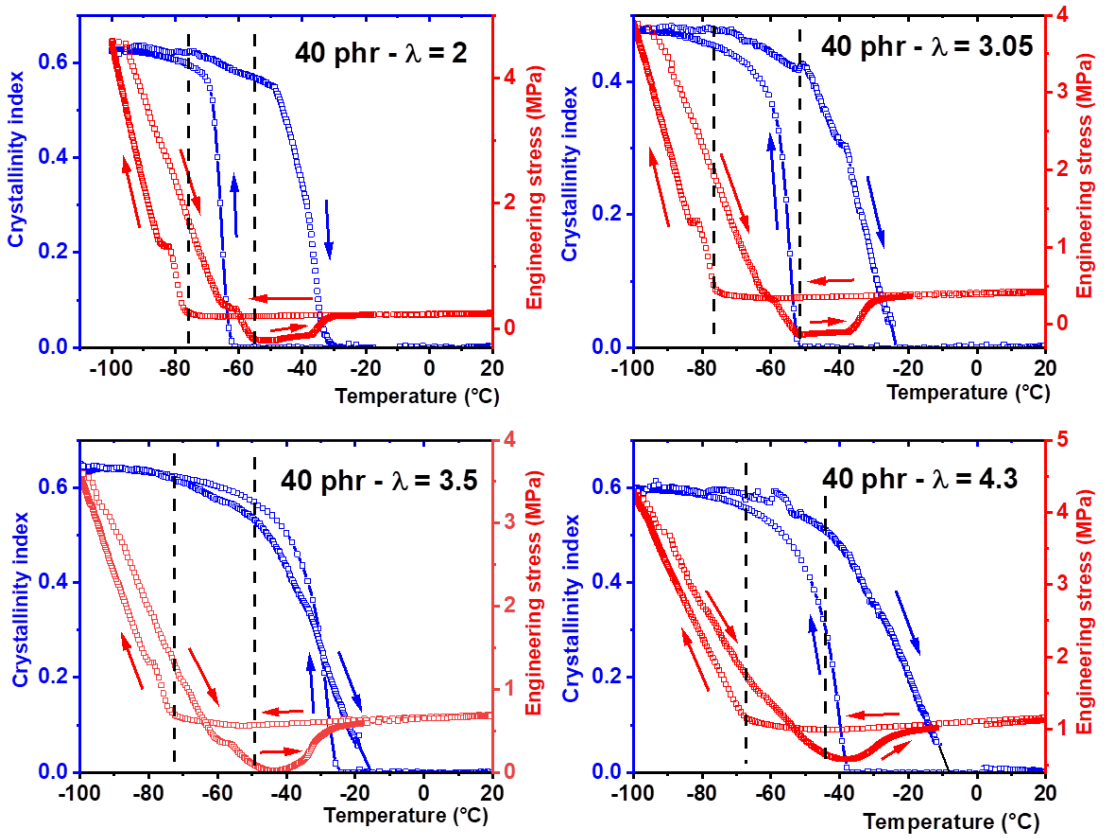

Figure 5.7 Variation of the crystallinity index and engineering stress during a temperature scan for a sample subjected to various static draw ratios. Filler content: 40phr

Whereas crystallization onset during cool-down is observed at ca.-70 ℃ in the quiescent state, we see it occurs systematically at higher temperature in presence on an applied strain. Another example is given in **Figure 5.8** for a sample containing a different amount of filler: it compares with what is observed in **Figure 5.7** for a quite similar draw ratio (3.05) in terms of stress levels. However, crystallinity indices are rather different which is not surprising as they are based on different evaluation methods due to the condensation issue: this precludes any thorough comparison of data and could be only compensated by the development of a specific apparatus including some vacuum isolation. The crystallization temperature has a net tendency to increase with increasing draw ratio, but it is recalled that this parameter is highly dependent upon

the cooling speed. Its variability can explain the fact that crystallization occurs at a higher temperature for λ=3.5 compared to λ=4.3. In all cases, the stress upturn is observed between -80 ℃ and -70 ℃, and occurs when the crystallization process is almost completed.

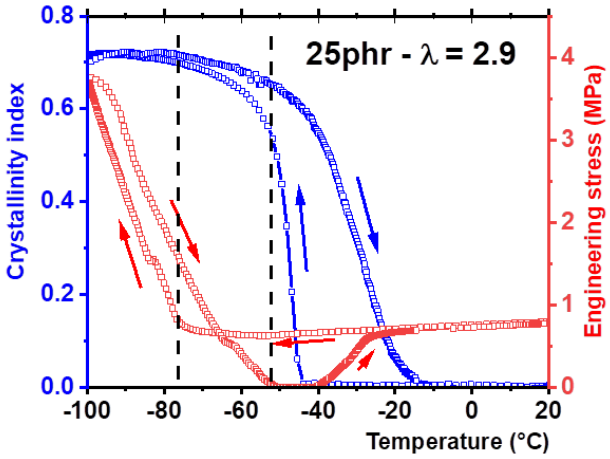

Figure 5.8 Variation of the crystallinity index and engineering stress during a temperature scan for a sample subjected to a static strain. Filler content: 25phr

Stress starts to decrease as soon as cooling is stopped and goes down below the initial stress value before extensive melting is started as observed in the quiescent state. The stress minimum is observed at a temperature close to -50 ℃ independent of the applied strain. Stress levels close to zero are reached which indicates that crystallization has induced some stress relaxation and this is an indication for some strain-induced crystallization (SIC) in PDMS elastomers; upon further warming, stress goes back to initial levels as soon as total melting is observed. The melting temperature steadily increases with applied extension as shown in **Figure 5.9**.

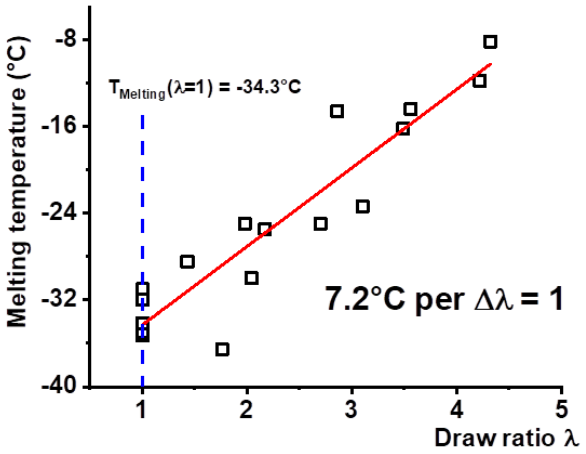

Figure 5.9 The influence of the preset draw ratio λ on the onset crystallization temperature (T_c^{onset}) and the offset melting temperature (T_m^{offset}).

We observe an increase of 7 ℃ per extension increment to compare with 22 ℃ observed in natural rubber that is considered as a model compound for SIC. Another salient feature is the existence of kinks or plateaus in the stress curves both during cooling and warming, without correspondence in the crystallinity index: see **Figures 5.7** and **5.8**. A good example is also provided by the series displayed in **Figure 5.10** for different filler contents and filling procedures. A possible explanation could be some slippage of the sample from the grips. However, one sees no reason why slippage should occur at a much lower stress level during warming compared to cooling. We have no satisfying explanation for this effect.

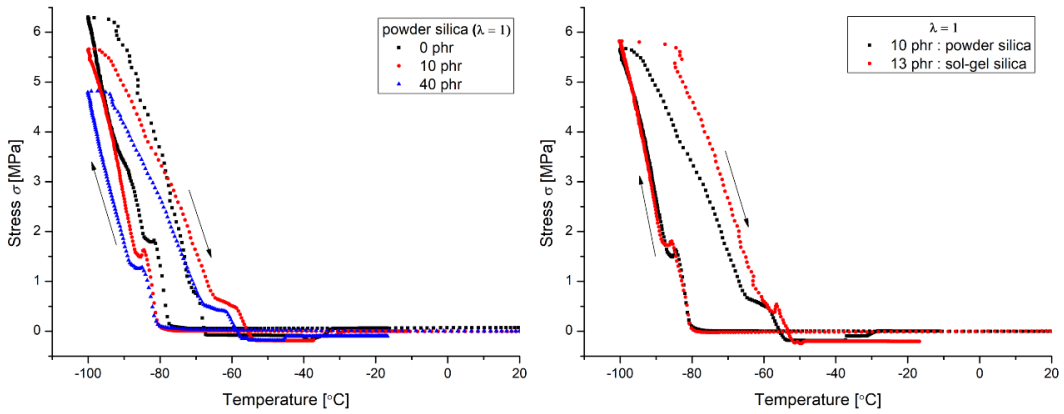

-A- **-B-**

Figure 5.10 The thermoelastic properties of unstretched dog bone shape during cooling and heating: -A- different powder silica content; -B- different mixing method of silica.

5.3.2 Evaluation of the elastic modulus in the crystalline phase

The origin of the stress increase is now discussed. We notice that the stress upturn only occurs after crystallization is almost completed: it is clearly not related to the apparition of the crystallization itself. We believe it is simply due to the combination of the thermal contraction due to cooling and to the modulus increase due to the extensive presence of crystalline phase. We reported in Chapter 1 the work by *Bosq et al* that measured the thermal variation of the PDMS modulus by DMA [6]: see **Figure 5.11**. This increase linked to the increase in crystalline phase content may be attributed to two effects: (i) the inclusion of a hard phase (the crystallites) (ii) the formation of a harder amorphous phase located between the crystalline lamellae (the so-called "constrained amorphous phase"). Indeed, it is our personal experience that diffraction by the remaining amorphous fraction appears modified by the presence of crystalline phase: this could be an indication for some structural modification of the amorphous phase.

The thermal contraction (dilatation) ΔL that occurs in the temperature span ΔT where the stress increases (decreases) is computed in **Equation 5.1**; we assume that the linear thermal expansion coefficient α_L is constant which is justified by the fact that the crystalline content is nearly constant:

$$\varepsilon_T = \Delta L/L = \alpha_L \Delta T \tag{5.1}$$

We take $\alpha_L = 2.56 \times 10^{-4}\ ℃^{-1}$ base on a volumetric thermal expansion coefficient (α_V) of $7.68 \times 10^{-4}\ ℃^{-1}$ at room temperature. The stress increase in this temperature range is $\Delta\sigma$ and the Young modulus is:

$$E = \Delta\sigma/\varepsilon_T \tag{5.2}$$

The evaluation was conducted on samples with different filler contents and in the quiescent state; it shows a rather important dispersion in the data and we obtain $814 \pm 150\ MPa$ during cooling and $577 \pm 130\ MPa$. The difference can be due to the fact that initial thermal contraction has some softening effect similar to the Mullins effect. We see that those values are not far from those reported in **Figure 5.11** at similar temperatures.

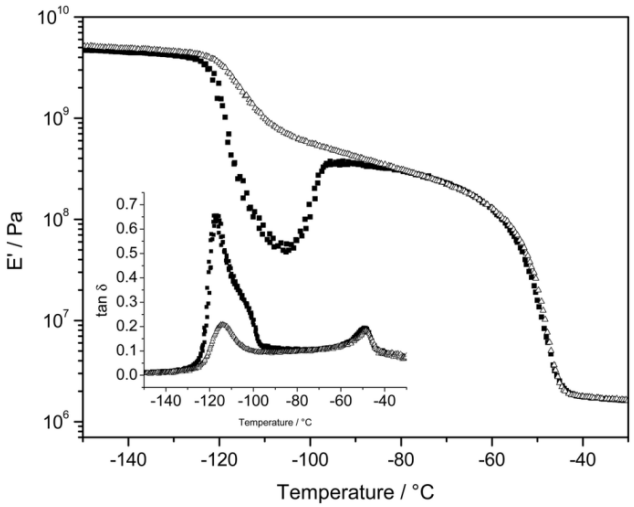

Figure 5.11 Elastic modulus (E′) and tan δ (inset) versus temperature measured on heating an unfilled PDMS elastomer at 1K mn-1. Open triangle: heating after slow cooling from the melt. Solid squares: heating after fast cooling from the melt [22].

5.3.3 "Mesomorphous phase" and crystalline phase

We mentioned in **Chapter 3** the apparition of what Tosaka called a mesomorphous phase when a sample is highly stretched at room temperature [4]. It manifests as strong equatorial intensity reinforcement slightly shifted to higher angles compared to the amorphous halo. The most intense reflection of the high-stretch texture is located at the

same place. This point has been verified during the present study and it is illustrated in **Figure 5.12**: only the mesomorphous phase is visible at -36.7 ℃ and the crystalline phase appears at -37.8 ℃. It clearly demonstrates that both phases are different in nature but that they are related.

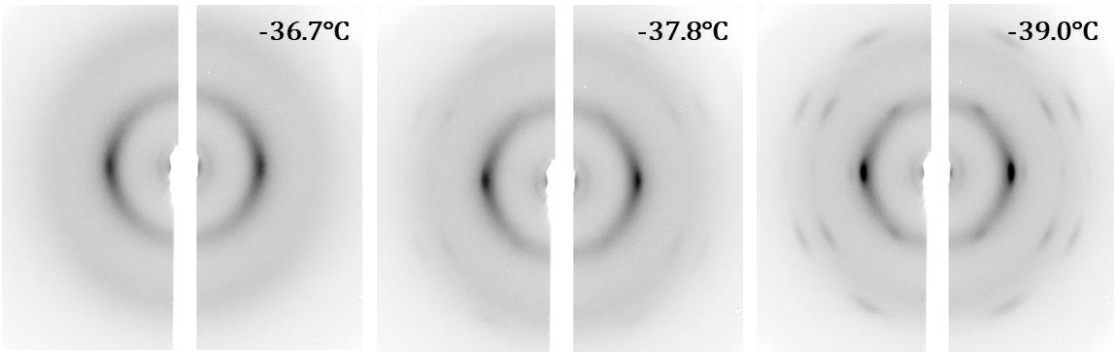

Figure 5.12 The in-situ WAXD patterns of pre-stretched silica-filled PDMS elastomer during cooling.

References

[1] Warrick, E. L. (1958). Crystallinity and orientation in silicone rubber. II. Physical measurements. *Journal of Polymer Science*, 27(115), 19-38.

[2] Flory, P. (1947) Thermodynamics of Crystallization in High Polymers. I. Crystallization induced by Stretching. *J. Chem. Phys.* (15) 397-408.

[3] Luch, D. and Yeh, GSY. (1973). Strain-Induced Crystallization of Natural Rubber. III. Reexamination of Axial-Stress Changes during oriented Crystallization of Natural Rubber Vulcanizates. *J. Polym. Sci. polym. Phys*. (11), 467-486.

[4] Tosaka, M., Noda, M., Ito, K., Senoo, K., Aoyama, K., & Ohta, N. (2013). Strain- and temperature-induced polymorphism of poly (dimethylsiloxane). *Colloid and Polymer Science*, 291(11), 2719-2724.

[5] Trabelsi, S., Albouy, PA & Rault, J. (2003) Crystallization and Melting Process in Vulcanized Stretched Natural Rubber. *Macromolecules* (36), 7624-7639.

[6] Bosq, N., Guigo, N., Persello, J., & Sbirrazzuoli, N. (2014). Melt and glass crystallization of PDMS and PDMS silica nanocomposites. *Physical Chemistry Chemical Physics*, 16(17), 7830-7840.

[7] www.siliconerecycling.com/high-and-low-viscosity-pdms/

Chapter 6

Crystal Structure Determination of Poly (dimethyl siloxane)

Contents

6.1 Introduction

We stressed in **Chapter 1** there is some paradox that the atomic structure of polymer that shows greatest commercial importance in a variety of fields [1], ranging from daily necessities to the industrial and medical applications, is still unknown. Although Damaschun[2] or Albouy[3] respectively proposed a monoclinic crystal structure with two-fold helical conformation and a tetragonal crystal structure with four-fold helical conformation, neither of them gave atomic positions. Similarly, four or crystal polymorphs are sketched in the publications[4] [5] of Tosaka *et al.* without further detail.

In what follows, we try to fill this gap and obtain a full crystal structure based on the analysis of X-ray powder patterns. With the help of annealing simulation, DFT optimization as well as Rietveld refinement, we will propose a crystal structure with detailed atomic information: it will be shown that a basic problem is still to account for the intensity of some diffraction lines. In order to see if the underlying problem was not a misunderstanding of the local crystalline structure (micro-twinning for instance), we also performed some selected area electron diffraction (SAED) at low temperature. This could be only possible due to the help of Alexandre GLOTER from the Electron microscopy team at the LPS.

6.2 Experimental section

6.2.1 Materials

We used silanol-terminated PDMS oils (DMS-S42 and DMS-S21, Gelest Inc.; M_W = 18000 and 4200) for the observation of electron diffraction or powder X-ray diffraction; they were previously vacuum-dried at 120 ℃ for 4 hours.

6.2.2 Differential scanning calorimetry (DSC)

Some DSC measurements were performed to precisely ascertain the two temperatures that are important for this study: the glass transition temperature (T_g) and the melting temperature (T_m): cooling the sample below T_g will not result in an increase in crystallinity; furthermore the rigidity of the amorphous phase may constraint the crystallites and induces some peak broadening. Furthermore, we wanted to improve the crystalline and the crystallite perfection performing some annealing below T_m. The crystallization temperature (T_c) is dependent upon the cooling rate and it is thus only

an indicative parameter. Oils with three different molecular weights were tested with a Q1000 TMDSC from TA Instruments. The cooling rate is fixed at 10 ℃/min and the heating rate at 2 ℃/min. Temperature ranges from room temperature to -160 ℃. We thank Sandrine PENSEC from the Polymer Chemistry Team at the IPCM for all her assistance.

6.2.3 Transmission electron microscopy (TEM)

Transmission electron microscopy (TEM) experiments were performed using a JEOL 2010 equipped with a high-brightness LaB_6 electron source for HRTEM imaging and electron diffraction; the working voltage is 200 kV. The samples for the TEM observation were prepared as follows: the hydroxyl- or vinyl-terminated PDMS oil was dissolved into hexane to prepare a 0.007 vol% solution. Approximately 8 μL of this dilute PDMS solution was dropped onto the gold-coated carbon film of a TEM grid. After complete evaporation of hexane, the TEM grid was first examined by optical microscopy to ascertain the presence of PDMS oil at the surface. Subsequently, the specimen was put in the electron microscope and cooled at ca. 100K. Lanthanum aluminate ($LaAlO_3$) was used as reference to calibrate the magnification factor. These measurements were done under the supervision of Alexandre GLOTER from the Electron Microscopy team at the LPS.

6.2.4 Powder X-ray diffraction

Most of the powder X-ray diffraction characterization of linear PDMS oil was performed on a commercial Bruker D8 Advance diffractometer (shown in **Figure 6.1**). The setup is working at 40 kV and 40 mA in Bragg-Brentano geometry, with Cu Kα radiation ($\lambda = 0.15418$ nm). The Anton Paar TTK 600 low-temperature chamber affixed to the goniometer allows cooling close to the liquid nitrogen temperature. It is normally equipped with a membrane pump to maintain a primary vacuum. It proved non-sufficient to prevent frost deposition on the substrate on the long term. Diffraction peaks associated to ice formation had thus to be removed from the diffractograms; this was afterwards corrected using a more efficient pump. The specimen is placed in a groove-shaped sample-holder with dimension of 14 mm × 10 mm × 0.8 mm that is directly cooled by liquid nitrogen. The nitrogen consumption is not negligible and the maximum acquisition time was ca. 12 hours, fixed by the nitrogen bottle capacity. A Pt100

temperature sensor is positioned close to the sample for precise temperature measurement. The 2theta scan range was fixed between 6 °and 100 °with a step size of 0.02 ° in continuous mode: the diffracted intensity is continuously recorded by a LynxEye linear detector, which allows a huge gain in intensity compared to a step by step acquisition. Prior launching a data acquisition, the correct position of the sample into the beam is checked with a Z-scan (the sample is moved vertically into the beam at zero angle). This procedure avoids errors in the diffraction line positions due to a sample ill-positioning.

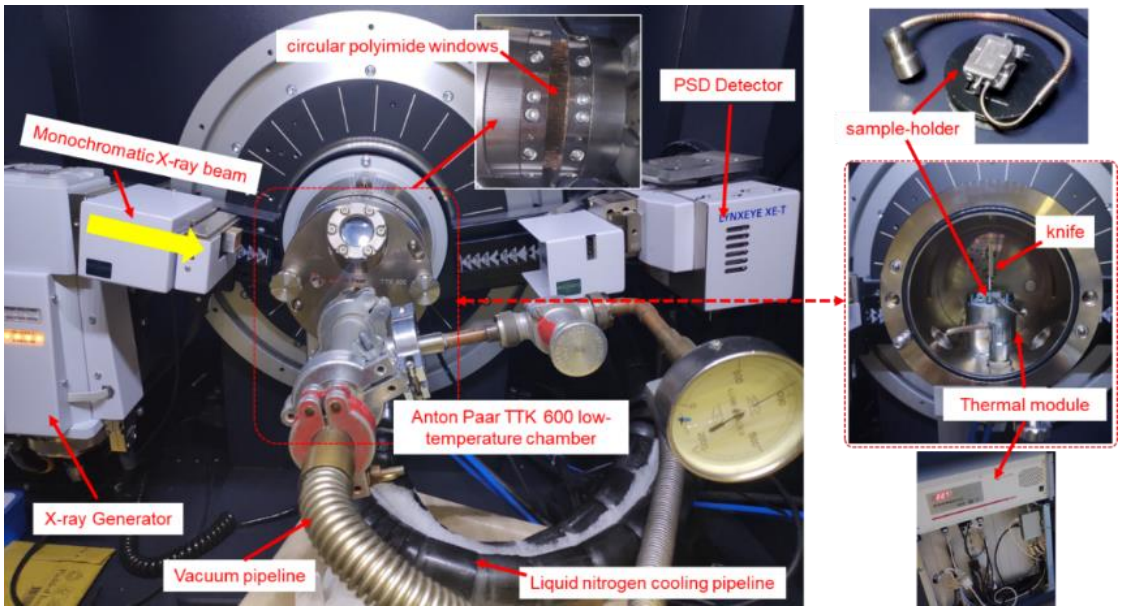

Figure 6.1 General view of the experimental low temperature powder X-ray diffraction instrument.

All measurements were originally to be performed on a high-resolution powder diffractometer working at the wavelength of copper (0.1542 nm) and designed in the Laboratory. The apparatus was only recently ready for operation and only a few measurements could be performed. It operates step by step so that the collected intensity is much lower than with the Bruker. However, it works in parallel beam geometry (parabolic multilayer optic) and it is equipped with a back monochromator that allows removal of Compton scattering and that significantly improves the resolution (parabolic multilayer optics): see **Figure 6.1**. The experimental resolution (ca. 0.03 nm^{-1}) is high enough to permit the separation of some double diffraction lines and the set-up has been essentially used to ascertain the tetragonal unit cell in what follows: no intensity adjustment was performed based on these data.

6.3 Results and discussion

6.3.1 DSC analysis

The first and second cooling/heating scans are displayed in **Figure 6.2** for three different PDMS oils. The data extracted from the second scan are presented in **Table 6.1**. The first and second thermograms are almost identical, especially for vinyl-terminated PDMS, indicating reproducibility and absence of memory effects and hysteresis. Thermal data reported in **Table 6.1** are in good agreement with early published works [6] [7] [8].

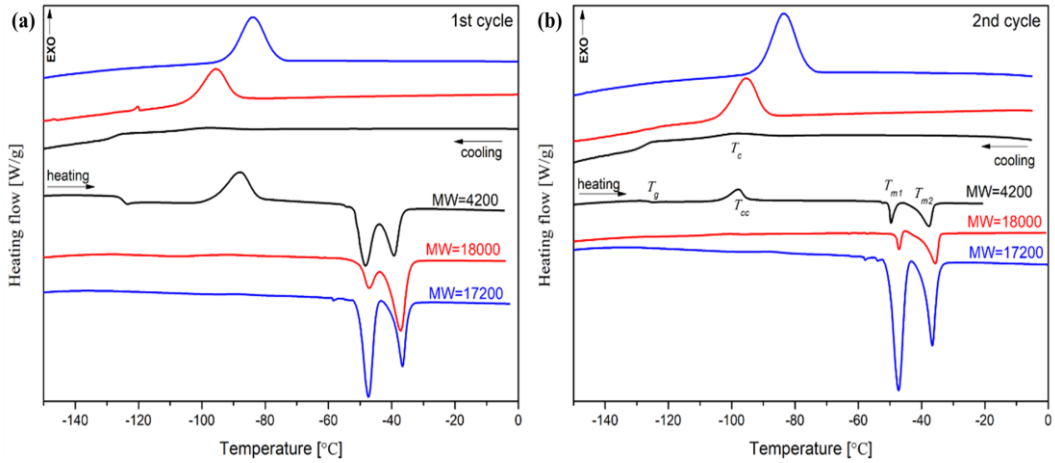

Figure 6.2 DSC traces of (a) first and (b) second cooling/heating scan of silanol-terminated (MW=4200, 18000) and vinyl-terminated PDMS (Mw=17200) oil.

Table 6.1 Thermal data for linear PDMS: crystallization temperature T_c, glass transition temperature T_g, cold crystallization temperature T_{cc} and melting temperature T_{m1} and T_{m2}.

Linear PDMS oil	2nd scan				
	T_c [℃]	T_g [℃]	T_{cc} [℃]	T_{m1} [℃]	T_{m2} [℃]
Silanol-terminated (Mw=4200)	-98.70	-127.33	-97.80	-49.60	-37.52
Silanol-terminated (Mw=18000)	-95.50	*	*	-47.03	-35.58
Vinyl-terminated (Mw=17200)	-83.56	*	*	-47.29	-36.61

* refers to no result showed during the cooling/heating scan.

A major feature is the occurrence of two melting peaks and it is actually commonly observed in PDMS [10] as well as in other polymers [11] [12] [13]. Helmer and Po lmanteer proposed that the two melting peaks correspond to two different types of crystals [14] but further studies did not favor this conclusion and the double melting peaks are now attributed to a melting/recrystallization of smaller or less stable crystallites.

One observes cold crystallization in the M_w=4200 PDMS sample that occurs during warming-up when polymer chains have recovered sufficient mobility to further crystallize. It is not observed in the other samples and the double peaks do not appear specifically linked to this effect. When cooling at an appropriate low rate, the lower melting peak will decrease, even overlap into one peak with the high melting peak, which has been evidenced in previous publications [8] [9] [10] . Moreover, the filler addition and crosslinking in the bulk PDMS can suppress the formation of the higher melting species, thus giving a single melting peak. Annealing at a temperature intermediate between T_{m1} and T_{m2} after first cooling, followed by second cooling is also a way to suppress the lower temperature melting peak. It was systematically performed for the Bruker measurements as it is expected to increase the crystallinity and the crystallite quality.

6.3.2 Selected area electron diffraction (SAED) analysis

In order to exclude doubts about the reliability of the tetragonal crystal structure model, both silanol-terminated PDMS (Mw=4200) and vinyl-terminated PDMS (MW=17200) oils were measured by selected area electron diffraction (SAED). The specimen was first cooled to −110°C and held for 60 min, followed by TEM observation.

A main problem was to find single-crystals on the grid. If we focus on large irregular aggregates with micrometric dimension as displayed in **Figure 6.3a** (the insert TEM image), electron diffraction demonstrates it consists in many small crystallites.

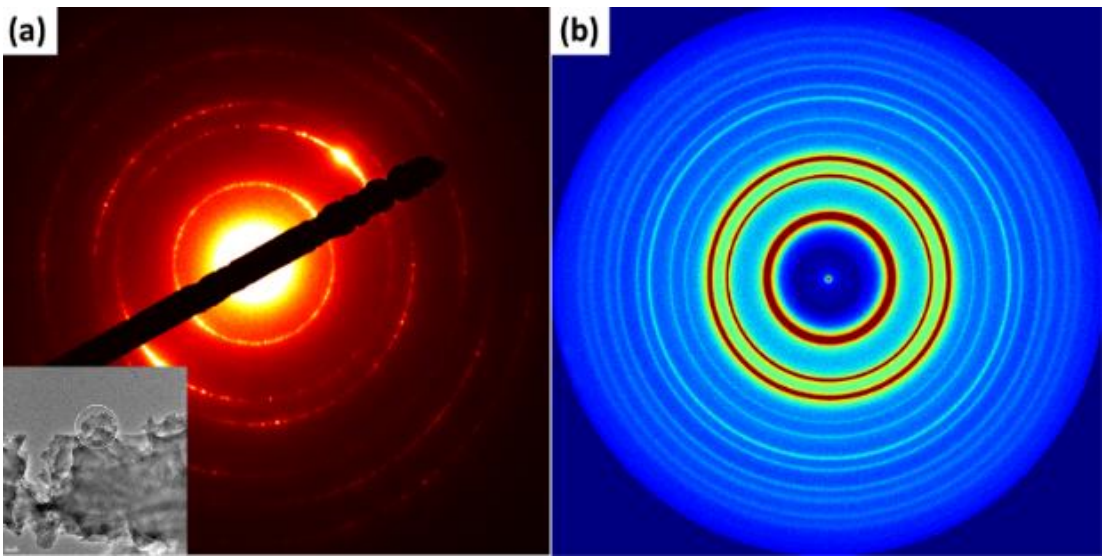

Figure 6.3 (a) the electron diffraction pattern recorded from the selected area (the white cycle) in the inset TEM image and **(b)** the X-ray diffraction pattern of short-chain (Mw=4200) PDMS oil in crystalline state.

The diffraction pattern is indeed very similar to the one obtained by X-ray diffraction (**Figure 6.3b**: Mar345 set-up; wavelength 0.071nm). It confirms we have crystallized PDMS on the TEM grid. Only one aggregate giving rise to well-defined Bragg reflections could be found: it has a rather irregular morphology (see insert in **Figure 6.4**) but it gives rise to well-defined Bragg reflections. The pattern displayed in **Figure 6.4** originates from the thinner zone indicated by a red circle.

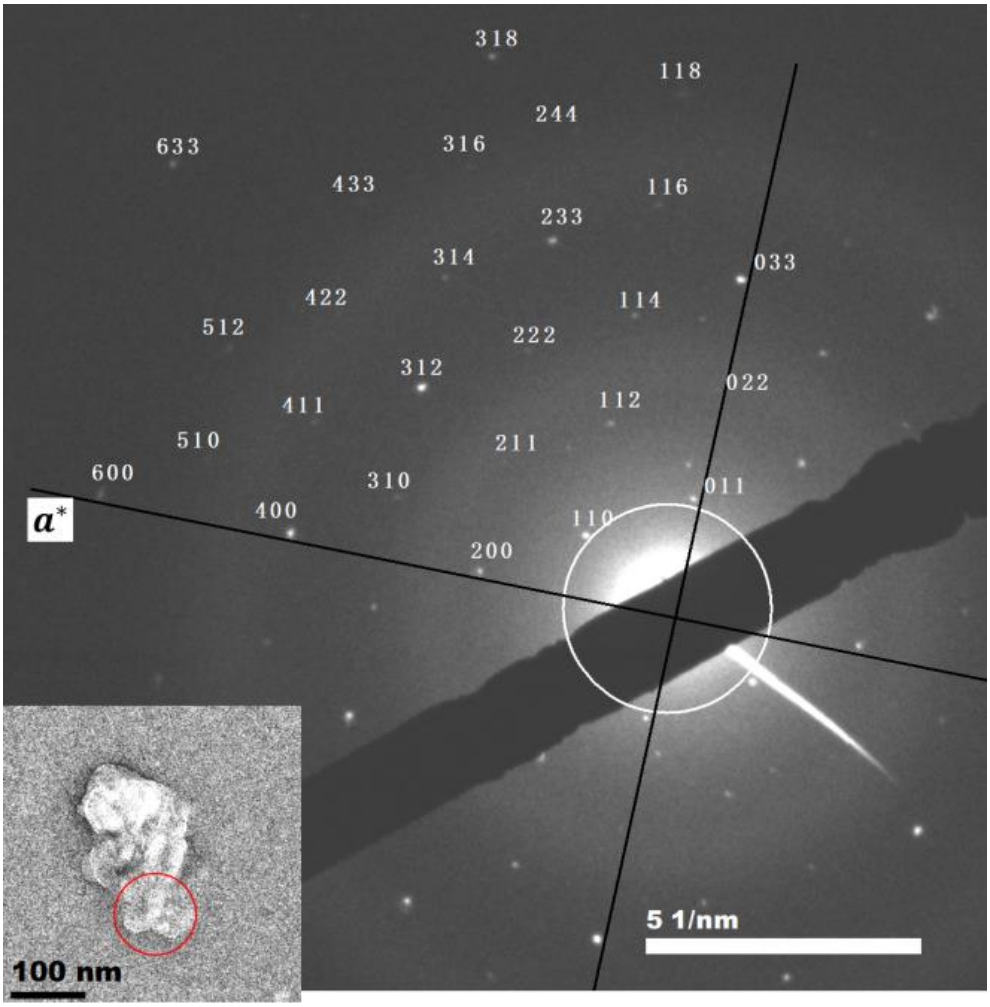

Figure 6.4 the electron diffraction patterns collected from the selected area: (a) red and (b) white cycle in the inset TEM image of the short-chain (MW=4200) PDMS oil in crystalline state.

The indexation given in the figure is based on the tetragonal cell defined by Albouy. Indeed, all four SAED diffraction pictures presented by Tosaka *et al.* [31] and that they associate to four different crystalline forms can be indexed with the only tetragonal cell.

6.3.3 Powder X-ray diffraction analysis

We represent in **Figure 6.5** typical diffractograms obtained in the molten state (room temperature) and in the semi-crystalline state (-100 ℃) with the Bruker D8

Advance diffractometer (PDMS oil M_w=18000). It is similar to all our previous observations made on PDMS rubber samples.

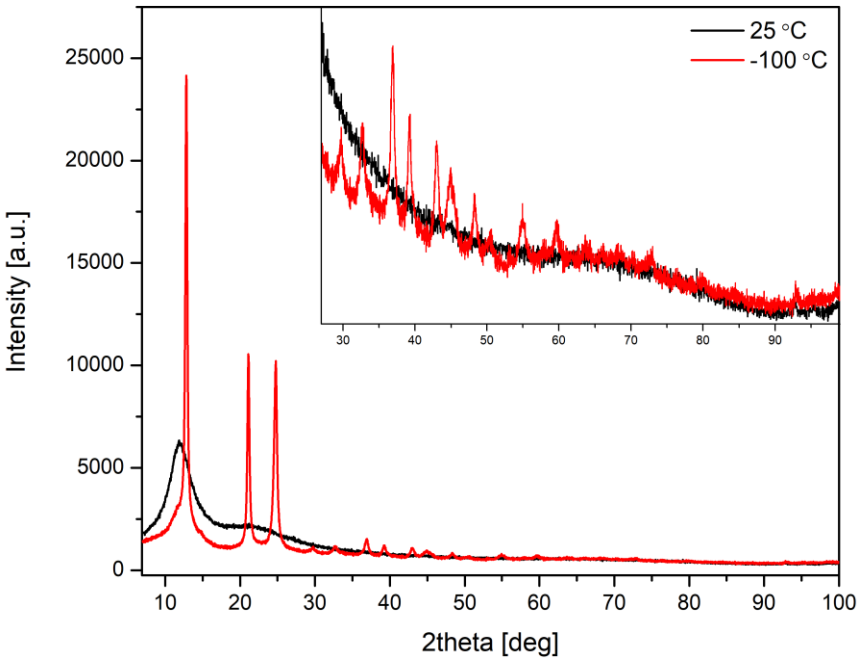

Figure 6.5 X-ray diffraction profile of pristine PDMS oil (M_w=18000) at 20 and -100 ℃

Marked differences in intensity are observed when using a short chain oil (M_W=4200): see **Figure 6.6**.

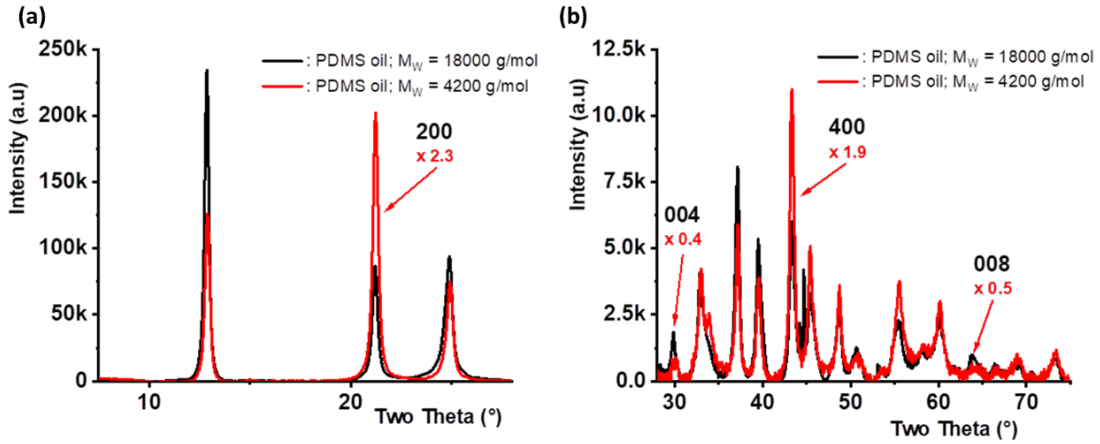

Figure 6.6 The comparison of X-ray diffraction in reflection geometry of pristine PDMS oil at -100 ℃ with regard to different chain length (M_W=18000 and 4200). The background is substrate.

Diffraction patterns obtained with similarly light oil poured into a capillary glass did not exhibit such differences (Albouy, private communication). This effect is thus due to the sample geometry that induces some preferential orientation. The intensity of lines with $l = 0$ is increased while the (004) and (008) lines are decreased by a factor ca. 2. This indicates that the c-axis is preferentially oriented parallel to the oil-air

interface. It is in agreement with the chain axis parallel to the c-axis: in the liquid state chains located close to interface will have a tendency to be parallel to it, which will induce preferential orientation at the crystallization step.

6.4 Theory of crystal structure determination

X-ray crystallography is unique to determine atomic positions within the crystal (although NMR can also bring some information). We briefly recall that the diffracted amplitude (i.e. amplitude of the electric field) scattered by any sample is the Fourier transform of its electronic density. In case of a single-crystal the electronic density presents a 3D repetition in the direct space and amplitude is scattered only in discrete directions. These directions are characterized by scattering vectors $\vec{q}_{hkl}$ that present 3D periodicity in the so-called reciprocal space: $\vec{q}_{hkl} = h\vec{a}^* + k\vec{b}^* + l\vec{c}^*$. When the sample is polycrystalline, these directions coalesce into diffraction cones. Each amplitude F_{hkl} is one component of the Fourier transform of the electron density. If amplitudes, including their phase could be measured, the crystal structure would be simply obtained by inverse Fourier transform. However, detectors are only sensitive to the flux of energy carried by an electromagnetic wave that is proportional to the square of the electric field. It means that $|F_{hkl}|^2$ and hence $|F_{hkl}|$ are measured, and not F_{hkl}: this is the well-known "phase problem". Crystal structure determination is so fundamental in fields like crystal chemistry, solid state physics, and the biological sciences that many methods have been devised to solve it.

6.4.1 Line profile analysis

In a crystal powder samples, the diffracted intensity merges into cones of diffraction characterized by their angular apertures 2θ that are related to the unit cell parameters $(a, b, c, \alpha, \beta, \gamma)$ in the direct space by the Bragg's law. Various instrumental and specimen features may affect the observed positions of Bragg peaks. These factors are often known as systematic aberrations (distortions). In terms of the shapes of diffraction peaks, the so-called peak-shape function (PSF) is a convolution ($\otimes$) of three different functions: instrumental broadening (Ω), wavelength dispersion (Λ), and specimen function (Ψ), which is expressed as:

$$\mathrm{PSF}(\theta) = \Omega(\theta) \otimes \Lambda(\theta) \otimes \Psi(\theta) + b(\theta) \qquad (6.1)$$

where $\boldsymbol{b}$ is the background function.

On the other hand, the arrangement of the atoms within the unit cell determines the relative intensities of the reflections: these are the structure factors $|F_{hkl}|^2$. More specifically, other factors like specimen factors (owing to its shape and size, preferred orientation, grain size and distribution, microstructure and other parameters of the sample) and instrumental factors (such as properties of radiation, type of focusing geometry, properties of the detector, slit and/or monochromator geometry) play roles in determining peak intensities.

6.4.2 Unit cell determination

The first step in solving a crystal structure based on powder diffraction is to find the unit cell that allows an hkl indexation of all observed diffraction lines. The angular line positions relate to the d-spacings by the Bragg's law and the relation of d_{hkl} to the indices hkl and the unit cell parameters is known:

$$d_{hkl} = f(h, k, l, a, b, c, \alpha, \beta, \gamma) \tag{6.2}$$

Through peak searching, all possible reflections could be located at $\boldsymbol{d^{obs}}$ $\boldsymbol{(2\theta^{obs})}$. For any given assumed unit cell dimensions, the combination of symmetrically independent triplet (hkl) is assigned to the observed Bragg peak by matching $\boldsymbol{d_{hkl}^{calc}}$ $\boldsymbol{(2\theta_{hkl}^{calc})}$ and $\boldsymbol{d^{obs}}$ $\boldsymbol{(2\theta^{obs})}$ based on the minimum difference between the pairs of values. To evaluate the reliability of indexing, figures of merit (M_{20}[15] or F_N [16]) are introduced. Generally, the more reliable indexing yields the higher F_N or M_{20}, and both are useful when comparing different indexing solutions for the same pattern.

As for indexing powder XRD data, there are different strategies available which are incorporated into the widely used programs ITO[17], TREOR[18], DICVOL[19], CRYSFIRE[20], and McMaille[21] [22] [23] [24]. They consider the measured positions of peak maxima for about 20 selected peaks at low diffraction angles. The existence of significant peak overlap can be particularly problematic in the indexing stage, as certain peaks that may be vital for correct indexing may be obscured or completely unresolved due to peak overlap. In this regard, successful indexing of powder XRD data of a substance can sometimes be particularly challenging. Therefore, experimental operating condition should be noticed when aiming to collecting quality powder diffraction data.

6.4.3 Profile fitting

After the unit cell has been determined, the next stage is to prepare the intensity data for space group determination and structure solution using an appropriate profile fitting technique such as the such as the Pawley method[25] or the Le Bail method[26] . The aim of this stage is not to determine the crystal structure, but rather to obtain reliable values of the variables that describe different features of the powder XRD profile by completely fitting, which are useful in the Rietveld refinement stage for the structure determination process. The variables include: (**i**) The peak positions (the variables that determine the peak positions include the unit cell parameters and the zero-point shift parameter); (**ii**) The background intensity distribution; (**iii**) The peak widths; (**iv**) The peak shapes; (**v**) The peak intensities.

It is important to emphasize that no structural model is used in the profile fitting procedure (except in so far as the unit cell parameters are used to determine the peak positions), and the intensities in (**v**) represent a set of intensity variables that are refined to give an optimal fit to the experimental powder XRD pattern without reference to any structural model.

6.4.4 Structure solution

Techniques for structure solution from powder XRD data can be subdivided mainly into two categories: the traditional and direct-space approaches. The traditional approaches can be divided into two broad categories: those based on reciprocal-space methods and those based on real-space methods. Typically, the former (direct methods[27]) involve direct use of the measured reciprocal space data, i.e. the $|\mathbf{F}|^2$ values, while the latter (Patterson methods[28]) are concerned with the position and conformation of the molecules (or individual atoms/ions) within the unit cell. Both methods follow a close analogy to the analysis of single-crystal XRD data, in that the intensities $I(q)$ of individual reflections are extracted directly from the powder XRD pattern and are then used in the types of structure solution calculation. However, peak overlap in the powder XRD pattern can limit the reliability of the extracted intensities, and uncertainties in the intensities can lead to difficulties in subsequent attempts to solve the structure.

In contrast to the traditional approach, the direct-space approach[29] follows a close analogy to global optimization procedures. In the direct-space strategy, trial

crystal structures are generated in real space, independently of the experimental powder XRD data, and the suitability of each trial structure is assessed by direct comparison between the calculated powder XRD pattern and the experimental powder XRD pattern. In this case, the corresponding comparison result is quantified using an appropriate figure-of-merit, the weighted profile *R*-factor R_{wp}, defined as:

$$R_{wp} = 100\sqrt{\frac{\sum_i w_i(y_i - y_{ci})^2}{\sum_i w_i y_i^2}} \tag{6.3}$$

where y_i is the intensity of the *i*-th point in the digitized experimental powder XRD pattern, y_{ci} is the intensity of the *i*-th point in the calculated powder XRD pattern and w_i is a weighting factor for the *i*-th point.

Without further manipulation of individual peak intensities measured, the R-factor also considers the peak overlap implicitly because the direct-space approach compares the calculated and measured intensity point-by-point, rather than focusing on some individual diffraction maxima. The aim of the direct-space strategy is to find the trial crystal structure that corresponds to lowest *R*-factor, and is equivalent to exploring a hypersurface $R(\Gamma)$ to find the global minimum, where Γ represents the set of variables that define the structure. Techniques for global optimization, including Monte Carlo/simulated annealing[30] [31] and genetic algorithm[32] [33] [34] [35], have proved effective in finding the lowest point on this $R(\Gamma)$ hypersurface.

6.4.5 Structure rietveld refinement (Final crystal structure model)

In so-called Rietveld refinement[36] [37] [38], the variables that define the powder XRD profile (i.e. the variables (i)-(iv) obtained by profile fitting stage) and the variables defining the structural model (which are used to determine the relative peak intensities in the calculated powder XRD pattern) are adjusted by least squares methods in order to obtain an optimal fit between the experimental and calculated powder XRD patterns. In general, the weighted profile R-factor (R_{wp}) is used to assess the quality of fit.

6.4.6 Overview of the structure determination process

We illustrate in **Figure 6.8** the main stages of the structure determination from diffraction data: Structure solution aims to derive an approximately correct description of the structure, using the unit cell and space group determined in the first stage, but

starting from no knowledge of the actual arrangement of atoms or molecules in the unit cell. If the structure solution represents a sufficiently good approximation to the true structure, a good quality description of the structure can then be obtained by structure refinement.

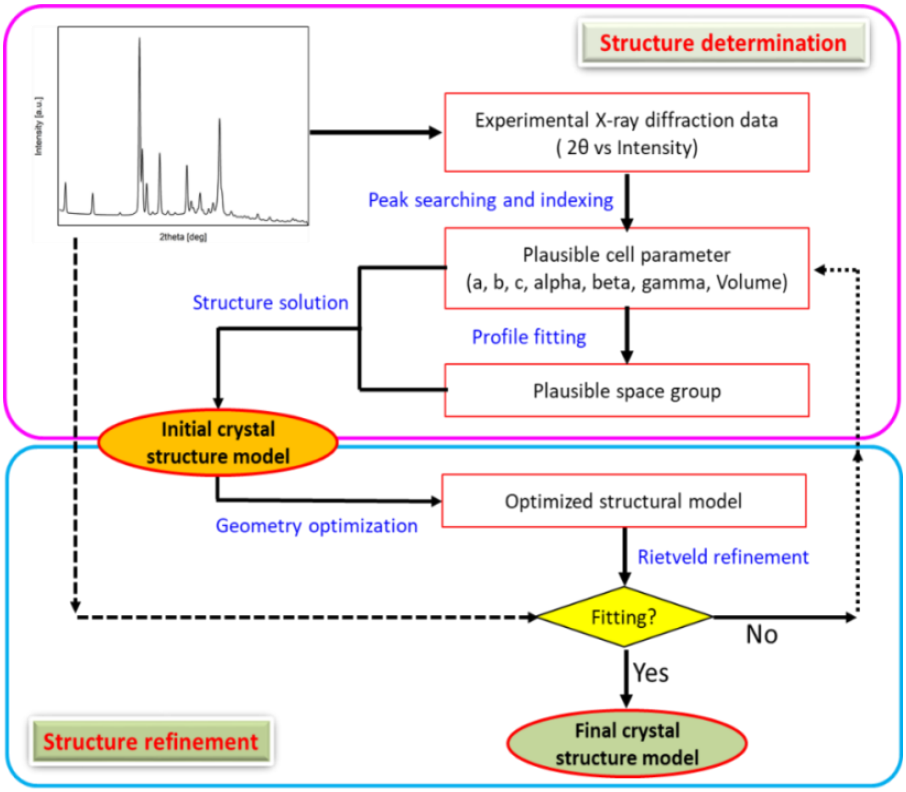

Figure 6.8 Schematic diagram showing the sequence of stages involved in crystal structure determination from powder XRD data.

Using the program of FullProf suite [39] , we first indexed 14 intense peaks of a diffractogram measured at -100 ℃ (170K) by the TREOR-09 method (the whole pattern is then fitted introducing shape and width parameters): see **Figure 6.9**.

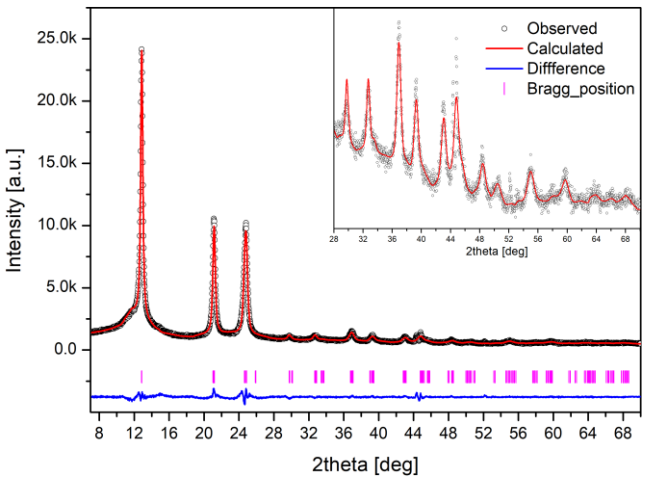

Figure 6.9 Profile fitting.

We found a tetragonal unit cell with parameters of $\boldsymbol{a} = \boldsymbol{b} = \mathbf{8.\ 3972}$ **Å** and $\boldsymbol{c} = \mathbf{11.9773}$ **Å** (170K) which agree very well with the previous result of X-ray and electron diffraction pattern analysis. The ratio c/a is 1.431, close to $\sqrt{\mathbf{2}}$. If this ratio was $\sqrt{\mathbf{2}}$, lines of indices 103 and 121 that constitute the third most intense diffraction line should be perfectly superimposed. This cannot be judged from **Figure 6.9** as the resolution of the Bruker diffractometer is not sufficient. Some additional measurements have been performed with the home-made high-resolution diffractometer recently constructed in the group MATRIX (wavelength 0.1542 nm). We see in **Figure 6.10** that the two lines are actually separated. Parameters determined with this apparatus are $\boldsymbol{a} = \boldsymbol{b} = \mathbf{8.\ 405}$ **Å** and $\boldsymbol{c} = \mathbf{12.041}$ **Å** at 230K and $\boldsymbol{a} = \boldsymbol{b} = \mathbf{8.\ 272}$ **Å** and $\boldsymbol{c} = \mathbf{11.850}$ **Å** at 110K. The ratio c/a is 1.433, very similar to the precedent estimation.

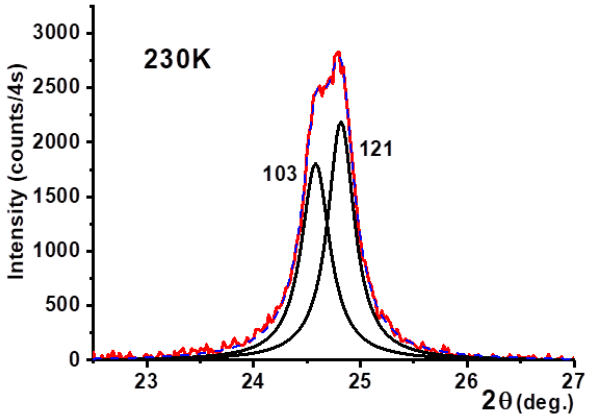

Figure 6.10 High-resolution profile for the third more intense diffraction line.

Subsequently, the symmetry groups were obtained by running the incorporated CheckGroup program, that suggested 49 possible space groups, listed in **Table 6.2**.

Table 6.2 the top 10 of 49 possible space group list

Number(IT)	Hermann-Mauguin Symbol	Merit*
141	$I\ 4_1/a\ m\ d$: 1	2.60
109	$I\ 4_1\ m\ d$	2.44
122	$I\ \bar{4}\ 2\ d$	2.44
88	$I\ 4_1/a$: 1	2.29
98	$I\ 4_1\ 2\ 2$	2.05
80	$I\ 4_1$	2.05
87	$I\ 4/m$	1.95
107	$I\ 4\ m\ m$	1.95
82	$I\ \bar{4}$	1.95
119	$I\ \bar{4}\ m\ 2$	1.95

* The merit (F_N) has been introduced by Smith and Snyder[16], it is defined as:

$$F_N = \frac{N}{N_{poss}} \times \frac{1}{\left|\overline{\Delta 2\theta}\right|} = \frac{N^2}{N_{poss} \sum_{i=1}^{N} \left|2\theta_i^{obs} - 2\theta_i^{calc}\right|} \quad (6.4)$$

where N is the number of the observed Bragg peaks, N_{poss} is the number of independent Bragg reflections possible up to the N-th observed diffraction peak; $\left|\overline{\Delta 2\theta}\right|$ is the average absolute difference between the observed and calculated 2θ.

When considering the 4_1-screw symmetry and the body-centered cell feature, five space groups with highest figure of merit (above 2), including *I* 4_1 (No. 80), *I* 4_1 /*a*:1 (No. 88), *I* 4_1 2 2 (No. 98), *I* 4_1 *m d* (No. 109), *I* 4_1 /*a m d* (No. 141), might be more reasonable.

The unit cell content information, more exactly, the number of monomers per unit cell (*Z*), is vital for the crystal structure determination. Taking into account the structure formula and the cell volume (V_{cell}) which is obtained by the indexation, Z can be estimated as the ratio between V_{cell} and the molecular volume (V_{mol}):

$$\boldsymbol{Z = \frac{V_{cell}}{V_{mol}}} \quad \boldsymbol{(6.5)}$$

Where an evaluation of V_{mol} can be provided by one of the two following ways:

(1) Using the 18 Å^3 rule: counting all the non-hydrogen atoms in the chemical formula and multiplying this number by 18 Å^3;

(2) Using the approximate atomic volumes given by reference [40]: 13.87 Å^3 for C, 11.39 Å^3 for O, 37.30 Å^3 for Si, 5.08 Å^3 for H.

In the case (–SiC_2H_6O–) as original asymmetrical unit and a unit cell volume of 843.76 Å^3, we find a *Z* value of ca. 12 with the first criterion and ca. 8 with the second approach. It corresponds to crystalline phase densities of 1.751 and 1.167 g/cm^3 respectively; the last estimation is very close to the value 1.16 g/cm^3 at 183K proposed by Albouy and based on X-ray absorption data. It can be concluded that there are most probably 8 monomers per unit in the crystalline lattice.

In the case of space group *I* 4_1/*a* (No. 88), *I* 4_1 2 2 (No. 98), *I* 4_1 *m d* (No. 109) or *I* 4_1/*a m d* (No. 141), there should be a total of 16 monomers per unit cell according to the corresponding symmetry operators, with a density of 2.335 g/cm^3 in the normal condition (all atoms having a site occupancy of 1). This is seriously inconsistent with the experimental estimation 1.16 g/cm^3. The space group that conforms to Z=8 and an occupancy of 1 is *I* 4_1 (No. 80). However, it should be noted that and *I* 4_1 /*a* (No. 88) also could be possible if the site occupancy of all atoms was set 0.5 (the other three

were still impossible because of the failure in generating polymer chain conformation inside the cell under this condition).

We first start with the space group $I\,4_1$ (No. 80) and 8 monomers per cell. The cell parameter can be slightly regulated to make the connection between monomers possible and allow for a reasonable chain conformation. We also used use restraints on bond distances and angles or bond valences and this approach increases the probability to obtain only chemically plausible models. They are similarly relationships between atoms to prevent atomic group overlapping with other parts of structure. Space group $I\,4_1/a$ (No. 88) with atom site occupancy of 0.5 has be also selected for further comparison.

6.4.6.1 Annealing simulation

In essence, molecular structure calculation and refinement is a search for the global minimum of a target function of the parameters of an atomic model in particular atomic coordinates.

$$E = E_{chem} + w_{data}E_{data} \tag{6.6}$$

where E_{chem} comprises empirical information about chemical interactions; it is a function of all atomic positions, describing covalent (bond lengths, bond angles, torsion angles, chiral centers, and planarity of aromatic rings) and nonbonded (intramolecular as well as intermolecular and symmetry-related) interactions. E_{data} describes the difference between observed and calculated data, and w_{data} is a weight appropriately chosen to balance the gradients (with respect to atomic parameters) arising from the two terms.

The general least-squares refinement procedure follows a continuously "downhill" path to minimize the objective function. If the starting model is too far away from the correct solution, the refinement may end up in a local minimum rather than global minimum that corresponds to an incorrect structure. As introduced in **Section 6.4.4**, the direct-space approach can make maximal use of information on molecular geometry that is already known reliably, independently of the powder XRD data, prior to commencing the structure solution calculation. The traditional approach for structure solution, on the other hand, does not (in general) utilize prior knowledge of features of molecular geometry.

A most popular direct-space method, called **simulated annealing,** can often enable the refinement to escape from local minima and find the global minimum. Simulated annealing, which is a modified form of a **molecular dynamic simulation**, uses Newton's laws of motion to predict possible movements of the atoms in a trial model of the crystal structure. The molecule is allowed to move as if it were at high temperature, in order to enable it to escape from any local energy minima; initial atomic velocities are assigned randomly from a Maxwell distribution at the appropriate temperature. Then, the molecule is cooled slowly to find its preferred structure at the temperature of the X-ray diffraction experiment. During this process, the assigned energy of the molecule partly depends on agreement with the diffraction data.

In the case of solving PDMS crystal structure, our final aim is to search for the chain conformations of the polymer molecule that best fit the experimental data and that simultaneously maintain reasonable covalent and noncovalent interactions. From our above analysis, one monomer (–$OSiC_2H_6$–) was treated as the starting asymmetric seed to construct the crystal structure, hoping that the best resulting model will most closely resemble the global minimum. More specifically, through the symmetry operation, the unit cell could be filled, these fragments are expected to interact with each other in a reasonable way when considering bond length and bond angle. Finally, the energy is minimized with respect to all the rotational angles and the intra-chain symmetry.

The crystal structure determination was performed by simulated annealing using the program Expo2014 [41] . During the simulated annealing calculations, the cost function was chosen as *R* intensities. As explained above anti-bumping restraints were set to let all monomers connect to each other into polymer chains. Finally, it yields two kinds of chain conformation within the PDMS crystal, depending on the selected space group, illustrated in **Figure 6.11**. The torsion angle (−O−Si−O−Si−) of space group *I* 4_1 (No. 80) is about 160 °, much larger than that of *I* $4_1/a$ (No. 88), which is 100 °, suggesting a more spiral chain configuration in space group of *I* $4_1/a$ (No. 88). We call these two crystal structure models of "extended model" and "helical model" respectively. We put an occupancy of 0.5 for each atom for space group *I* $4_1/a$. We will see that we interpret it as chains running along the c-axis and that can occupy different locations with a probability of 1/2.

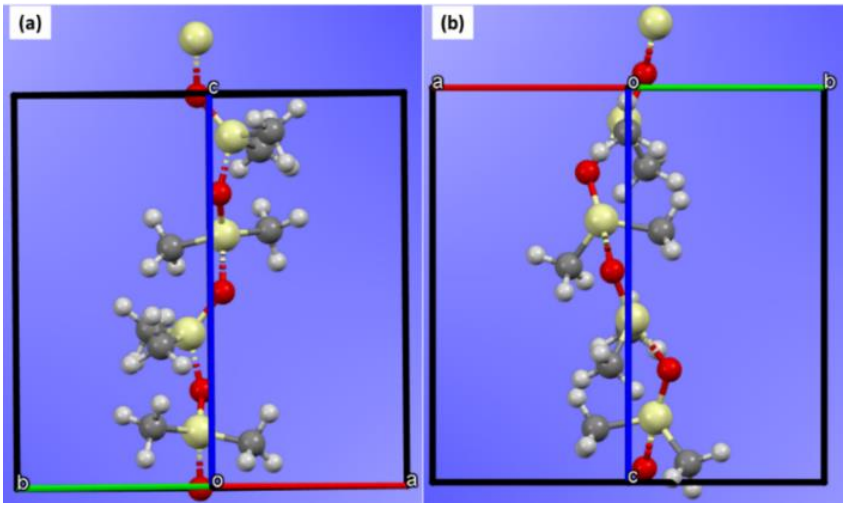

Figure 6.11 The **chain conformation** in PDMS crystal: (a) *I* 4_1 (No. 80), (b) *I* 4_1 /*a*:1 (No. 88) with all atom site occupancy of 0.5.

Figure 6.12 displays the "**extended model**" of *I* 4_1 (No. 80): two polymer chains related by the centering condition and running along the *c*-axis (parallel to the 4_1 symmetry axis). The tetragonal unit cell has parameters ***a* = *b* = 8.428 Å and *c* = 12.053 Å** and the cell volume is **856.26 Å^3** (the parameters are slightly relaxed to allow for the chain formation). In this initial crystal structure, silicon and oxygen atoms are located very close to the chain axis and all methyl groups pointing outwards

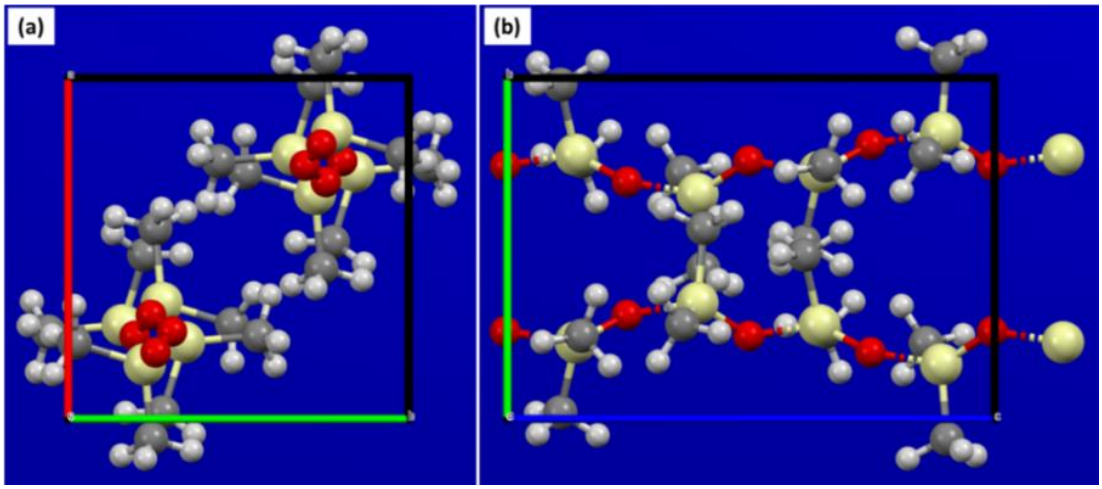

Figure 6.12 The model of PDMS crystal structure [*I* 4_1 (No. 80)]: (**a**) top view (**b**) side view

Figure 6.13 shows the "**helical model**" of *I* 4_1/*a*:1 (No. 88) with all atom site occupancy of 0.5, four chains adopt similar conformation within a tetragonal unit cell with parameters of ***a* = *b* = 8.432 Å and *c* = 12.061 Å**. The probability of finding a chain at a given location is fixed to 1/2.

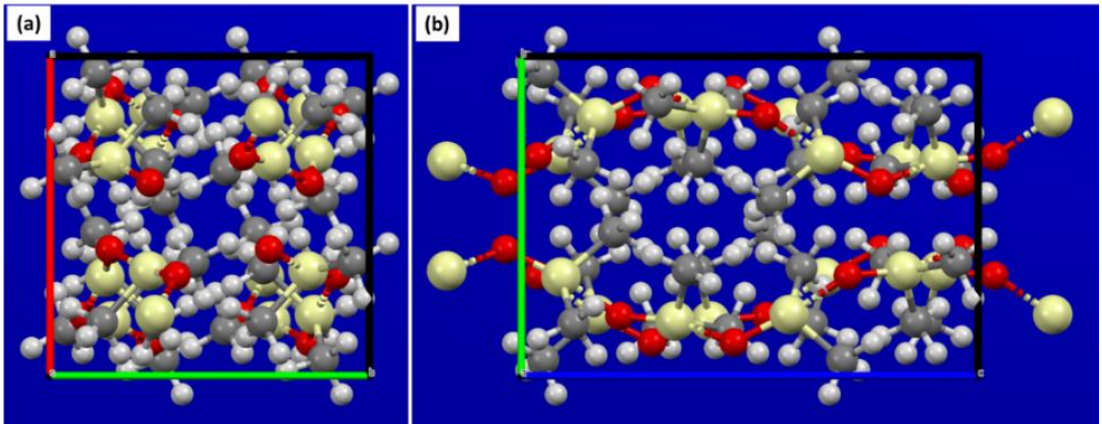

Figure 6.13 The **helical model** of PDMS crystal structure [$I\,4_1/a$:1 (No. 88)] with all atom site occupancy of 0.5: (**a**) top view (**b**) side view.

We used the software Mercury to get the simulated powder diffraction pattern of the two models: see **Figure 6.14**. If we let the 110 reflection apart, which is experimentally absent and computed rather intense for space group $I\,4_1$, the agreement with the experimental data seems better for the extended model [$I\,4_1$ (No. 80)] compared to the helical model [$I\,4_1/a$:1 (No. 88)].

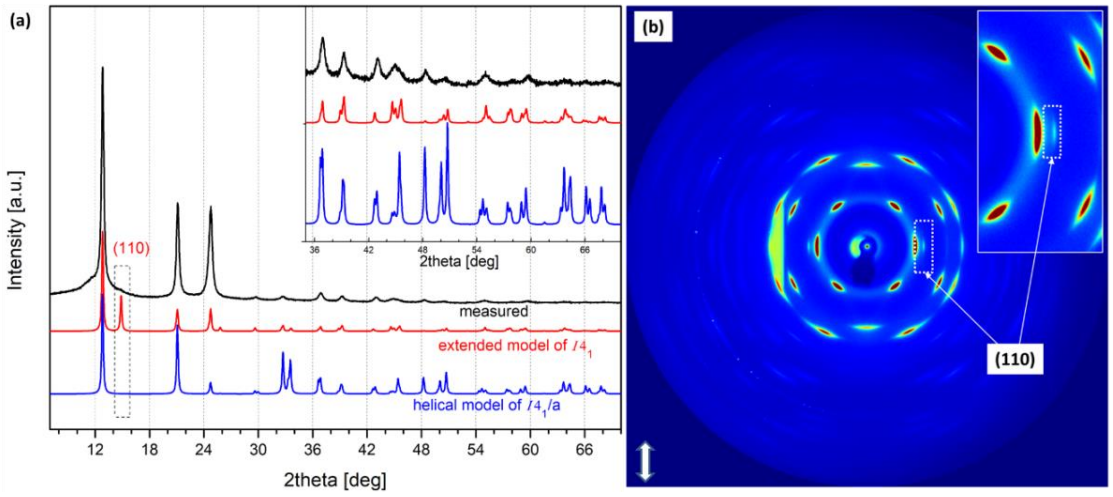

Figure 6.14 (a) the comparison between experimental and calculated XRD profiles of the two crystal structure models, (b) the appearance of reflection (110) in the WAXD pattern measured at high preset strains, with Mo Kα radiation used as the X-ray source and the direction of stretching (SD) is vertical.

The fundamental question of the 110 reflection is now discussed. It is actually not visible on crystallized oil and can be only detected in strained specimens (see **Figure 6.14-b**): in this last case, care must be taken that strain can slightly deform the unit cell. The 110 reflection corresponds to the incident beam reflection on the (110)

lattice planes. These are depicted in blue in **Figure 6.15** and the planes in-between are depicted in red.

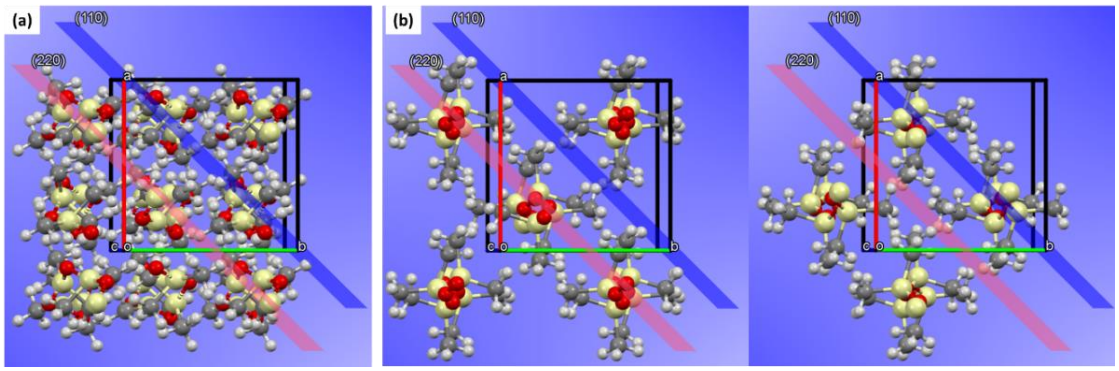

Figure 6.15 The top view of inter-chain conformation in the two possible crystal structures: (a) "helical model" [$I\,4_1/a$:1 (No. 88)] and (b) "extended model" [$I\,4_1$ (No. 80)] in two different packing modes.

In the case of space group $I\,4_1$, blue planes are high electron density planes (Silicon and oxygen atoms grouped on them) while red planes appears as low electron density planes, (the contrary can be chosen, see Figure in the center). This contrast explains the high computed intensity for the 110 reflection. On the other side, blue and red planes have similar electron densities for the $I\,4_1$ group and the 110 reflection is no more present. In this last case, this equilibrium can be destroyed when PDMS crystalized under high preset elongation and the 110 reflection may appear.

6.4.6.2 Geometry optimization

Quantum Espresso (QE)[42] is an open source set of computer codes designated to perform electronic structure calculations based on density functional theory (DFT), plane waves, and pseudopotentials that is capable of calculating the energy of and performing local optimizations on periodic crystal systems. It was only run for the $I\,4_1$ space group.

The initial crystal structure of the extended model [$I\,4_1$ (No. 80)] was geometrical optimized: the optimization of intermolecular interactions is completed in a fixed cell calculation by means of the PBE approximation (using the RRKJUS-PBE for C and H, along with the NL-RRKJUS_PSL-PBE for the Si and O). Meanwhile, van der Waals corrections were applied according to Grimme's DFT-D3 approach[43] . For the auxiliary basis set of plane waves and charge, the cutoff 45 Ry and 450 Ry were used. Finally, the optimized crystal structure is presented in **Figure 6.16**: it was found

that the DFT optimization yields a more extended four-fold helical configuration within the tetragonal unit cell with parameters of $\boldsymbol{a} = \boldsymbol{b} = \mathbf{8.428}$ Å and $\boldsymbol{c} = \mathbf{12.053}$ Å.

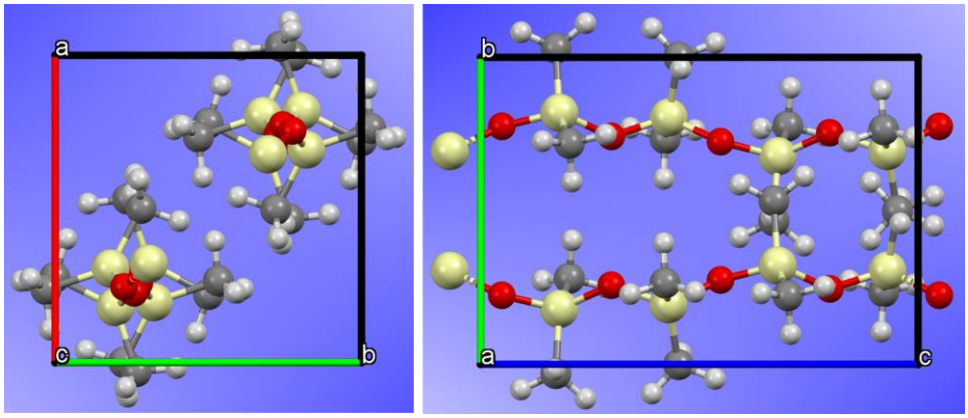

(a) (b)

Figure 6.16 The optimized PDMS crystal structure [I 41 (No. 80)]: (a) top view (b) side view

On the other hand, similar method of DFT optimization was applied for the case of the helical model [$I\,4_1/a$:1 (No. 88)] with half site occupancy, the chain conformation become more stretched in the lattice, showed in **Figure 6.17**, and the lattice parameters are $\boldsymbol{a} = \boldsymbol{b} = \mathbf{8.432}$ Å and $\boldsymbol{c} = \mathbf{12.061}$Å.

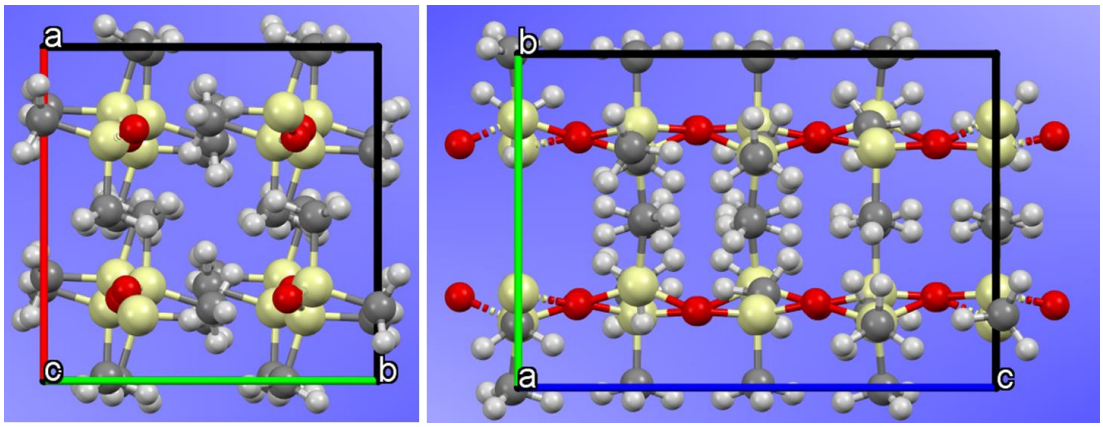

(c) **(d)**

Figure 6.17 The optimized PDMS crystal structure [$I\,4_1/a$:1 (No. 88)] with all atom site occupancy of 0.5: (c) top view (d) side view

6.4.6.3 Rietveld refinement and fitting

For successful Rietveld refinement, the initial structural model (taken from the structure solution) must be a sufficiently close representation of the correct structure. As Rietveld refinements often suffer from problems of instability, the use of geometric restraints (soft constraints) based on standard molecular geometries generally need to be applied in order to ensure stable convergence of the refinement. Furthermore, it is common to use only isotropic displacement parameters in Rietveld refinement, rather

than the anisotropic displacement parameters that are generally refined (except in the case of hydrogen atoms) for XRD data.

On basis of the experimental parameters that obtained from the step of profile fitting, the simulated x-ray diffraction information was obtained by Rietveld refinement, which was compared with the experimental XRD data, showed in **Figure 6.18**. Clearly, the relative intensity of the three most intense reflections is well-accounted except for the 110 reflection but the adjustment quality is rather average at higher angles. The associated crystallographic information is given in **Table 6.3**, together with the atomic coordinates of the asymmetric unit (**Table 6.4**), bond lengths, bond angles and torsion angles deduced from the Rietveld refinement (**Table 6.5**).

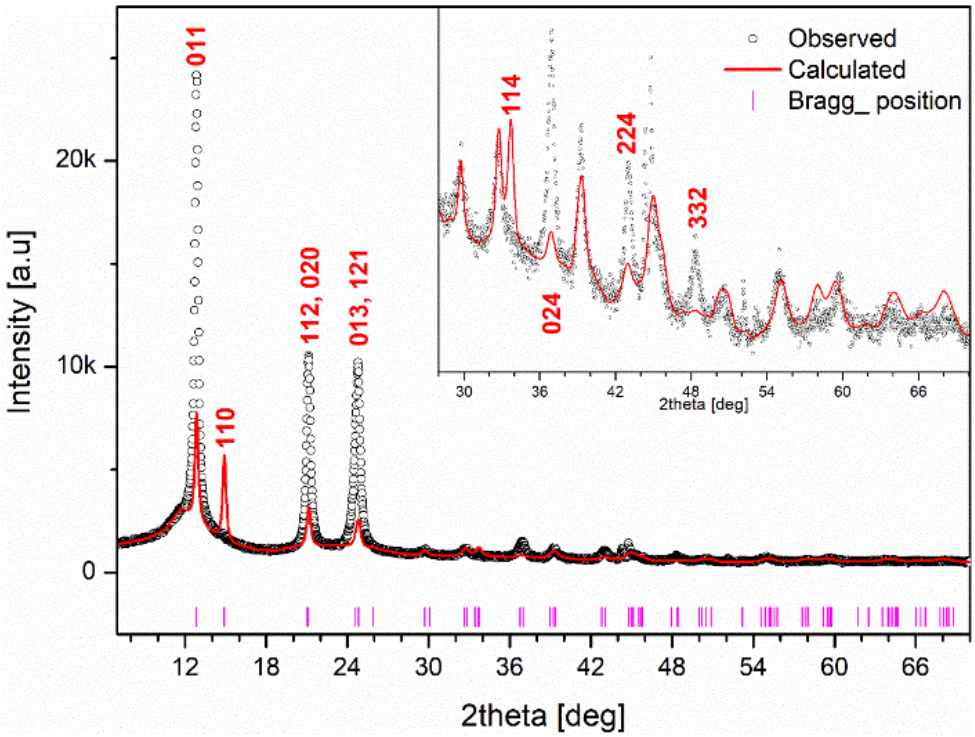

Figure 6.18 The refinement of the optimized crystal structure of extended model [$I\,4_1$ (No. 80)].

Table 6.3 Crystallographic information for the final PDMS crystal structure

Cell Lengths (Å)	a	8.428	b	8.428	c	12.053
Cell Angles (deg)	alpha	90	beta	90	gamma	90
Space Group			*I* 41 (No. 80)			
Symmetry operations	1) x, y, z					
	2) -y, x+1/2, z+1/4					
	3) -x+1/2, -y+1/2, z+1/2					
	4) y+1/2, -x, z+3/4					

5) x+1/2, y+1/2, z+1/2	
6) -y+1/2, x, z+3/4	
7) -x, -y, z	
8) y, -x+1/2, z+1/4	
Cell Volume ($Å^3$)	856.262
Cell Content	$Si_8O_8C_{16}H_{48}$
Density (g/cm^3)	1.150

Table 6.4 Fractional Atomic Coordinates of the asymmetric unit for the final PDMS crystal structure

Number	Label	x	y	z	Occ.
1	Si1	0.16004	0.74223	0.03544	1.0
2	O2	0.26937	0.79277	-0.0779	1.0
3	C3	-0.057	0.80476	0.02779	1.0
4	H4	-0.1168	0.77835	0.10721	1.0
5	H5	-0.1198	0.7411	-0.0385	1.0
6	H6	-0.0835	0.92965	0.012	1.0
7	C7	0.18558	0.52497	0.01512	1.0
8	H8	0.14409	0.49158	-0.0686	1.0
9	H9	0.11583	0.46254	0.07782	1.0
10	H10	0.3102	0.48614	0.02262	1.0

[a] Symmetry transformation was used to generate other equivalent atoms

Table 6.5 bond lengths, bond angles and torsion angles of the asymmetric unit for the final crystal structure

Number	Atoms			Length(Å) or Angle(°)
1	Si1	O2		1.6949
2	Si1	C3		1.8992
3	Si1	C7		1.8532
4	Si1	O1		1.703
5	O2	Si1		1.703
6	C3	H4		1.0998
7	C3	H5		1.0943
8	C3	H6		1.0887
9	C7	H8		1.0997
10	C7	H9		1.0882
11	C7	H10		1.0999
1	O2	Si1	C3	114.33
2	O2	Si1	C7	94.49

3	O2	Si1	O2		127.83
4	C3	Si1	C7		112.14
5	C3	Si1	O2		103.47
6	C7	Si1	O2		103.39
7	Si1	O2	Si1		139.35
8	Si1	C3	H4		109.9
9	Si1	C3	H5		111.26
10	Si1	C3	H6		118.07
11	H4	C3	H5		108.18
12	H4	C3	H6		104.6
13	H5	C3	H6		104.22
14	Si1	C7	H8		109.55
15	Si1	C7	H9		108.72
16	Si1	C7	H10		113.03
17	H8	C7	H9		109.78
18	H8	C7	H10		107.5
19	H9	C7	H10		108.22
1	C3	Si1	O2	Si1	-21.61
2	C7	Si1	O2	Si1	95.16
3	O2	Si1	O2	Si1	-154.04
4	O2	Si1	C3	H4	-174.52
5	O2	Si1	C3	H5	65.69
6	O2	Si1	C3	H6	-54.73
7	C7	Si1	C3	H4	79.42
8	C7	Si1	C3	H5	-40.37
9	C7	Si1	C3	H6	-160.79
10	O2	Si1	C3	H4	-31.35
11	O2	Si1	C3	H5	-151.14
12	O2	Si1	C3	H6	88.44
13	O2	Si1	C7	H8	-56.12
14	O2	Si1	C7	H9	-176.08
15	O2	Si1	C7	H10	63.72
16	C3	Si1	C7	H8	62.44
17	C3	Si1	C7	H9	-57.53
18	C3	Si1	C7	H10	-177.72
19	O2	Si1	C7	H8	173.25
20	O2	Si1	C7	H9	53.29
21	O2	Si1	C7	H10	-66.9

In the helical model [$I\ 4_1/a$:1 (No. 88)], the refinement (see **Figure 6.19**) exhibits rather large discrepancies for two of the more intense line, although the absence of 110 reflections is of course accounted for. The adjustment is quite average for the weaker lines located at larger scattering angles. The corresponding crystallographic information is given in **Table 6.6**, together with the atomic coordinates of the asymmetric unit (**Table 6.7**), bond lengths, bond angles and torsion angles deduced from the Rietveld refinement (**Table 6.8**).

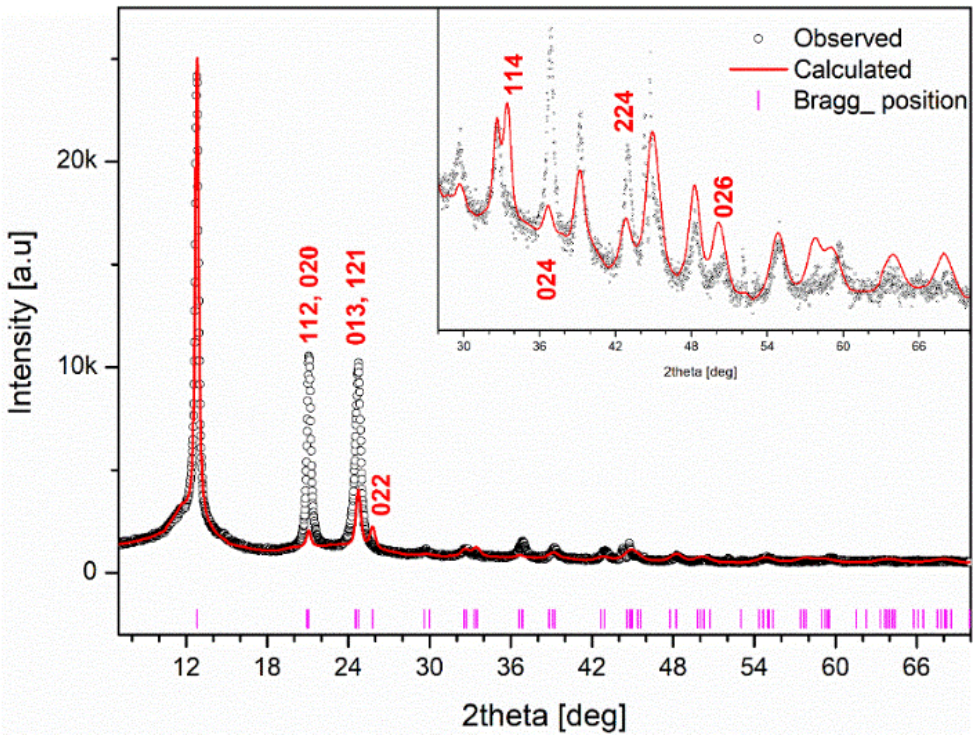

Figure 6.19 The refinement of the optimized PDMS crystal structure of helical model [$I\ 4_1/a$:1 (No. 88)] with all atom site occupancy of 0.5.

Table 6.6 Crystallographic information for the PDMS crystal structure

Cell Lengths (Å)	a	8.432	b	8.432	c	12.061
Cell Angles (deg)	alpha	90	beta	90	gamma	90
Space Group	$I\ 41/a:1$ (No. 80-1)					
Symmetry operations	1) x, y, z 2) -y, x+1/2, z+1/4 3) -x+1/2, -y+1/2, z+1/2 4) y+1/2, -x, z+3/4 5) -x, -y+1/2, -z+1/4 6) y, -x, -z 7) x+1/2, y, -z+3/4 8) -y+1/2, x+1/2, -z+1/2 9) x+1/2, y+1/2, z+1/2 10) -y+1/2, x, z+3/4					

	11) -x, -y, z 12) y, -x+1/2, z+1/4 13) -x+1/2, -y, -z+3/4 14) y+1/2, -x+1/2, -z+1/2 15) x, y+1/2, -z+1/4 16) -y, x, -z 1) x, y, z
Cell Volume ($Å^3$)	856.61
Cell Content	$Si_8O_8C_{16}H_{48}$
Density (g/cm^3)	1.150

Table 6.7 Fractional Atomic Coordinates of the asymmetric unit for PDMS crystal structure

Number	Label	x	y	z	Occ.
1	Si1	0.19558	0.28173	1.00046	0.5
2	O1	0.25353	0.27096	0.87252	0.5
3	C1	0.18749	0.49103	1.00221	0.5
4	H1	0.11796	0.53214	0.078	0.5
5	H17	0.12627	0.53511	0.92378	0.5
6	H33	0.31303	0.54091	1.00599	0.5
7	C17	-0.00445	0.21878	1.01409	0.5
8	H49	-0.00737	0.08904	0.0406	0.5
9	H65	0.93221	0.23248	0.93114	0.5
10	H81	0.93339	0.29439	0.07929	0.5

[a] Symmetry transformation was used to generate other equivalent atoms

Table 6.8 bond lengths, bond angles and torsion angles of the asymmetric unit for the final crystal structure

Number	Atoms			Length(Å) or Angle(°)
1	Si1	O1		1.621
2	Si1	C1		1.766
3	Si1	C17		1.776
4	Si1	O1		1.631
5	O1	Si1		1.631
6	C1	H1		1.140
7	C1	H17		1.140
8	C1	H33		1.140
9	C17	H49		1.140
10	C17	H65		1.140
11	C17	H81		1.140
1	O1	Si1	C1	94.53
2	O1	Si1	C17	110.96
3	O1	Si1	O1	137.02
4	C1	Si1	C17	105.12
5	C1	Si1	O1	100.74

6	C17	Si1	O1		103.42
7	Si1	O1	Si1		145.7
8	Si1	C1	H1		109.47
9	Si1	C1	H17		109.47
10	Si1	C1	H33		109.47
11	H1	C1	H17		109.47
12	H1	C1	H33		109.47
13	H17	C1	H33		109.47
14	Si1	C17	H49		109.47
15	Si1	C17	H65		109.48
16	Si1	C17	H81		109.47
17	H49	C17	H65		109.47
18	H49	C17	H81		109.47
19	H65	C17	H81		109.47
1	C1	Si1	O1	Si1	-125.71
2	C17	Si1	O1	Si1	-17.62
3	O1	Si1	O1	Si1	123.23
4	O1	Si1	C1	H1	165.27
5	O1	Si1	C1	H17	45.27
6	O1	Si1	C1	H33	-74.73
7	C17	Si1	C1	H1	52.13
8	C17	Si1	C1	H17	-67.87
9	C17	Si1	C1	H33	172.12
10	O1	Si1	C1	H1	-55.09
11	O1	Si1	C1	H17	-175.09
12	O1	Si1	C1	H33	64.9
13	O1	Si1	C17	H49	96.55
14	O1	Si1	C17	H65	-23.44
15	O1	Si1	C17	H81	-143.45
16	C1	Si1	C17	H49	-162.43
17	C1	Si1	C17	H65	77.57
18	C1	Si1	C17	H81	-42.43
19	O1	Si1	C17	H49	-57.18
20	O1	Si1	C17	H65	-177.18
21	O1	Si1	C17	H81	62.82

6.5 Conclusion

We are still confronted to the puzzling situation where no satisfying solution can be proposed for the PDMS crystalline structure. The tetragonal unit cell we propose accounts for the position of all observed diffraction lines with high precision and only

two cell parameters: it can hardly be discarded. Furthermore, the crystalline density points to 8 monomers per unit cell and this cannot be also discarded. If we now consider the extended model [$I\,4_1$ (No. 80)], the question of the absence of the 110 reflection is not solved (it is visible on patterns of stretched samples but remains weak and could be due to some distortion). A predicted intense 110 reflections are intrinsic to the proposed structure (strong density modulation along the [110] direction). Moreover, each crystallite only contains chains with either 4_1 or 4_3 helical conformation and such a selection is unusual. On the other hand, the helical model of [$I\,4_1/a$:1 (No. 88-1)] with atom site occupancy of 0.5 fails to account correctly for the relative intensity of the three most intense diffraction lines. It remains that we give an occupancy 0.5 to every monomer while it should be given to an entire chain, in the 4_1 or 4_3 conformation. We had no time to go deeper in this question.

Indeed, a very intriguing fact is the fact underlined above that the parameter *c* is very close to $a\sqrt{2}$. Indeed, this may be a mere coincidence. However, a conformation analysis could be performed to see if a polymer chain propagating along the c-axis cannot turn at right angle and extend along the [110] direction before turning again along the c-axis. This would be a manner to explain an occupancy of 1/2 in a model based on space group $I\,4_1/a$: a chain can go from one location to another. This could be an explanation for the texture evolution: the [111] orientation observed at higher strains as fiber axis could be a compromise for chains running along the [001] and [111] directions.

A last point to notice is that the textured patterns obtained for instance with the shorter wavelength set-up could be deeper analyzed. The relative intensity of hardly resolved line doublets in the crystallized oil could be easily deduced from these patterns as the lines get well-separated.

References

[1] Owen, M. J. (1981). Why silicones behave funny. *Chemtech*, 288-292.

[2] Damaschun, G. (1962). Röntgenographische untersuchung der struktur von silikongummi. *Kolloid-Zeitschrift und Zeitschrift für Polymere*, 180(1), 65-67.

[3] Albouy, P. A. (2000). The conformation of poly (dimethylsiloxane) in the crystalline state. *Polymer*, 41(8), 3083-3086.

[4] Tosaka, M., Noda, M., Ito, K., Senoo, K., Aoyama, K., & Ohta, N. (2013). Strain- and temperature-induced polymorphism of poly (dimethylsiloxane). *Colloid and Polymer Science*, 291(11), 2719-2724.

[5] Tosaka, M., & Tashiro, K. (2018). Crystal polymorphism and structure models of Poly (dimethylsiloxane). *Polymer*, 153, 507-520.

[6] Maus, A., & Saalwächter, K. (2007). Crystallization Kinetics of Poly (dimethylsiloxane) Molecular-Weight Blends—Correlation with Local Chain Order in the Melt?. *Macromolecular Chemistry and Physics*, 208(19-20), 2066-2075.

[7] Clarson, S. J., Dodgson, K., & Semlyen, J. A. (1985). Studies of cyclic and linear poly (dimethylsiloxanes): 19. Glass transition temperatures and crystallization behaviour. *Polymer*, 26(6), 930-934.

[8] Klonos, P. A. (2018). Crystallization, glass transition, and molecular dynamics in PDMS of low molecular weights: A calorimetric and dielectric study. *Polymer*, 159, 169-180.

[9] Aranguren, M. I. (1998). Crystallization of polydimethylsiloxane: effect of silica filler and curing. *Polymer*, 39(20), 4897-4903.

[10] Soutzidou, M., Panas, A., & Viras, K. (1998). Differential scanning calorimetry (DSC) and Raman spectroscopy study of poly (dimethylsiloxane). *Journal of Polymer Science Part B: Polymer Physics*, 36(15), 2805-2810.

[11] Supaphol, P. (2001). Crystallization and melting behavior in syndiotactic polypropylene: origin of multiple melting phenomenon. *Journal of applied polymer science*, 82(5), 1083-1097.

[12] Blundell, D. J. (1987). On the interpretation of multiple melting peaks in poly (ether ether ketone). *Polymer*, 28(13), 2248-2251.

[13] Sun, Y. S., & Woo, E. M. (1999). Relationships between polymorphic crystals and multiple melting peaks in crystalline syndiotactic polystyrene. *Macromolecules*, 32(23), 7836-7844.

[14] Helmer, J. D., & Polmanteer, K. E. (1969). Supercooling of polydimethylsiloxane. *Journal of applied polymer science*, 13(10), 2113-2118.

[15] de Wolff, P. D. (1968). A simplified criterion for the reliability of a powder pattern indexing. *Journal of Applied Crystallography*, 1(2), 108-113.

[16] Smith, G. S., & Snyder, R. L. (1979). FN: A criterion for rating powder diffraction patterns and evaluating the reliability of powder-pattern indexing. *Journal of Applied Crystallography*, 12(1), 60-65.

[17] Visser, J. W. (1969). A fully automatic program for finding the unit cell from powder data. *Journal of Applied Crystallography*, 2(3), 89-95.

[18] Werner, P. E., Eriksson, L., & Westdahl, M. (1985). TREOR, a semi-exhaustive trial-and-error powder indexing program for all symmetries. *Journal of Applied Crystallography*, 18(5), 367-370.

[19] Boultif, A., & Louër, D. (1991). Indexing of powder diffraction patterns for low-symmetry lattices by the successive dichotomy method. *Journal of Applied Crystallography*, 24(6), 987-993.

[20] Shirley, R. (2000). The CRYSFIRE system for automatic powder indexing: user's manual. *The Lattice*.

[21] Le Bail, A. (2004). Monte carlo indexing with mcmaille. *Powder Diffraction*, 19(3), 249-254.

[22] Shirley, R. (2003). Overview of powder-indexing program algorithms (history and strengths and weaknesses). *Commission on Crystallographic Computing*, 48.

[23] Giacovazzo, C. A. R. M. E. L. O. (1996). Direct methods and powder data: State of the art and perspectives. *Acta Crystallographica Section A: Foundations of Crystallography*, 52(3), 331-339.

[24] Kaduk, J. A. (2002). Use of the Inorganic Crystal Structure Database as a problem-solving tool. *Acta Crystallographica Section B: Structural Science*, 58(3), 370-379.

[25] Pawley, G. S. (1981). Unit-cell refinement from powder diffraction scans. *Journal of Applied Crystallography*, 14(6), 357-361.

[26] Le Bail, A., Duroy, H., & Fourquet, J. L. (1988). Ab-initio structure determination of LiSbWO6 by X-ray powder diffraction. *Materials Research Bulletin*, 23(3), 447-452.

[27] Altomare, A. G. C. A. M. C. G. M., Cascarano, G., Giacovazzo, C., Guagliardi, A., Burla, M. C., Polidori, G. T., & Camalli, M. (1994). SIRPOW. 92–a program for automatic solution of crystal structures by direct methods optimized for powder data. *Journal of Applied Crystallography*, 27(3), 435-436.

[28] Wilson, C. C. (1989). Determination of crystal structures from poor-quality data using Patterson methods. *Acta Crystallographica Section A: Foundations of Crystallography*, 45(12), 833-839.

[29] Harris, K. D., Tremayne, M., Lightfoot, P., & Bruce, P. G. (1994). Crystal structure determination from powder diffraction data by Monte Carlo methods. *Journal of the American Chemical Society*, 116(8), 3543-3547.

[30] Ramprasad, D., Pez, G. P., Toby, B. H., Markley, T. J., & Pearlstein, R. M. (1995). Solid state lithium cyanocobaltates with a high capacity for reversible dioxygen binding: Synthesis, reactivity, and structures. *Journal of the American Chemical Society*, 117(43), 10694-10701.

[31] Pagola, S., Stephens, P. W., Bohle, D. S., Kosar, A. D., & Madsen, S. K. (2000). The structure of malaria pigment β-haematin. *Nature*, 404(6775), 307-310.

[32] Kariuki, B. M., Calcagno, P., Harris, K. D., Philp, D., & Johnston, R. L. (1999). Evolving opportunities in structure solution from powder diffraction data—Crystal structure determination of a molecular system with twelve variable torsion angles. *Angewandte Chemie International Edition*, 38(6), 831-835.

[33] Kariuki, B. M., Psallidas, K., Harris, K. D., Johnston, R. L., Lancaster, R. W., Staniforth, S. E., & Cooper, S. M. (1999). Structure determination of a steroid directly from powder diffraction data. *Chemical Communications*, (17), 1677-1678.

[34] Turner, G. W., Tedesco, E., Harris, K. D., Johnston, R. L., & Kariuki, B. M. (2000). Implementation of Lamarckian concepts in a genetic algorithm for structure solution from powder diffraction data. *Chemical Physics Letters*, 321(3-4), 183-190.

[35] Habershon, S., Harris, K. D., & Johnston, R. L. (2003). Development of a multipopulation parallel genetic algorithm for structure solution from powder diffraction data. *Journal of computational chemistry*, 24(14), 1766-1774.

[36] Young, R. A. (Ed.). (1993). The rietveld method (Vol. 6). *Oxford: Oxford university press*.

[37] Rietveld, H. (1969). A profile refinement method for nuclear and magnetic structures. *Journal of applied Crystallography*, 2(2), 65-71.

[38] McCusker, L. B., Von Dreele, R. B., Cox, D. E., Louër, D., & Scardi, P. (1999). Rietveld refinement guidelines. *Journal of Applied Crystallography*, 32(1), 36-50.

[39] Rodríguez-Carvajal, J. (2001). FullProf. CEA/Saclay, France.

[40] Hofmann, D. W. (2002). Fast estimation of crystal densities. *Acta Crystallographica Section B: Structural Science*, 58(3), 489-493.

[41] Altomare, A., Cuocci, C., Giacovazzo, C., Moliterni, A., Rizzi, R., Corriero, N., & Falcicchio, A. (2013). EXPO2013: a kit of tools for phasing crystal structures from powder data. *Journal of Applied Crystallography*, 46(4), 1231-1235.

[42] Giannozzi, P., Baroni, S., Bonini, N., Calandra, M., Car, R., Cavazzoni, C., ... & Dal Corso, A. (2009). QUANTUM ESPRESSO: a modular and open-source software project for quantum simulations of materials. *Journal of physics: Condensed matter*, 21(39), 395502.

[43] Grimme, S., Antony, J., Ehrlich, S., & Krieg, H. (2010). A consistent and accurate ab initio parametrization of density functional dispersion correction (DFT-D) for the 94 elements H-Pu. *The Journal of chemical physics*, 132(15), 154104.

Chapter 7

Structural Study of Cholesterol-based Organogelators

Contents

7.1 Introduction

Physical gelation of functional fluids such as liquid crystals is an interesting approach for the development of functional molecular materials. As one of the liquid crystal building blocks (mesogens), the cholesteryl unit has been incorporated extensively as mesogen and/or gelator in material science[1] [2] , due to (i) the commercial availability of the cholesterol as an inexpensive natural product, (ii) its rigid structure with eight chiral centers (an attractive feature for realizing chirality in mesophases), and (iii) the ease to get derivatives by chemical reaction.

Recently, a number of photo-sensitive segments like azobenzene[3] , tetrathiafulvalene[4] , dithienylethene[5] and perylene[6] have been introduced into the cholesterol based gelators, which endow these materials with light-responsive functions. Meanwhile, as an emblematic luminophore with aggregation-induced emission (AIE) properties, tetraphenylethylene (TPE) has also been combined with cholesterol moisty to develop advanced optical materials, owing to their interesting features of gelation enhanced emission[7] . For example, Wang and Ma[8] have prepared AIE organogels by connecting tetraphenylethylene and cholesterol moieties to a central salicylideneaniline. Their systems allow one to make use of the Excited-State Intramolecular Proton Transfer (ESIPT) process with large Stokes shift in gel state.

During my PhD research, in cooperation with M. Hui CHEN in Chimie ParisTech (Université PSL Paris), we have developed new stimuli-responsive AIE fluorescent gelators from two series of cholesterol-based compounds, **TPE-C$_n$-Chol** (with n = 1, 4, 5, 6) and **TPE-Azobenzene-C$_n$-Chol** (with n = 0, 1, 3, 5) (see **Scheme 7.1**). My contribution in these works is the participation to the structural study of these organogels by X-ray diffraction, differential scanning calorimetry (DSC) and thermal polarizing optical microscopy (POM).

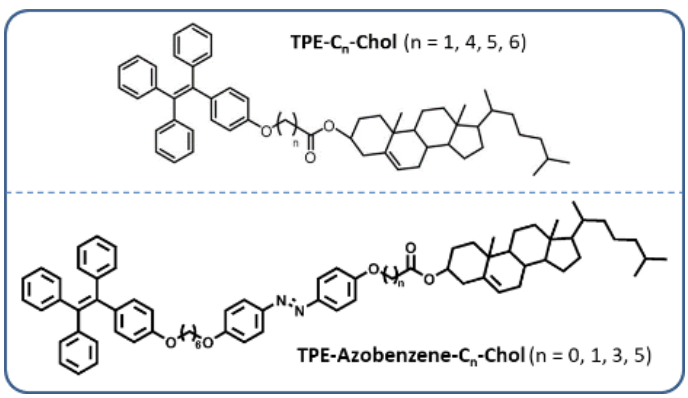

Scheme 7.1 Molecular structure of the two series of cholesterol-based compounds.

7.2 Background

In this section, thermotropic liquid crystals and X-ray scattering of liquid crystals will be briefly presented.

7.2.1 Thermotropic liquid crystals

In the liquid crystal phase (mesophase), the liquid crystal (LC) molecules possess, at the same time, certain orders of crystals, like the orientational order, and certain disorders of liquid, like the absence of long-range positional order giving rise to the fluidity. There are thermotropic and lyotropic LC phases. In this thesis we discuss only thermotropic LC phases where a phase transition into the LC phase is obtained as the temperature is changed.

The thermotropic LC molecules are normally composed of a central core (often aromatic or other rigid core) and one or several flexible peripheral moieties (generally aliphatic chains). Based on the shape of mesogens, thermotropic LCs are classified into three main groups: (a) calamitic (rod-like), (b) bent-core (banana-like), and (c) discotic (disk-like) LCs, as illustrated in **Figure 7.1**.

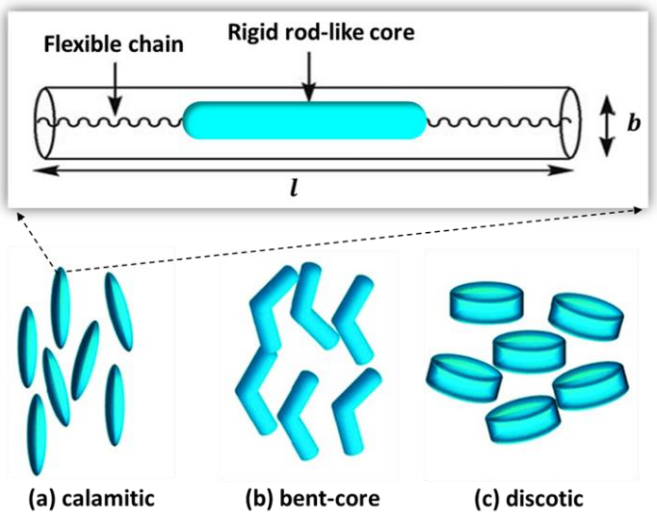

Figure 7.1 Schematic representation of the main types of thermotropic LCs (for a calamitic LC molecule, the molecular length ***l*** is significantly greater than the molecular breadth ***b***).

In thermotropic LC, the transition temperature from the crystal to the mesophase is called the ***melting point***, while the transition temperature from the mesophase to the isotropic liquid is called the ***clearing point***. When a thermodynamically stable mesophase is obtained both on heating and cooling, the phase is called ***enantiotropic***.

When the mesophase is obtained only upon cooling from the isotropic liquid, it is called the ***monotropic*** phase.

Between the melting point and the clearing point, different mesophases can be observed depending on the orientational and positional orders of mesogens, as shown in **Figure 7.2**. **Nematic phase (N)** and **smectic phases (Sm)** are the most common mesophases. In the nematic phase, the mesogens present only a long-range orientational order. In the smectic phases, a positional order with layer structure exists, while each layer can be considered as a 2D nematic where only the average orientation of the mesogens are defined without positional order. Depending on whether the director is parallel or tilted with respect to the layer normal, smectic mesophases can be classified as **SmA** and **SmC** phases. Other LC phases are formed when the chirality is introduced in the molecules, like chiral nematic phase **N***, ferroelectric phase **SmC***, twist grain boundary phases, etc. The chiral nematic phase is also called the cholesteric phase. In the chiral phases, successive molecules positioned along the long axis are rotated around this axis, giving rise to a periodicity that repeats itself at distances corresponding to a complete rotation.

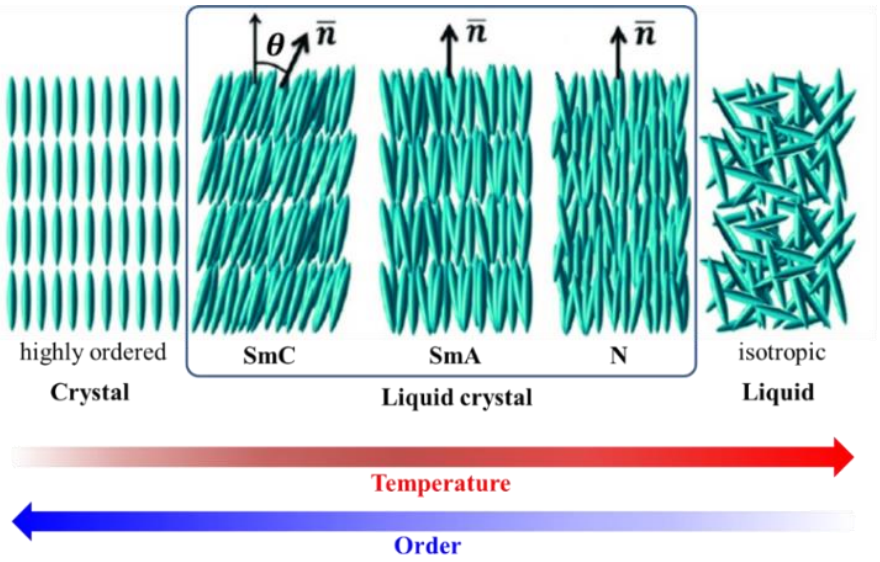

Figure 7.2 Schematic representation of the crystal, liquid crystal and liquid state with different arrangement of LC molecules. $\bar{n}$ refers to the direction of molecules and θ is the tilted angle between the molecular axis and layer normal direction.

7.2.2 X-ray scattering study of liquid crystals

The unaligned (polydomain) samples with different LC phases can yield scattering patterns with isotropic diffraction rings, as discussed in the work of Seddon[9] .

Thus, the most useful information is the peak positions in scattering vector $\boldsymbol{q}$, which are reciprocally related to the separations between molecules (or groups of molecules) within the liquid crystalline phase. The sharpness of the peaks is related to the extent to which the separations extend periodically over large distances. For phases with Bragg peaks, the ratio of the peak positions reveals the long-range organization of the phase, as shown in **Figure 7.3**, which can be used to assesses the structure information of the mesophase.

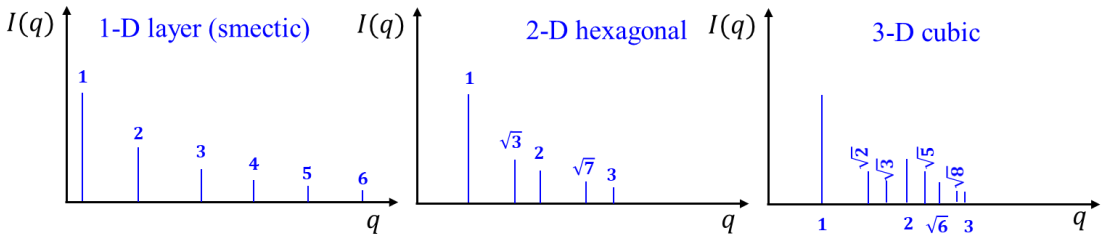

Figure 7.3 SAXS profile of characteristic 1-D layer (smectic) phases, 2-D hexagonal phases, and 3-D cubic phases.

On the other hand, the X ray diffraction of the aligned (monodomain) sample is essential for the detailed structural studies of liquid crystals. The alignment may be achieved under magnetic fields or by surface treatments. The molecular arrangement in different LC phases, together with their corresponding X-ray scattering patterns and diffraction intensity profiles obtained with aligned samples are schematically illustrated in Figure 7.4. For the aligned nematic phase, the diffraction pattern shows typically a set of diffuse arcs at wide angles along the equator. In some cases (*e.g.*, the aligned nematic phase in a main-chain liquid crystal polymer), a set of signals at small angles along the meridian (the direction of alignment) can be observed. They give information about the average lateral distance between two adjacent mesogens (b'), the LC order parameter, and the length of mesogen (l), as shown in **Figure 7.4-a**. In the case of the oriented smectic A phase (SmA), there are one or several pairs of narrow spots at small angles along the meridian due to the smectic layer spacing (d), and a pair of broad arcs at wide angle along the equatorial like in nematic phase. For aligned SmC phase, the small angle signals appear at a tilted angle $\boldsymbol{\theta}$ with respect to the meridian. As illustrated in Figure 7.4, the X ray diffraction patterns and intensity profiles of the aligned samples are essential to distinguish the different liquid crystal phases and to determine their structural parameters.

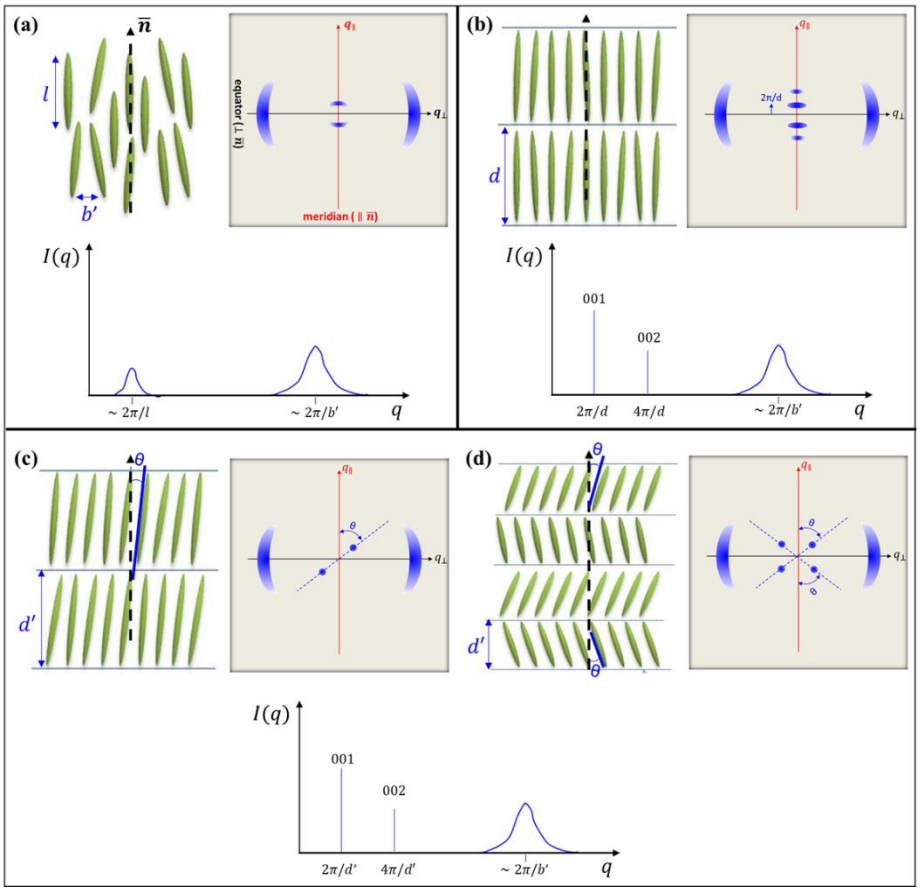

Figure 7.4 Schematic representation of molecular arrangements and their corresponding X-ray scattering patterns, diffraction profiles from aligned samples of different LC phases: (a) Nematic, (b) Smectic A, and (c, d) Smectic C phase in different alignment. $\bar{n}$ refers to the director of molecules and θ is the tilted angle between the director and the layer normal, *b'* is the average lateral distance between two neighbor liquid crystal molecules.

7.3 Experimental Section

7.3.1 Materials

The two series of organic compounds of **TPE-C_n-Chol** (with n = 1, 4, 5, 6) and **TPE-Azobenzene-C_n-Chol** (with n = 0, 1, 3, 5) (**Scheme 7.1)** were synthesized by my colleagues Hui CHEN and Xia YU. The synthetical protocols were presented in detail in our published articles[9] .

These compounds mainly consist of two or three representative units: (1) Cholesterol (Chol) moiety: a mesogen can act as gelator; (2) Azobenzene moiety: a mesogen with photosensitive properties; (3) Tetraphenylethylene (TPE) moiety: a popular luminogen with aggregation-induced emission (AIE) characteristics. Meanwhile, alkyl chains (-$O(CH_2)_nCOO$-) with different lengths were introduced into cholesterol-based system to adjust the distance between cholesterol and TPE moieties or TPE-azobenzene moieties.

7.3.2 X-ray scattering measurements

The X-ray diffraction and scattering experimental setups were showed in **Figures 7.5, 7.6, and 7.7.**

The powder X-ray diffraction characterization at room temperature was performed on a commercial Bruker D8 Advance diffractometer. The diffractometer is working at 40 kV and 40 mA in Bragg-Brentano geometry [theta/2theta scan mode] by using Cu Kα radiation (λ =1.5418 Å). The powder specimens are dispersed homogeneously in a sample-holder of round plastic plate to keep the reflection surface flat, with the diffraction data recorded by a LynxEye detector.

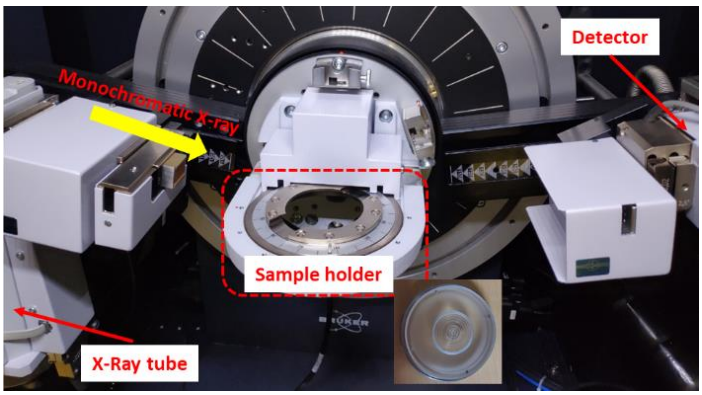

Figure 7.5 General view of the Bruker X-ray diffraction setup used for the room temperature (RT) measurement of powder sample.

The SAXS experiments of LC samples were carried out by using a homemade SAXS setup in transmission mode with monochromatized X-ray beam (λ=1.5418 Å), showed in **Figure 7.6**. The sample-to-detector distance was set 568 mm, and the scattering information was collected by square-shape photosensitive image plate with an X-ray exposure time of more than 10 minutes. For the thermal-SAXS, a heater was mounted for the characterization at different temperature in the solid state.

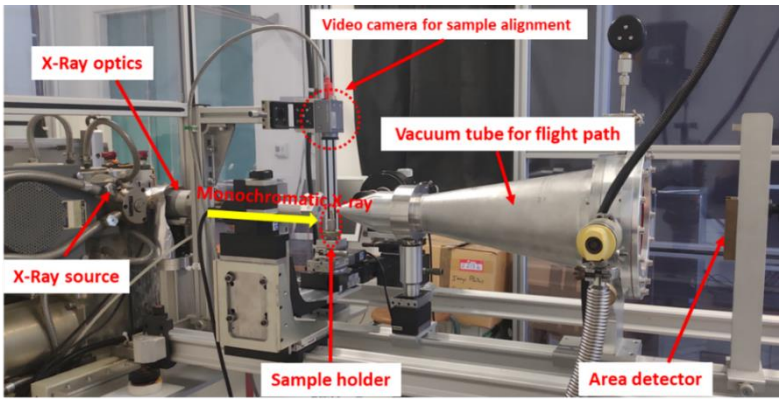

Figure 7.6 General view of the experimental home-made SAXS setup used for liquid crystal measured at RT and high temperature.

The WAXS experiments of LC samples were performed using a setup with Marr345 detector as shown in **Figure 7.7**, where the sample-to-detector distance can be adjusted automatically for the recording of good scattering patterns.

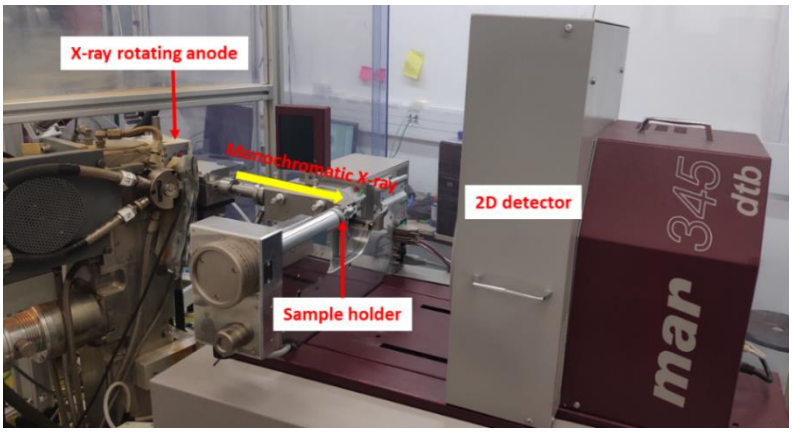

Figure 7.7 General view of the experimental WAXS set-up.

The d-spacing ***d*** and coherence length (averaged crystallite grain size) $\boldsymbol{\zeta}$ used in this chapter can be computed based on the Bragg's law and Scherrer's equation:

$$d = \frac{n\lambda}{2\sin\theta} \tag{7.1}$$

$$\boldsymbol{\zeta} = \frac{K\lambda}{\beta\cos\theta} \tag{7.2}$$

where n is a positive integer and λ is the wavelength of the incident X-ray, K is a dimensionless shape factor (about 0.9), β is the line broadening at half the maximum intensity (FWHM), θ is the Bragg angle.

7.3.3 Other techniques for liquid crystal characterization

The mesomorphic properties in the bulk state of the two series of cholesterol-based compounds, **TPE-Azobenzene-C_n-Chol** (with n = 0, 1, 3, 5) and **TPE-C_n-Chol** (with n = 1, 4, 5, 6), were also studied by Differential scanning calorimetry (DSC) and Thermal polarizing optical microscopy (POM).

DSC was performed using a Perkin-Elmer DSC7. Samples were scanned twice from RT to 210 ℃ with heating and cooling rates of 2 ℃/min. The phase transition temperatures were taken at the peak temperatures in DSC thermograms.

The mesomorphic phases of the sample were observed by thermal POM using a Leitz Ortholux microscope equipped with a Mettler FP82 hot stage.

7.4 Results and Discussion

7.4.1 AIE fluorescent gelators (TPE-Cn-Chol) with stimuli-responsive chromatic properties– Series TPE-Cn-Chol (n = 1, 4, 5, 6)

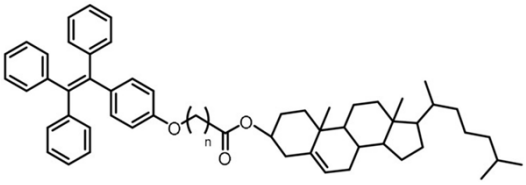

TPE-C_n-Chol (n = 1, 4, 5, 6)

7.4.1.1 DSC analysis and POM measurement

DSC and POM were firstly used to identify the phase transitions and phase types. The DSC curves of **TPE-C_n-Chol** series (**Figure 7.8**) show clearly that all these pristine powders (obtained by precipitation using dichloromethane/methanol as solvent/precipitant pair) present a remarkable melting point (higher than 100 ℃) in the first heating process. Upon subsequent cooling to RT, no recrystallization was detected. In the second heating/cooling scan, a glass transition with T_g between 40-50 ℃ is observed for all samples.

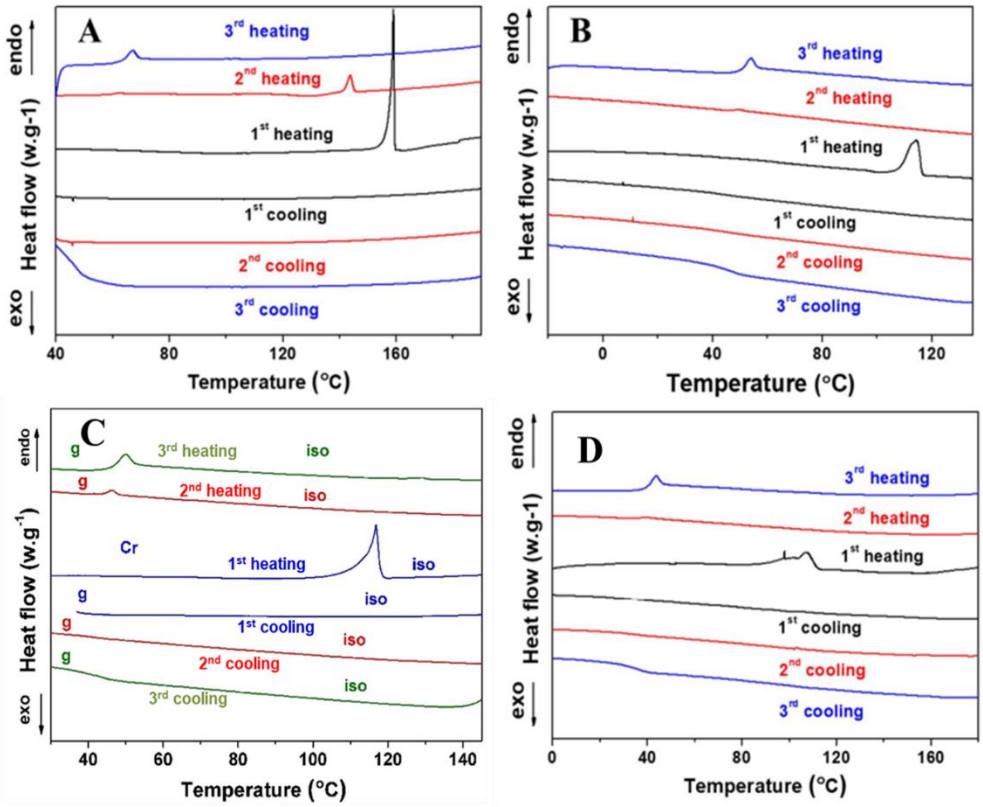

Figure 7.8 DSC thermograms of **TPE-C_n-Chol** upon the first, second and third heating-cooling cycle at a rate of 2 ℃ min^{-1}: (A) **n=1**, (B) **n=4**, (C) **n=5** and (D)**n=6**.

POM was also used to characterize the compounds. Taking **TPE-C_5-Chol** as an example, its POM images were recorded in crystalline and isotropic phases (**Figure 7.9 A and B)**. At room temperature, needle-like crystals with birefringence were observed. Heating to 150 ℃, POM image under crossed polarizer and analyzer showed an isotropic state without birefringence. This isotropic state was kept until room temperature to give a isotropic glass state. Very interestingly, both pristine crystalline state and isotropic states of **TPE-C_5-Chol** at room temperature show fluorescence under UV illumination (365 nm) (**Figure 7.9 C and D)**. Moreover, the fluorescence colors are different at two states. Therefore, we are interested in studying the relationship between the structures of the condensed phases and their fluorescence, as well as their stimuli-responsive chromatic properties.

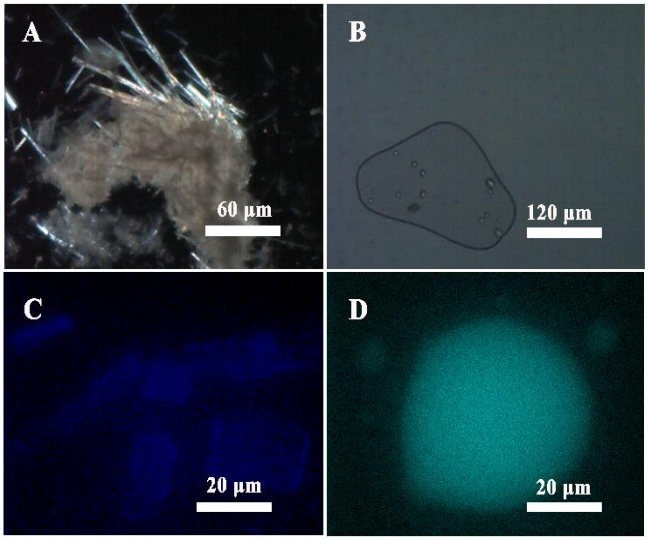

Figure 7.9 (A) POM image of pristine powder sample of TPE-C_5-Chol after synthesis and purification. (B) POM image of TPE-C_5-Chol in isotropic phase at 150 ℃ and in glass state at 25 ℃ (no modification was observed upon cooling from 150 ℃ to room temperature). (C) Fluorescence optical microscope image of pristine powder sample of TPE-C_5-Chol. (D) Fluorescence optical microscope image of TPE-C_5-Chol glass at 25 ℃ after cooling from the isotropic liquid phase. (excitation wavelength = 365 nm).

7.4.1.2 Stimuli-responsive chromatic property analysis

It was found that all **TPE-C_n-Chol** molecules possess thermo-, mechano-, and vapo-chromic properties. that is, they can change their fluorescence color from blue to cyan in the condensed state under external stimuli, such as melting, grinding, and solvent fuming.

In order to understand the mechanism behind these stimuli-sensitive chromic properties, powder X-ray diffraction characterization were carried out on different powder samples. Taking **TPE-C_5-Chol** as an example, its fluorescence spectra and the

corresponding XRD profiles in different treatments were presented and compared in **Figure 7.10**.

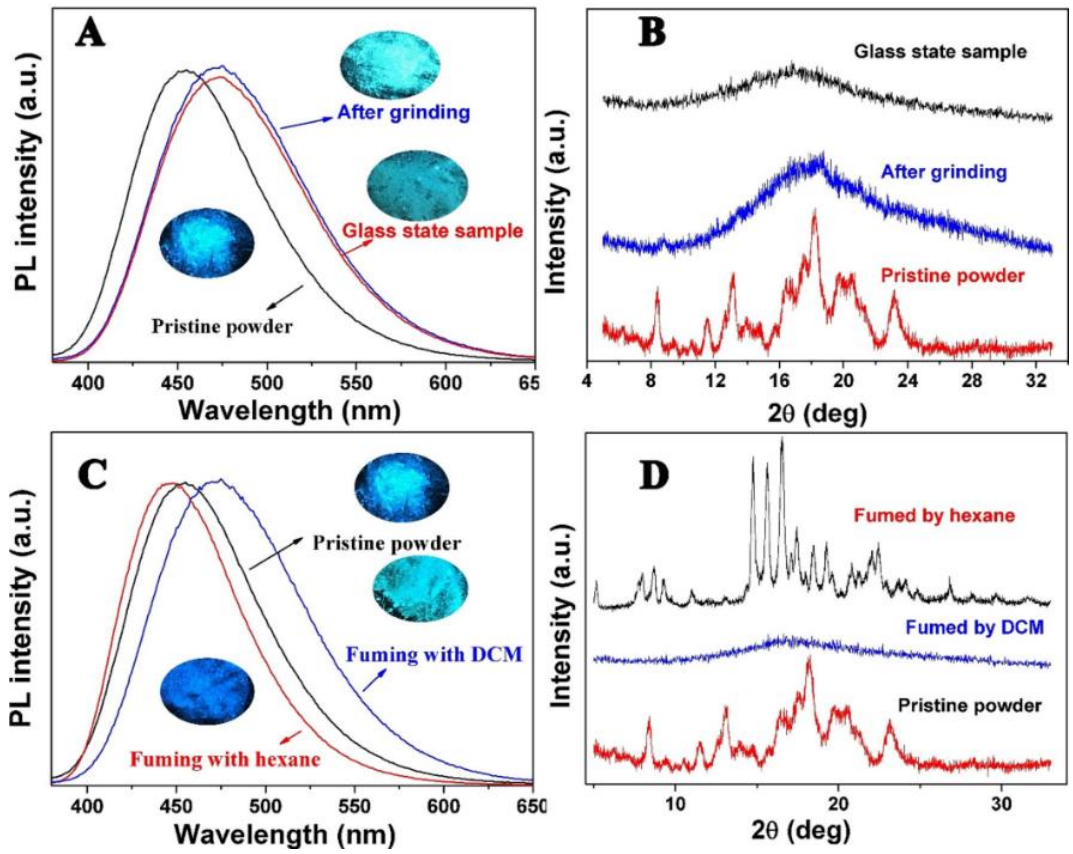

Figure 7.10 (A, B) Fluorescence spectra and the corresponding powder XRD profile of **TPE-C5-Chol** in different condensed states: pristine sample, ground sample, and in the glass state at RT after being heated to the isotropic phase (120 °C); (C, D) Fluorescence spectra and the corresponding XRD profile of **TPE-C5-Chol** before and after the different vapor treatments: pristine, fumed with DCM and hexane. Insets: Photographs of samples in different states under UV light.

In the pristine state, the sample displayed many sharp and intense reflections, which indicated that the pristine sample was mainly composed of crystals, in agreement with the POM observation (**Figure 7.9**). After grinding, the size of the powder-like crystals is reduced and eventually the long-range crystalline ordering may be disrupted, as revealed by the XRD signals, which show no sharp, but a broad amorphous peak centered at 2θ=18° (the d-spacing is 0.49 nm, which corresponds to the average lateral distance between two neighboring molecules of **TPE-C_5-Chol**). The X-ray diffraction of the **TPE-C_5-Chol** powder sample in the glass state was nearly similar as that in grinding state. Therefore, it can be concluded that the thermo- and mechano-chromic properties are both caused by the change of the condensed state (crystallization or amorphization), which induce a change in molecular packing in the sample. When comparing the effect of dichloromethane (DCM) and hexane fuming treatment, DCM-

fuming leads to the formation of an amorphous solid, while fuming with hexane improves the crystalline organization in the pristine state, which results in sharper XRD signals.

In conclusion, the different molecular packing in the crystalline and amorphous phases is the cause of the stimuli-responsive chromatic properties above-discussed of these AIE molecules **TPE-C_n-Chol**.

7.4.2 Liquid crystal gelators with photo-responsive and AIE properties – Series TPE-Azobenzene-Cn-Chol (n = 0, 1, 3, 5)

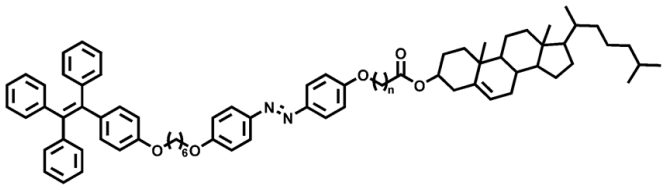

TPE-Azobenzene-C_n-Chol (n = 0, 1, 3, 5)

The main difference between **TPE-Azobenzene-C_n-Chol** and **TPE-C_n-Chol** is the introduction of an aliphatic spacer –O–$(CH_2)_6$–O– and an azobenzene moiety between **TPE** and **C_n-Chol**, as shown above.

7.4.2.1 DSC analysis and POM measurement

Similarly, DSC and POM were firstly used to identify the phases and phase transitions. **Figure 7.11** shows the DSC curves of **TPE-Azobenzene-C_n-Chol** series. With the addition of azobenzene (also a popular mesogen), the series of **TPE-Azobenzene-C_n-Chol** become liquid crystalline. More specifically, the molecules of **TPE-Azobenzene-C_n-Chol** with **n=0** and **n=3** exhibit, in pure state, enantiotropic LC feature, while those with **n=1** and **n=5** show monotropic LC phase. Moreover, molecules with **n=0**, **n=1** and **n=3** keep their LC phases at room temperature upon cooling after at least one heating history to isotropic (Iso) phase, while the molecule with **n=5** recrystallizes when T lower than 140 ℃. Another interesting observation is that the molecules **n=0, 1 and 3** present hot-crystallization upon further heating, probably because of the improvement of the molecular mobility upon heating that promote the recrystallization.

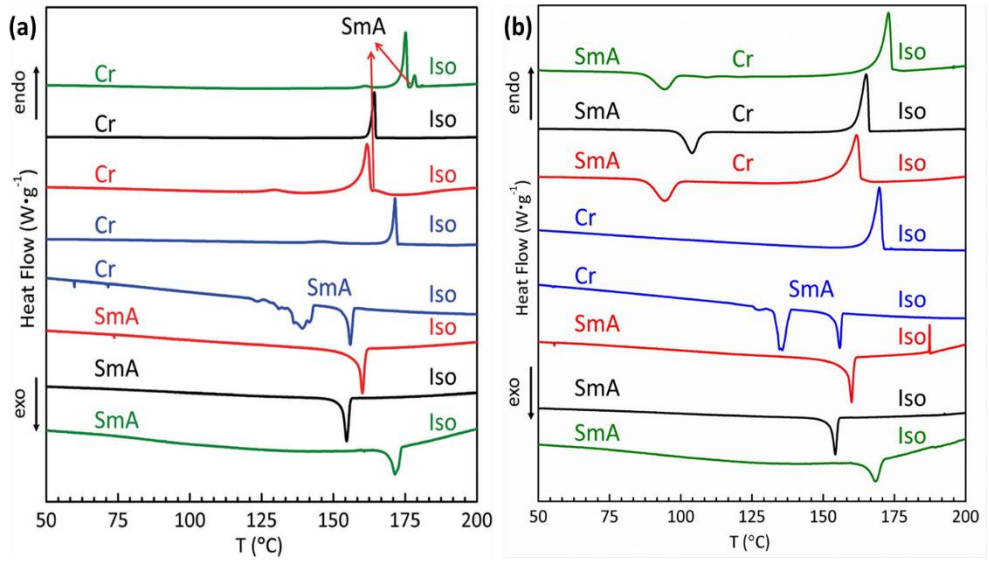

Figure 7.11 DSC curves of **TPE-Azobenzene-C_n-Chol** series upon (a) first and (b) second heating (4 upper)-cooling (4 lower) cycle at 2 ℃/min: **n=0** (green), **n=1** (black), **n=3** (red) and **n=5** (blue).

The POM characterization of these **TPE-Azobenzene-C_n-Chol** molecules, is presented in **Figure 7.12**. Typical smooth fan-shaped (focal conic) textures were observed for all four molecules upon cooling from isotropic phase, indicating the nature of a smectic A phase. For the molecules with **n=0** and **n=3**, enantiotropic smectic phase was observed, but only in a very narrow temperature range on slowly heating as shown in Figure 7.11 (a) green curve and **Figure 7.13** for **n=0**.

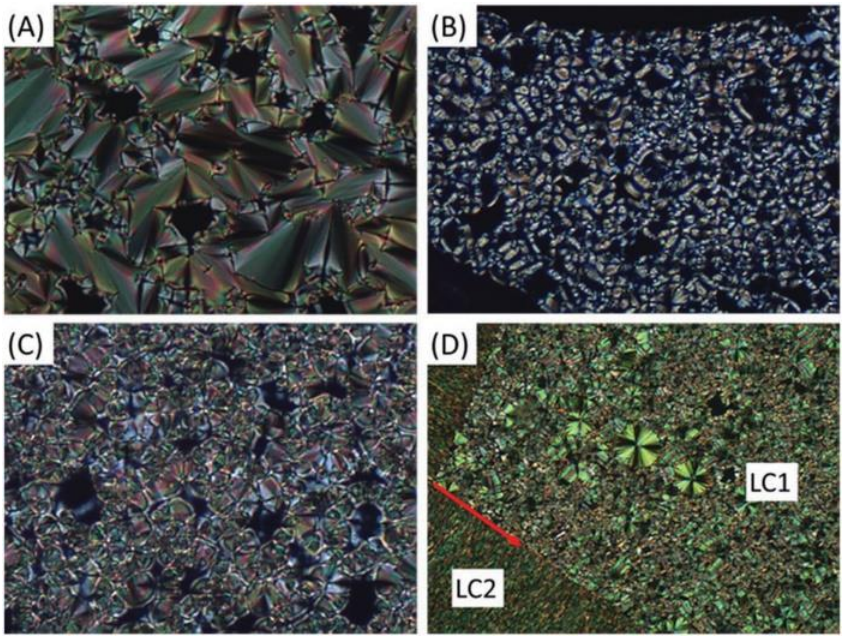

Figure 7.12 Textures of **TPE-Azobenzene-C_n-Chol** series observed by POM upon cooling from isotropic phase. (A) **n=0**, (B) **n=1** and (C) **n=3** at 25 ℃; (D) **n=5** at 145 ℃ (the phase LC2 started to grow from left)

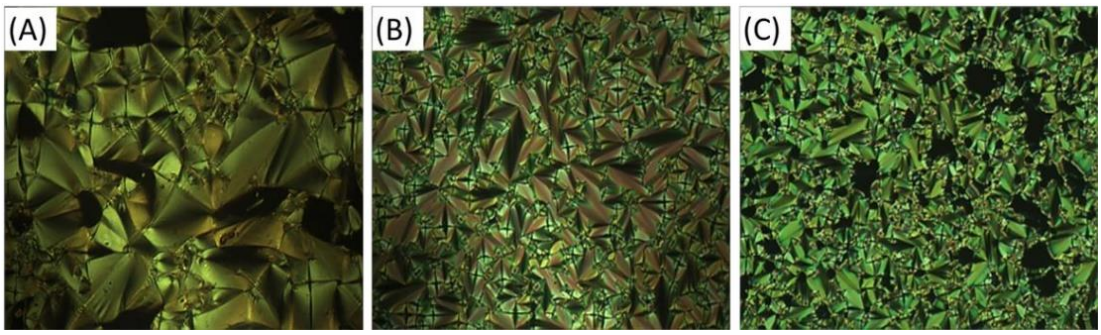

Figure 7.13 Textures of **TPE-Azobenzene-C$_0$-Chol** observed by POM. (A) 179 ℃ upon first heating, (B) 173 ℃ upon first cooling, (C) 175 ℃ upon second heating.

7.4.2.2 Wide- and small-angle X-ray scattering characterizations

WAXS and SAXS were applied to characterize the LC behavior of **TPE-Azobenzene-C$_n$-Chol** in a quantitative way. When measured by WAXS at RT, all compounds of **TPE-Azobenzene-C$_n$-Chol** series display an isotropic and broad diffraction reflection at higher 2theta area (**Figure 7.14**). According to the Bragg law, this diffuse ring has a *d*-spacing of about 0.47 nm, which refers to the average lateral distance between neighboring molecules.

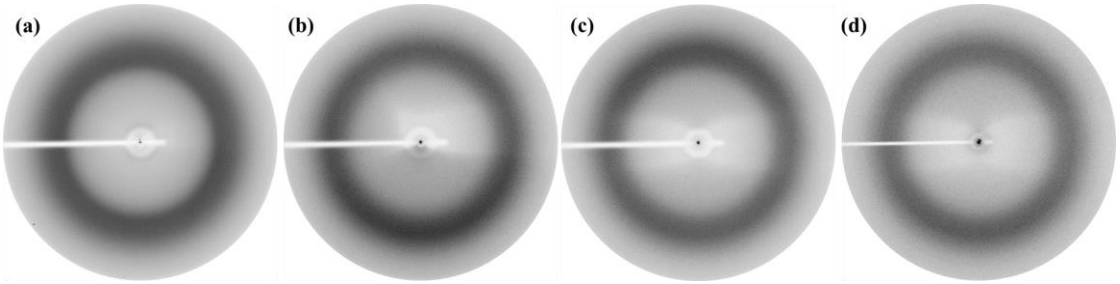

Figure 7.14 TPE-Azobenzene-C$_n$-Chol series observed by WAXS at RT. (a) **n=0**; (b) **n=1**; (c) **n=3**; (d) **n=5**.

The powder samples of **TPE-Azobenzene-C$_n$-Chol** with **n=0**, **n=1** and **n=3** were then heated to their isotropic state, and slowly cooled to RT. These thermally treated samples were measured by SAXS at RT. **Figure 7.15** shows its diffraction patterns and intensity profiles, which reveals that molecules with **n=0**, **n=1** and **n=3** have similar LC phase behavior with two orders of diffraction reflection ($q = 2\pi/d$, q_1 / q_2 = 1 : 2). These LC phases are smectic phase with layer spacings, d = 5.63, 5.85, and 6.01 nm, respectively.

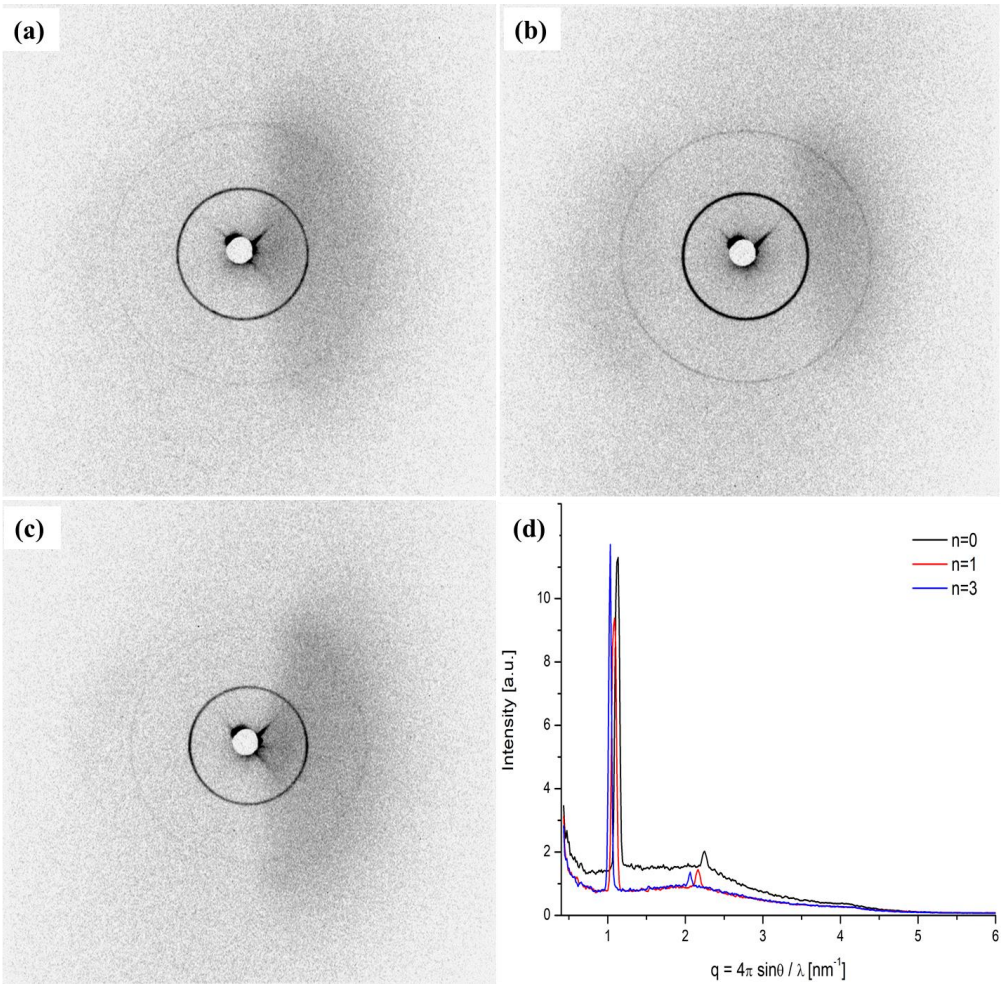

Figure 7.15 TPE-Azobenzene-C_n-Chol series measured at RT: SAXS patterns of (a) **n=0**; (b) **n=1**; (c) **n=3**; and (d) their corresponding intensity profile.

As for the **TPE-Azobenzene-C_5-Chol**, because it exhibits the LC phase at high temperatures around 145 ℃ (Figures 7.11 and 7.13), thermal-SAXS measurements at different temperatures were performed. Because of its monotropic LC feature, the cooling scan was focused, and the result is showed in **Figure 7.16**. Notably, the smectic order fluctuation still exists even in isotropic phase (180 ℃) where a large peak corresponded to the 4th order diffraction reflection of the smectic A (with coherent length of ζ = 9.8 nm). At 145 °C, SAXS pattern showed two orders of diffraction reflections ($q = 2\pi/d$, q_1 / q_4 = 1 : 4) with a smectic spacing of 6.35 nm (ζ =50 nm from q_1 peak). Four orders of diffraction reflections ($q = 2\pi/d$, 1: 2: 3: 4) was observed with a smectic spacing of d = 6.17 nm for LC2 phase at 100 ℃. The spacing continued to decrease to 6.08 nm at room temperature (RT) without any phase transition. From the available data, the nature of LC2 cannot be defined precisely. It should be a smectic phase with higher orders.

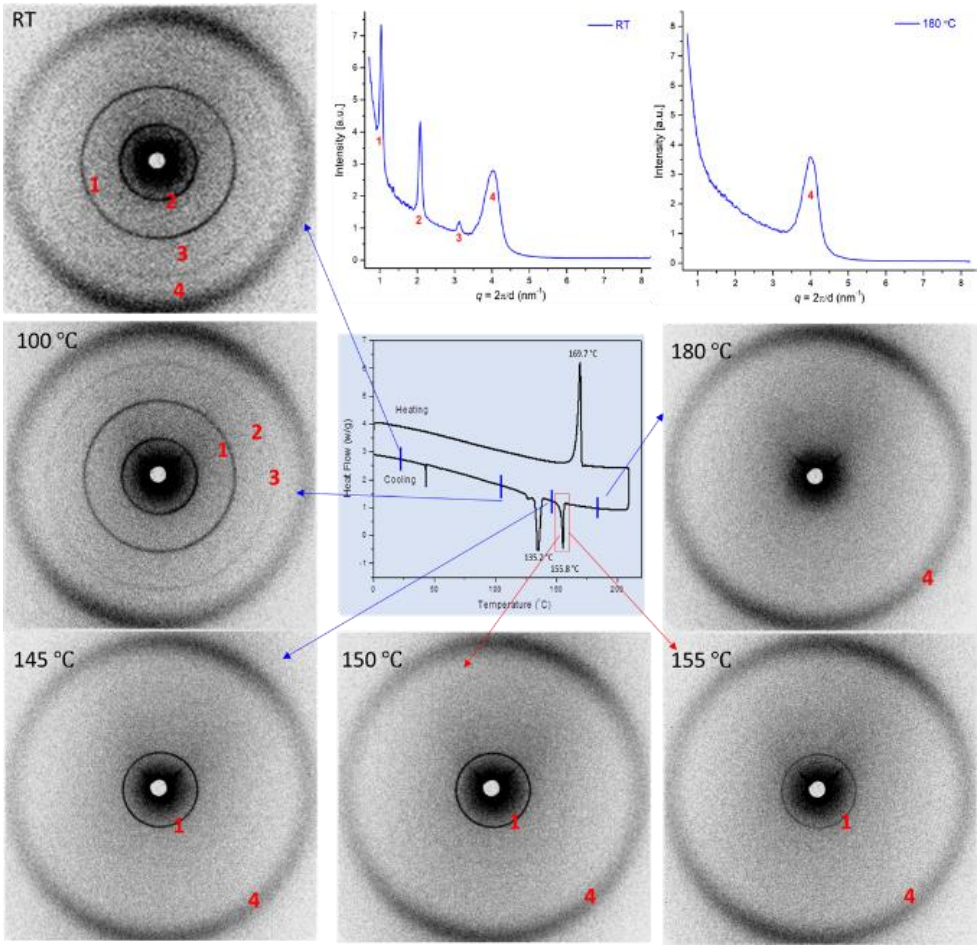

Figure 7.16 The thermal-SAXS of **TPE-Azobenzene-C$_5$-Chol** molecules measured at different temperature.

Finally, WAXS and SAXS were performed on the aligned sample of **TPE-Azobenzene-C$_5$-Chol**, which was prepared as follows. The sample was first heated to isotropic phase (180 ℃) and then cooled to 150 ℃, at which the melt sample was introduced into a flat capillary. Thus, the molecules were aligned by capillarity. The flat capillary sample was then quenched to room temperature on a metallic surface, and then studied by WAXS and SAXS. The results together with those of previous un-aligned sample, are displayed in **Figure 7.17**. Similar to the thermal-SAXS result (**Figure 7.16**), **Figure 7.17b** shows 4 orders of Bragg reflections corresponding to a layer spacing of 6.09 nm. However, in the WAXS pattern of aligned sample, three characteristic features were found: (i) same smectic diffraction orders as observed in small angles (in the dashed red rectangle); (ii) crystalline diffraction orders in the yellow symmetrical arc area, which is normal to the LC director; (iii) a broad diffuse reflection at wider angle. Therefore, LC2 phase at RT presents higher orders (than smectic A phase at higher temperature) with some crystalline features.

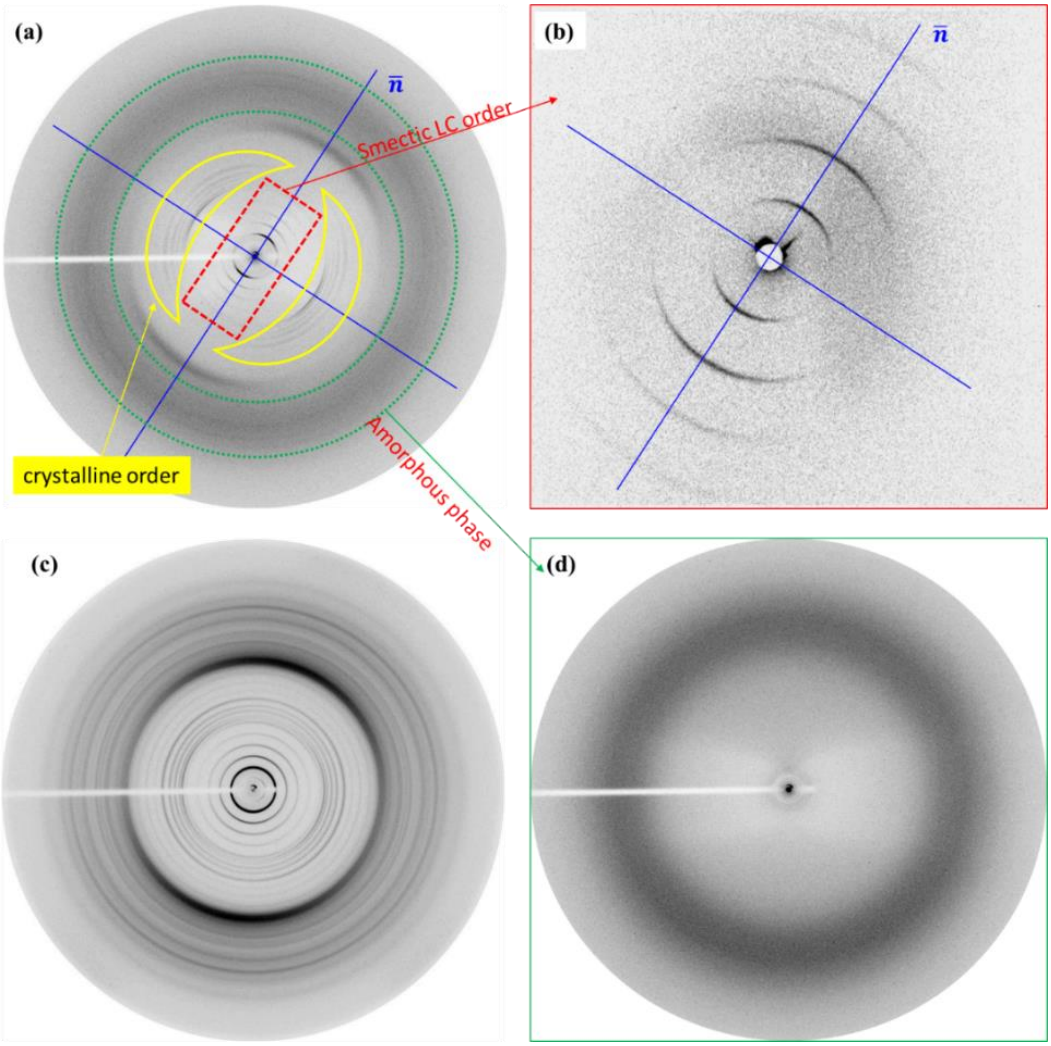

Figure 7.17 WAXS (a) and SAXS (b) measured at RT of the aligned **TPE-Azobenzene-C$_5$-Chol** sample, compared with WAXS of unaligned sample in crystalline state (c) and pristine state after synthesis (d). $\bar{n}$ refers to the direction of molecules.

Finally, the period *d* of SmA phase of each **TPE-Azobenzene-C$_n$-Chol** derivatives (*d* = 5.63, 5.85, 6.01 and 6.35 nm) corresponds to a value between *l* and 2*l*, *l* being the stretched length of each molecule (*l* = 4.74, 4.95, 5.26 and 5.52 nm) as calculated by its molecular model with ChemDraw. Hence, all molecules of **TPE-Azobenzene-C$_n$-Chol** exhibit an interdigitated antiparallel bilayer smectic A phase (**SmA$_d$ phase**) as shown in **Figure 7.18**. This is also comprehensible from the major difference of molecular areas between the TPE subunit (clover-like) and azobenzene/cholesterol parts (rod-like), which prevents the single layer organization. The non-flexible and non-rod-like tetraphenylethylene (TPE) fitted finally into the wholly rod-like molecules and didn't destroy their LC properties.

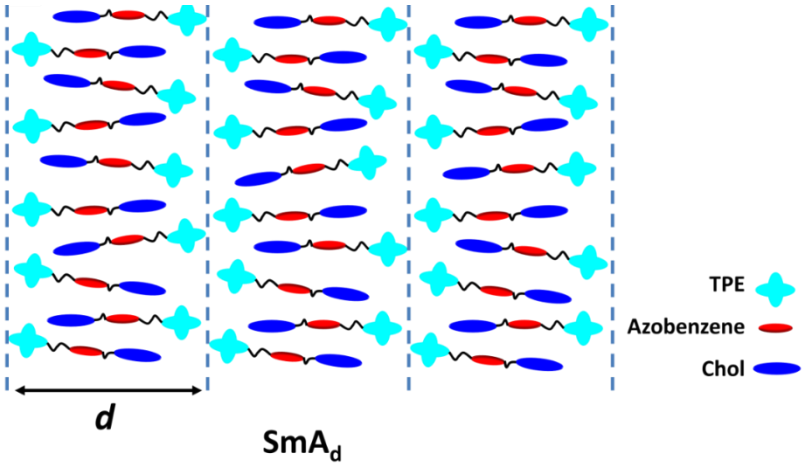

Figure 7.18 A possible model of molecular organization of SmA_d.

7.5 Conclusion

(1) In the series of **TPE-C_n-Chol**, the clover-shaped TPE unit introduced into the rod-like cholesterol mesogen inhibits not only the formation of a liquid-crystal phase but also the recrystallization upon cooling from the isotropic liquid phase. Very interestingly, TPE-C_n-Chol molecules in the condensed state change their fluorescence color under external stimuli, such as melting, grinding, and solvent fuming. The phase transition, *i.e.*, crystallization or amorphization, that can induce a change in molecular packing in the condensed state, is the origin of these thermo-, mechano-, and vapo-chromic properties.

(2) In the series of **TPE-Azobenzene-C_n-Chol**, the smectic-A LC behavior can be facilitated and achieved by integrating cholesterol and azobenzene moieties with TPE, and the spacer length of alkyl chain can influence the thermodynamical stability of mesophases during heating and cooling process. From the careful analyses of WAXS and SAXS data, a model of interdigitated antiparallel bilayer smectic A phase, SmA_d, is proposed for **TPE-Azobenzene-C_n-Chol** LC phase.

References

[1] Žinic, M., Vögtle, F., & Fages, F. (2005). Cholesterol-based gelators. In *Low Molecular Mass Gelator* (pp. 39-76). Springer, Berlin, Heidelberg

[2] Kato, T., Mizoshita, N., Moriyama, M., & Kitamura, T. (2005). Gelation of liquid crystals with self-assembled fibers. In *Low Molecular Mass Gelator* (pp. 219-236). Springer, Berlin, Heidelberg.

[3] Koumura, N., Kudo, M., & Tamaoki, N. (2004). Photocontrolled gel-to-sol-to-gel phase transitioning of meta-substituted azobenzene bisurethanes through the breaking and reforming of hydrogen bonds. *Langmuir*, 20(23), 9897-9900.

[4] Wang, C., Chen, Q., Sun, F., Zhang, D., Zhang, G., Huang, Y., ... & Zhu, D. (2010). Multistimuli responsive organogels based on a new gelator featuring tetrathiafulvalene and azobenzene groups: reversible tuning of the gel−sol transition by redox reactions and light irradiation. *Journal of the American Chemical Society*, 132(9), 3092-3096.

[5] Wang, S., Shen, W., Feng, Y., & Tian, H. (2006). A multiple switching bisthienylethene and its photochromic fluorescent organogelator. *Chemical communications*, (14), 1497-1499.

[6] van Herpt, J. T., Areephong, J., Stuart, M. C., Browne, W. R., & Feringa, B. L. (2014). Light-Controlled Formation of Vesicles and Supramolecular Organogels by a Cholesterol-Bearing Amphiphilic Molecular Switch. *Chemistry–A European Journal*, 20(6), 1737-1742.

[7] Zhao, Z., Lam, J. W., & Tang, B. Z. (2013). Self-assembly of organic luminophores with gelation-enhanced emission characteristics. *Soft Matter*, 9(18), 4564-4579.

[8] Luo, M., Wang, S., Wang, M., Huang, S., Li, C., Chen, L., & Ma, X. (2016). Novel organogel harnessing Excited-State Intramolecular Proton Transfer process with aggregation induced emission and photochromism. *Dyes and Pigments*, 132, 48-57.

[9] Seddon, J. M. (1998). Structural studies of liquid crystals by X-ray diffraction. *Handbook of liquid crystals*, *1*, 635-679.

[10] a) Chen, H., Zhou, L., Shi, X., Hu, J., Guo, J., Albouy, P. A., & Li, M. H. (2019). AIE Fluorescent Gelators with Thermo-, Mechano-, and Vapo-chromic Properties. *Chemistry–An Asian Journal*, 14(6), 781-788; b) Yu, X., Chen, H., Shi, X., Albouy, P. A., Guo, J., Hu, J., & Li, M. H. (2018). Liquid crystal gelators with photo-responsive and AIE properties. *Materials Chemistry Frontiers*, 2(12), 2245-2253.

Part III

General Conclusion

Chapter 8

Summary and Future Works

Contents

8.1 Conclusions

This thesis started with the apparently simple question of the crystalline structure of PDMS and actually ends with many more questions! It helped push forward many intriguing features that somehow remained unaddressed probably due to the difficulty of working at low temperature.

An important point that was demonstrated in **Chapter 3** relates to the strain amplification factor: it represents the ratio between the actual strain experienced by the soft PDMS phase to the macroscopic applied strain. If φ represents the volume fraction of hard phase (silica particles) the expected factor is $1/(1-\varphi)$ simply based on geometrical considerations. We could show that the experimental value was much higher in case of in-situ silica loading by a sol-gel process: for instance, a factor 2.31 is measured at 35phr while 1.15 is expected. For comparison we obtained 1.19 for a sample filled with powder silica in a similar proportion. To the best of our knowledge this factor has never been experimentally evaluated for this type of systems and more systematic studies would be of interest.

The fact that polymorphism is not necessary to account for the diffraction patterns changes with applied draw ratio is clearly demonstrated in **Chapter 4**. All patterns can be quantitatively accounted for with a similar tetragonal unit cell and all the observed modifications simply reflect texture changes. The tetragonal axis [001] is preferentially aligned along the draw axis at low stretch; the preferential axis progressively kips to the [111] diagonal direction at high stretch while remaining in the $(\bar{1}10)$ plane.

Experiments presented in **Chapter 4** require low temperatures that are reached by a cooling-warming sequence. The behavior of the tensile force in relation to the crystallization process during this thermal sequence is addressed in **Chapter 5**. It is shown that the sudden and tremendous stress rise that is observed during cooling appears only after most of the crystallization process is completed. It is assumed that the modulus of the semi-crystalline elastomer is magnified by the presence of confined amorphous phase. In these conditions the stress increase is simply related to thermal contraction of the sample. Moduli evaluated with this assumption are typically in the order of magnitude of DMA results published by another group. In agreement with Tosaka's results we could also show that the so-called "mesomorphous phase" that develops at high stretch and room temperature is related by some epitaxy relation to the

crystalline phase observed after cooling. A far-fetching implication is that polymer chains in the mesomorphous phase and in the high stretch crystalline texture are oriented similar.

An atomic resolution of the PDMS crystalline structure is attempted in **Chapter 6**. High-resolution diffractograms unambiguously confirm the tetragonal assignment with lattice parameters of $a = b = 8.428\,\text{Å}$ and $c = 12.053\,\text{Å}$ at 170K and a calculated density 1.150 g/cm^3 assuming 8 monomers per unit cell; this last value is close to experimental evaluations. Various softwares have been used for the data treatment. Among the proposed space groups, $I\,4_1$ is the only one compatible with the experimental crystal density and a position occupancy of 1 (8 monomers per unit cell). However, diffraction line intensities are not accounted for in a very satisfying way and in particular the 110 reflection is predicted strong while experimentally nearly extinct. Space group $I\,4_1/a$ was tried with an occupancy of 0.5 to remain compatible with the crystal density. The absence of the 110 reflection is accounted for but the computed line intensities remain far from the experimental data.

In addition, two cholesterol-based organogelators were also studied by different X-ray scattering techniques. The results suggest a change in molecular packing is the origin of stimuli-responsive chromatic property in TPE-C_n-Chol molecules; a smectic-A phase with interdigitated antiparallel bilayer was testified in TPE-Azobenzene-Cn-Chol molecules.

8.2 Perspectives

All the above-discussed results and the absence of clear answers open quite interesting perspectives:

(1) The question of the strain amplification factor could be first addressed. Preliminary small-angle X-ray scattering (SAXS) experiments on our samples confirm a nice level of organization of the filler: a diffraction ring associated to well-defined inter-filler particles is observed which has been reported by other authors. It has been also reported by other groups that the final mechanical properties depend upon the way (basic or acidic) silica is condensed into the PDMS matrix. This has been related to the filler morphology that has been shown to be different in both cases by SAXS. Our WAXS experiments that allow a precise evaluation of the strain

amplification factor would be of great interest to correlate mechanical and morphology changes.

(2) A more anecdotal point relates to the apparently reproducible observation of stress plateaus or kinks during the stress rise associated to cooling and warming sequences. Holding the samples in a more secure way could give a definite answer about their reality.

(3) The most important remaining question is the atomic resolution of the PDMS crystalline structure. Closely related to this is the evolution of the crystalline texture with applied extension. If the polymer chain is aligned along the tetragonal axis, this means that the chain direction is at 45 ° from the draw axis at higher stretches. There is apparently a relation between the "mesomorphous phase" at room temperature and the crystalline texture that seemingly implies that the chain orientation is similar in both cases. That the chain direction at room temperature and high draw ratios is not parallel to the stretching direction, at least in a fraction of the sample, is quite strange. Other methods like NMR or perhaps infra-red could definitively settle the question of the chain orientation within the crystal unit cell and at room temperature. If the chain orientation along the tetragonal axis is confirmed, a deeper analysis of possible disorders should be done: we already stressed the fact that having only 4_1 or 4_3 helices as is the case for the $I\,4_1$ space group is puzzling. The other $I\,4_1/a$ does not present this problem but it is probable that the disorder is not well introduced by a mere half site occupancy.

université PARIS-SACLAY | ÉCOLE DOCTORALE Physique en l'Île-de-France (PIF)

Titre : La structure cristalline du polydiméthylsiloxane: résultats supplémentaires et questions supplémentaires

Mots clés : poly(diméthylsiloxane) (PDMS), caoutchouc silicone, amplification des déformations, diagrammes de fibre, propriétés thermo-élastiques, cristallographie

Résumé : L'objectif principal de ce travail est de tenter d'élucider la structure cristalline du poly(diméthylsiloxane) (PDMS). Nous avons d'abord synthétisé des élastomères PDMS chargés en silice soit par mélange physique ou soit par croissance in situ, afin d'obtenir des échantillons pouvant supporter les élongations nécessaires à notre étude. En couplant tests mécaniques et diffraction des rayons X (WAXD) à température ambiante, il a été montré que les échantillons chargés in situ présentaient un facteur d'amplification des déformations anormalement élevé. Des clichés de diffraction obtenus à basse température et sous différentes extensions sur des échantillons cristallisés ont été comparés à des simulations : il a été démontré que les changements observés provenaient d'une évolution de la texture cristalline, la maille restante quadratique. Ceci contredit l'hypothèse d'un polymorphisme. L'augmentation soudaine de la contrainte lors du refroidissement d'un élastomère PDMS pré-étiré est connue. Il est montré que ceci n'apparaît qu'une fois la cristallisation terminée : cet effet serait dû à la contraction thermique et à l'augmentation du module de Young résultant de la présence de cristallites et d'une phase amorphe confinée. Une détermination atomique de la structure cristalline de PDMS a été tentée, basée sur des mesures de diffraction X de poudre à basse température. Les techniques de recuit simulé simulation, l'optimisation de DFT et d'affinement de Rietveld ont été utilisées. Deux groupes d'espace $I\,4_1$ et $I\,4_1/a$ sont proposés et les positions atomiques calculées pour chaque cas. Toutefois, aucune de ces propositions n'est vraiment satisfaisante en ce qui concerne les intensités calculées. D'autres hypothèses sont formulées.

En complément de ce travail, deux organogélateurs à base de cholestérol ont été étudiés par différentes techniques de diffusion des rayons X. Les résultats suggèrent qu'un changement de l'empilement moléculaire est à l'origine des propriétés chromatiques stimulo-sensibles des molécules de TPE-C n-Chol. L'existence d'une phase smectique-A avec bicouche antiparallèle inter-digitée a été également démontrée pour les molécules de TPE-Azobenzene-Cn-Chol.

Université Paris-Saclay
Espace Technologique / Immeuble Discovery
Route de l'Orme aux Merisiers RD 128 / 91190 Saint-Aubin, France

université PARIS-SACLAY | ÉCOLE DOCTORALE Physique en l'Île-de-France (PIF)

Title: The crystalline structure of polydimethylsiloxane: additional results and additional questions

Keywords: poly (dimethylsiloxane) (PDMS), silicone rubber, strain amplification, fiber diagrams, thermo-elastic properties, crystallography

Abstract: The main objective of this work is to elucidate the crystalline structure of poly(dimethylsiloxane) (PDMS). Silica-filled PDMS elastomers are first synthesized by either physical mixing or in-situ sol-gel loading to obtain specimens that can sustain the extensions necessary for our purpose. Coupling tensile tests and X-ray diffraction (WAXD) at room temperature, it was found that the sol-gel silica filled samples exhibited an anomalously high strain amplification factor. Thereafter, WAXD patterns of PDMS elastomer under different extensions were collected at low temperature (typically -100 ℃) and the comparison between experimental data and simulations unambiguously demonstrated that the impressive pattern changes observed with increasing deformation originated from textures, the crystal unit cell remaining tetragonal unit cell in all cases; this contradicts the hypothesis of a possible polymorphism. A sudden rise in stress has been previously reported during cooling of a pre-stretched silicone rubber. It is presently shown to appear after crystallization is completed and it is to the combined effect of thermal contraction and the increase of Young's modulus that results from the presence of crystallites and harder confined amorphous phase. Based on low-temperature powder X-ray diffraction and selected area electron diffraction, an atomic determination of the crystal structure of was attempted by annealing simulation, DFT optimization as well as Rietveld refinement. Two space groups of $I\,4_1$ (No. 80) and $I\,4_1/a$:1 (No. 88-1) with a 0.5 occupancy probability are proposed and the atomic positions are computed for each case. However, no one of this proposal is really satisfying as regard to the computed intensities. Further hypothesis is formulated.

As a complement to this work, two cholesterol-based organogelators were studied by different X-ray scattering techniques. The results suggest a change in molecular packing is at the origin of stimuli-responsive chromatic properties in TPE-C n -Chol molecules. A smectic-A phase with inter-digitated antiparallel bilayer was also evidenced in TPE-Azobenzene-Cn-Chol molecules.

Université Paris-Saclay
Espace Technologique / Immeuble Discovery
Route de l'Orme aux Merisiers RD 128 / 91190 Saint-Aubin, France